



INSTITUTO SUPERIOR TÉCNICO
Universidade Técnica de Lisboa

Spatiotemporal dynamics of CBF and BOLD fMRI responses to breath-hold challenges

Joana Carolina Sequeira Pinto

Dissertação para obtenção do Grau de Mestre em
Engenharia Biomédica

Júri

Presidente:	Prof. Doutor Pedro Miguel Félix Brogueira
Orientador:	Prof. Patrícia Margarida Piedade Figueiredo
Co-Orientador:	Doutor Pedro Vilela
Vogal:	Prof. João Miguel Raposo Sanches

Novembro de 2012

Abstract

The study of cerebrovascular reactivity is important for the evaluation of neurological diseases. Functional magnetic resonance imaging (MRI) techniques are currently being explored for this purpose, namely the Blood Oxygenated Level-Dependent (BOLD) contrast and the Arterial Spin Labelling (ASL) cerebral blood flow (CBF) contrast. In this work, we aimed to characterize the spatiotemporal dynamics of both ASL and BOLD responses to breath-holding (BH) challenges.

A group of 7 healthy subjects were studied on a 3T MRI system using two BH protocols (with and without preparatory inspiration). Optimal BOLD and ASL data were acquired and BOLD, BOLD_{ASL} and CBF contrasts were obtained. Data were analysed based on a general linear model using two approaches (Sine Delay Optimization (SDO)/Sine Cosine Linear Combination (SCC)). The amplitude of cerebrovascular reactivity (CVR) and the associated cerebrovascular delays (CVD) were estimated for each contrast/BH protocol.

Both SDO and SCC models were successful in obtaining CVR and CVD values/maps. However, SCC yielded CVR and CVD voxelwise and showed greater sensitivity for BOLD and BOLD_{ASL} responses. The CBF data showed larger CVD variations relative to BOLD_{ASL} data. The BH protocol with preparatory inspiration led to larger values of CVD and the corresponding time courses showed a more complex shape relative to the BH protocol without inspiration.

In conclusion, we implemented a modelling approach that allows estimation of CVR and CVD voxelwise. Although BOLD data have been analysed in similar ways, to our knowledge, this is the first study of the spatiotemporal dynamics of ASL BOLD and CBF data.

Keywords

Functional Magnetic Resonance, Arterial Spin Labelling, Blood Oxygenation Level Dependent, Breath-Hold Challenge, Cerebrovascular Reactivity, Cerebrovascular Delay.

Resumo

O estudo da vasoreactividade cerebral é importante na avaliação de doenças neurológicas. Técnicas de ressonância magnética (MRI) funcional estão a ser exploradas para este propósito, nomeadamente o contraste Blood Oxygenated Level Dependent (BOLD) e o contraste fluxo sanguíneo cerebral (CBF) do Arterial Spin Labelling (ASL). O objectivo deste trabalho consiste em caracterizar a dinâmica espacial/temporal das respostas BOLD e ASL a tarefas de apneia (BH).

7 sujeitos saudáveis foram estudados num sistema MRI 3T usando dois protocolos de BH (com/sem inspiração preparatória). Foram adquiridas imagens BOLD optimizado e ASL e os contrastes BOLD, BOLD_{ASL} e CBF foram obtidos. As imagens foram analisadas utilizando o modelo geral linear (GLM) e usando duas abordagens (Sine Delay Optimization (SDO)/Sine Cosine Linear Combination (SCC)). A amplitude da vasoreactividade (CVR) e os atrasos da vasoreactividade (CVD) foram estimados para cada contraste/protocolo BH.

O SDO e SCC foram bem-sucedidos na obtenção dos valores/mapas de CVR e CVD. No entanto, a abordagem SCC obteve CVR e CVD voxel-a-voxel e mostrou maior sensibilidade para respostas BOLD e BOLD_{ASL}. A informação CBF apresenta uma maior variação de CVDs relativamente à informação BOLD_{ASL}. O protocolo BH com inspiração preparatória conduziu a valores de CVD mais elevados e a evolução temporal apresenta uma forma mais complexa relativamente ao protocolo sem inspiração preparatória.

Em conclusão, implementámos um método que permite estimar CVR e CVD voxel-a-voxel. Apesar da informação BOLD já ter sido analisada de forma semelhante, este é o primeiro estudo da dinâmica espacial/temporal dos contrastes BOLD e CBF do ASL.

Palavras Chave

Ressonância Magnética Funcional, Arterial Spin Labelling, Blood Oxygenation Level Dependent, Tarefa de Apneia, Vasoreactividade, Atraso da Vasoreactividade.

Agradecimentos

Em primeiro lugar gostaria de agradecer à minha orientadora, Professora Patrícia Figueiredo, pela oportunidade de desenvolver a minha tese numa área tão cativante e por todos conhecimentos que partilhou ao longo deste período. Não posso deixar de agradecer profundamente todo o apoio, entusiasmo, paciência e constante disponibilidade.

Agradeço também ao meu co-orientador, Dr. Pedro Vilela, pela oportunidade de adquirir as imagens que são a base de todo este trabalho e pela disponibilidade em responder a todas as minhas dúvidas sobre as bases fisiológicas desta tese.

Aos meus colegas de sala (6.14) que me apoiaram e animaram nesta etapa final.

Um agradecimento especial à Inês Sousa pelos conhecimentos partilhados e pela disponibilidade e ao João Jorge pela aquisição dos dados e pelos algoritmos que gentilmente me forneceu, nomeadamente o de visualização das imagens (*BrainVis*).

A todos os meus amigos e colegas que me apoiaram ao longo destes 5 anos.

À minha família por estarem sempre presentes e me encorajarem nos momentos de mais dificuldade. Um especial agradecimento aos meus pais, por me terem proporcionado a oportunidade de vir estudar para Lisboa e realizar este curso, e por todo o apoio incondicional que me deram, não só durante esta etapa, mas durante toda a minha vida.

Contents

Abstract.....	v
Resumo.....	vii
Agradecimentos.....	ix
Contents.....	xi
List of Figures	xiii
List of Tables	xix
List of Acronyms and Abbreviations	xxi
1 Introduction	1
1.1. Physiological Principles	2
1.1.1. Cerebrovascular Reactivity and Cerebrovascular Delay.....	2
1.1.2. Vasoactive Challenges	3
1.1.3. Measurement Techniques	5
1.2. Functional Magnetic Resonance Imaging Principles.....	6
1.2.1. MRI Basic Principles.....	6
1.2.2. Blood Oxygenation Level Dependent Contrast	8
1.2.3. Arterial Spin Labelling.....	9
1.2.4. General Linear Modelling	11
1.3. State of the Art.....	13
1.3.1. BOLD and ASL Sequences	13
1.3.2. CVR assessment using BOLD and ASL BH responses.....	14
1.4. Goals and approach	15
1.4.1. Thesis Outline.....	16
1.5. Contributions arising from this work	16
2 Methods	17
2.1. Data Acquisition.....	18
2.1.1. Subjects and Tasks	18
2.1.2. Acquisition Sequences	20
2.2. Data Analysis.....	20
2.2.1. Pre-Processing	20
2.2.2. General Linear Modelling	23
2.2.2.1. Breath Hold Response Model	24
2.2.2.2. Sine Delay Optimization	25
2.2.2.2.1. BOLD Signal Regressors.....	25
2.2.2.2.2. ASL Signal Regressors.....	26

2.2.2.2.3.	Calculation of CVR and CVD	27
2.2.2.2.4.	Using Motion Parameters and Harmonics	27
2.2.2.3.	Sine Cosine Linear Combination	28
2.2.2.3.1.	BOLD Signal Regressors	29
2.2.2.3.2.	ASL Signal Regressors	30
2.2.2.3.3.	Calculation of CVR and CVD	31
2.2.3.	Time Courses	32
3	Results	33
3.1.	Partial Pressure of End Tidal Carbon Dioxide	34
3.2.	Head Motion – Subject Exclusion	35
3.3.	Analysis Method Comparison	36
3.3.1.	Spatial Measurements	36
3.3.1.1.	Number of Responsive Voxels	36
3.3.1.2.	Cerebrovascular Delay Values	38
3.3.1.3.	Cerebrovascular Reactivity Values	44
3.3.2.	Cerebrovascular Reactivity and Delay Maps	46
3.3.2.1.	Individual Maps	46
3.4.	Breath-Hold Protocol Comparison	55
3.4.1.	Spatial Measurements	55
3.4.1.1.	Number of Responsive Voxels	55
3.4.1.2.	Cerebrovascular Delay Values	56
3.4.1.3.	Cerebrovascular Reactivity Values	58
3.4.2.	Cerebrovascular Reactivity and Delay Maps	60
3.4.2.1.	Group Maps	60
3.4.3.	Time Courses	71
4	Discussion and Conclusions	75
	Bibliography	78

List of Figures

Figure 1.1: Cerebrovascular autoregulation and the effect of blood gases on CBF. Retrieved from [17].	4
Figure 2.1: Breath-Hold without preparatory inspiration protocol presented to the subjects.	18
Figure 2.2: Breath-Hold with preparatory inspiration protocol presented to the subjects.	18
Figure 2.3: Summary of the different types of BH challenges and image acquisition sequences and resulting signal contrasts.	19
Figure 2.4: The breath-hold without preparatory inspiration time course for the BOLD and ASL protocols.	19
Figure 2.5: The breath-hold with preparatory inspiration time course for the BOLD and ASL data.	20
Figure 2.6: Example of a subject's structural images (left to right: coronal, sagittal and axial) before (top) and after (bottom) brain extraction using BET.	21
Figure 2.7: Motion correction results for one example subject. The relative displacement corresponds to the head position at each time point relative to the previous time point. The absolute displacement is calculated relative to the volume in the middle of the time series. The x axis represents the number of imaging volumes (TR=2.5s).	21
Figure 2.8: Summary of the steps performed during statistical analysis. Comparison between the two GLM approaches.	23
Figure 2.9: Relation between cerebrovascular delay (CVD), cerebrovascular reactivity (CVR) and breath-hold (BH) period.	24
Figure 2.10: Design matrix for the BOLD data set analysis (time runs vertically) and corresponding contrasts.	25
Figure 2.11: Design matrix for the ASL data set analysis (time runs vertically) and corresponding contrasts.	26
Figure 2.12: Mean number of responsive voxels of subjects obtained with a normal analysis and with analysis using harmonics and motion parameters as regressors. Error bars represent standard deviations of the mean.	28
Figure 2.13: Design matrix for the BOLD data set analysis (time runs vertically) and corresponding contrasts.	29
Figure 2.14: Design matrix for the ASL data set analysis (time runs vertically) and corresponding contrasts.	30
Figure 3.1: Bar charts of the P_{ET-CO_2} values during BH challenge with and without preparatory inspiration. * represents significant differences ($p < 0.05$).	35
Figure 3.2: Bar charts of mean head displacement in mm during BH challenge without preparatory inspiration (left) and with preparatory inspiration (right).	36
Figure 3.3: Bar chart of number of responsive voxels for each subject using the two modelling approaches (SDO and SCC), for each of the contrasts considered (BOLD, BOLD _{ASL} and CBF).	37

Figure 3.4: Bar chart of number of responsive voxels of the mean of all subjects using the two modelling approaches (SDO and SCC), for each of the contrasts considered (BOLD, BOLD _{ASL} and CBF). * represents significant differences ($p < 0.005$).	38
Figure 3.5: Bar chart of global CVD values for each subject using the two modelling approaches (SDO and SCC) approaches, for each of the contrasts considered (BOLD, BOLD _{ASL} and CBF).	39
Figure 3.6: Bar chart of the mean CVD values of all subjects using the SDO approach and the SCC approach. * represents significant differences ($p < 0.005$).	39
Figure 3.7: Bar chart (SDO approach) and histogram (SCC approach) of the number of responsive voxels of the BOLD _{ASL} data of subject R1.	40
Figure 3.8: Bar chart (SDO approach) and histogram (SCC approach) of the number of responsive voxels of the BOLD _{ASL} data of subject R2.	40
Figure 3.9: Bar chart (SDO approach) and histogram (SCC approach) of the number of responsive voxels of the BOLD _{ASL} data of subject R3.	40
Figure 3.10: Bar chart (SDO approach) and histogram (SCC approach) of the number of responsive voxels of the BOLD _{ASL} data of subject R4.	41
Figure 3.11: Bar chart (SDO approach) and histogram (SCC approach) of the number of responsive voxels of the BOLD _{ASL} data of subject R5.	41
Figure 3.12: Bar chart (SDO approach) and histogram (SCC approach) of the number of responsive voxels of the BOLD _{ASL} data of subject R6.	41
Figure 3.13: Bar chart (SDO approach) and histogram (SCC approach) of the number of responsive voxels of the BOLD _{ASL} data of subject R7.	42
Figure 3.14: Bar chart (SDO approach) and histogram (SCC approach) of the number of responsive voxels of the CBF data of subject R1.	42
Figure 3.15: Bar chart (SDO approach) and histogram (SCC approach) of the number of responsive voxels of the CBF data of subject R2.	42
Figure 3.16: Bar chart (SDO approach) and histogram (SCC approach) of the number of responsive voxels of the CBF data of subject R3.	43
Figure 3.17: Bar chart (SDO approach) and histogram (SCC approach) of the number of responsive voxels of the CBF data of subject R4.	43
Figure 3.18: Bar chart (SDO approach) and histogram (SCC approach) of the number of responsive voxels of the CBF data of subject R5.	43
Figure 3.19: Bar chart (SDO approach) and histogram (SCC approach) of the number of responsive voxels of the CBF data of subject R6.	44
Figure 3.20: Bar chart (SDO approach) and histogram (SCC approach) of the number of responsive voxels of the CBF data of subject R7.	44
Figure 3.21: Bar chart of global CVR values for each subject using the two modelling approaches (SDO and SCC) approaches, for each of the contrasts considered (BOLD, BOLD _{ASL} and CBF).	45
Figure 3.22: Bar chart of the mean CVR values of all subjects using the SDO approach and the SCC approach. * represents significant differences ($p < 0.005$).	46

Figure 3.23: CVR and CVD maps obtained for subject R1, using the two modelling approaches and for the two ASL contrasts.	48
Figure 3.24: CVR and CVD maps obtained for subject R2, using the two modelling approaches and for the two ASL contrasts.	49
Figure 3.25: CVR and CVD maps obtained for subject R3, using the two modelling approaches and for the two ASL contrasts.	50
Figure 3.26: CVR and CVD maps obtained for subject R4, using the two modelling approaches and for the two ASL contrasts.	51
Figure 3.27: CVR and CVD maps obtained for subject R5, using the two modelling approaches and for the two ASL contrasts.	52
Figure 3.28: CVR and CVD maps obtained for subject R6, using the two modelling approaches and for the two ASL contrasts.	53
Figure 3.29: CVR and CVD maps obtained for subject R7, using the two modelling approaches and for the two ASL contrasts.	54
Figure 3.30: Bar chart of number of responsive voxels for each subject using the BH protocol with preparatory inspiration (With Prep Insp) and without preparatory inspiration (Without Prep Insp) for each of the contrasts considered (BOLD, BOLD _{ASL} and CBF).	56
Figure 3.31: Bar chart of the mean number of responsive voxels across subjects using the BH protocol with preparatory inspiration (With Prep Insp) and without preparatory inspiration (Without Prep Insp) for each of the contrasts considered (BOLD, BOLD _{ASL} and CBF).	56
Figure 3.32: Bar chart of global delays of each subject using the BH protocol with preparatory inspiration (With Prep Insp) and without preparatory inspiration (Without Prep Insp) for each of the contrasts considered (BOLD, BOLD _{ASL} and CBF).	57
Figure 3.33: Bar chart of the mean CVD values across subjects using the BH protocol with preparatory inspiration (With Prep Insp) and without preparatory inspiration (Without Prep Insp) for each of the contrasts considered (BOLD, BOLD _{ASL} and CBF). * represents significant differences (p<0.005).	58
Figure 3.34: Bar chart of global reactivity values of each subject using the BH protocol with preparatory inspiration (With Prep Insp) and without preparatory inspiration (Without Prep Insp) for each of the contrasts considered (BOLD, BOLD _{ASL} and CBF).	59
Figure 3.35: Bar chart of the mean CVR values across subjects using the BH protocol with preparatory inspiration (With Prep Insp) and without preparatory inspiration (Without Prep Insp) for each of the contrasts considered (BOLD, BOLD _{ASL} and CBF).	59
Figure 3.36: Sum of all subject masks, overlaid on the T1-weighted structural image of the MNI standard brain.	61
Figure 3.37: Mean CVD map of BOLD _{ASL} responses across subjects, in the MNI standard space. Delays are in seconds.	61
Figure 3.38: Mean CVR map of BOLD _{ASL} responses across subjects, in the MNI standard space. Reactivity is in percentage.	61

Figure 3.39: Map of number of subjects exhibiting a significant BOLD _{ASL} response, in the MNI standard space.	62
Figure 3.40: Standard deviation of the values of CVD of BOLD _{ASL} responses across subjects, in the MNI standard space.	62
Figure 3.41: Mean CVD map of CBF responses across subjects, in the MNI standard space. Delays are in seconds.	62
Figure 3.42: Mean CVR map of CBF responses across subjects, in the MNI standard space. Reactivity is in percentage.....	63
Figure 3.43: Map of number of subjects exhibiting a significant CBF response, in the MNI standard space.	63
Figure 3.44: Standard deviation of the values of CVD of CBF responses across subjects, in the MNI standard space.	63
Figure 3.45: Mean of CVD values of subjects across specific brain regions. Error bars represent standard deviations of the mean.	64
Figure 3.46: Mean of CVD values across specific brain regions for each subject. Error bars represent standard deviations of the mean. GM and WM correspond to grey matter and white matter, respectively.....	64
Figure 3.47: Mean of CVR values across specific brain regions for each subject. Error bars represent standard deviations of the mean. GM and WM correspond to grey matter and white matter, respectively.....	65
Figure 3.48: Mean of CVD values across specific brain regions. Error bars represent standard deviations of the mean. GM and WM correspond to grey matter and white matter, respectively.....	65
Figure 3.49: Mean of CVR values across specific brain regions. Error bars represent standard deviations of the mean. GM and WM correspond to grey matter and white matter, respectively.....	65
Figure 3.50: Sum of all subject masks, overlaid on the T1-weighted structural image of the MNI standard brain.....	66
Figure 3.51: Mean CVD map of BOLD _{ASL} responses across subjects, in the MNI standard space. Delays are in seconds.	67
Figure 3.52: Mean CVR map of BOLD _{ASL} responses across subjects, in the MNI standard space. Reactivity is in percentage.....	67
Figure 3.53: Map of number of subjects exhibiting a significant BOLD _{ASL} response, in the MNI standard space.	67
Figure 3.54: Standard deviation of the values of CVD of BOLD _{ASL} responses across subjects, in the MNI standard space.	68
Figure 3.55: Mean CVD map of CBF responses across subjects, in the MNI standard space. Delays are in seconds.	68
Figure 3.56: Mean CVR map of CBF responses across subjects, in the MNI standard space. Reactivity is in percentage.....	68
Figure 3.57: Map of number of subjects exhibiting a significant CBF response, in the MNI standard space.	69

Figure 3.58: Standard deviation of the values of CVD of CBF responses across subjects, in the MNI standard space.	69
Figure 3.59: Mean and standard deviation of CVD values in seconds of specific regions of the brain.....	69
Figure 3.60: Mean of CVD values across specific brain regions for each subject. Error bars represent standard deviations of the mean. GM and WM correspond to grey matter and white matter, respectively.....	70
Figure 3.61: Mean of CVR values across specific brain regions for each subject. Error bars represent standard deviations of the mean. GM and WM correspond to grey matter and white matter, respectively.....	70
Figure 3.62: Mean of CVD values across specific brain regions. Error bars represent standard deviations of the mean. GM and WM correspond to grey matter and white matter, respectively.....	71
Figure 3.63: Mean of CVD values across specific brain regions. Error bars represent standard deviations of the mean. GM and WM correspond to grey matter and white matter, respectively.....	71
Figure 3.64: Time course of all subjects (left) and mean time course of all subjects (right) averaged over the BH with preparatory inspiration challenge blocks for BOLD signal. Subject R1 data was not used in this analysis due to high levels of motion.	72
Figure 3.65: Time course of all subjects (left) and mean time course of all subjects (right) averaged over the BH with preparatory inspiration challenge blocks for BOLD _{ASL} signal. Subject R3 data was not used in this analysis due to high levels of motion.	72
Figure 3.66: Time course of all subjects (left) and mean time course of all subjects (right) averaged over the BH with preparatory inspiration challenge blocks for CBF signal. Subject R3 data was not used in this analysis due to high levels of motion.	72
Figure 3.67: Time course of all subjects (left) and mean time course of all subjects (right) averaged over the BH without preparatory inspiration challenge blocks for BOLD signal.....	73
Figure 3.68: Time course of all subjects (left) and mean time course of all subjects (right) averaged over the BH without preparatory inspiration challenge blocks for BOLD _{ASL} signal.....	73
Figure 3.69: Time course of all subjects (left) and mean time course of all subjects (right) averaged over the BH without preparatory inspiration challenge blocks for CBF signal.	74

List of Tables

Table 3.1: $P_{ET}CO_2$ values in mmHg during BH challenge without preparatory inspiration (left) and with preparatory inspiration (right).....	34
Table 3.2: Mean head motion in mm during acquisitions	35
Table 3.3: Number of responsive voxels for each subject using the two modelling approaches (SDO and SCC), for each of the contrasts considered (BOLD, $BOLD_{ASL}$ and CBF).	37
Table 3.4: Global delay values in seconds for each subject using the two modelling approaches (SDO and SCC), for each of the contrasts considered (BOLD, $BOLD_{ASL}$ and CBF).	38
Table 3.5: CVR values in percent signal change for each subject using the two modelling approaches (SDO and SCC), for each of the contrasts considered (BOLD, $BOLD_{ASL}$ and CBF).	45
Table 3.6: Correlation between CVR values and $P_{ET}CO_2$	46
Table 3.7: Number of responsive voxels for each subject using the two BH protocols for each of the contrasts considered (BOLD, $BOLD_{ASL}$ and CBF).	55
Table 3.8: Global delay values in seconds for each subject using the two BH protocols, for each of the contrasts considered (BOLD, $BOLD_{ASL}$ and CBF).	57
Table 3.9: CVR values in percent signal change for each subject using the two BH protocols, for each of the contrasts considered (BOLD, $BOLD_{ASL}$ and CBF).....	58

List of Acronyms and Abbreviations

ACA	Anterior Cerebral Artery
ACZ	Acetazolamide
ASL	Arterial Spin Labelling
BET	Brain Extraction Tool
BH	Breath Hold
BOLD	Blood Oxygenation Level Dependent
CBF	Cerebral Blood Flow
CBV	Cerebral Blood Volume
CMRO₂	Cerebral Metabolic Rate of Oxygen
COPE	Contrast of Parameter Estimate
CPP	Cerebral Perfusion Pressure
CVD	Cerebrovascular Delay
CVR	Cerebrovascular Reactivity
EEG	Electroencephalography
EPI	Echo-Planar Imaging
EV	Explanatory Variable
FAST	FMRIB's Automated Segmentation Tool
FEAT	FMRI Expert Analysis Tool
FILM	FMRIB's Improved Linear Model
FLIRT	FMRIB's Linear Registration Tool
fMRI	Functional Magnetic Resonance
FMRIB	Oxford Centre for Functional Magnetic Resonance Imaging of the Brain
FSL	FMRIB Software Library
FWHM	Full Width Half Maximum
GLM	General Linear Model
MCA	Middle Cerebral Artery
MCFLIRT	FMRIB's Motion Correction tool
MRI	Magnetic Resonance Imaging
PASL	Pulsed Arterial Spin Labelling
PCA	Posterior Cerebral Artery
PE	Parameter Estimate
PET	Positron Emission Tomography
P_{ET}CO₂	End-Tidal CO ₂ pressure
PSC	Percent Signal Change
RF	Radio Frequency
ROI	Region of Interest
SCC	Sine Cosine Linear Combination
SDO	Sine Delay Optimization
SNR	Signal-to-noise ratio

SPECT	Single Photon Emission Tomography
SPM	Statistical Parametric Map
T1	Longitudinal Relaxation Time
T2	Tranverse Relaxation Time
T2[*]	Spin-Lattice Relaxation Time
TDU	Transcranial Doppler Ultrasound
TE	Echo Time
TI	Inversion Time
TR	Repetition Time
Xe-CT	Xenon Computed Tomography

1

Introduction

This work addresses the characterization of the cerebrovascular reactivity spatiotemporal dynamics, as measured by both the cerebral blood flow (CBF) and blood oxygen level-dependent (BOLD) responses to two different breath-hold (BH) challenges using functional Magnetic Resonance Imaging (fMRI). This is achieved by estimating the corresponding cerebrovascular reactivity amplitudes (CVR) and associated cerebrovascular delays (CVD). Two different modelling approaches are used to analyse the data: Sine Optimization Delay (global) and Sine Cosine Linear Combination (voxel-by-voxel). The results of the two models and the two different breath-hold paradigms are compared.

The physiological concepts related to the parameters of interest and the techniques employed to assess them will be analysed in Section 1.1. Section 1.2 will introduce a series of concepts about the basic principles of Magnetic Resonance Imaging, including statistical concepts. After that, Section 1.3 will provide the state of the art. The dissertation goals and outline will be given in Section 1.4 and the contributions arising from this Work will be enumerated in Section 1.5.

1.1. Physiological Principles

The following sections are going to describe the parameters of interest, CVR and CVD, and the techniques employed to assess them.

1.1.1. Cerebrovascular Reactivity and Cerebrovascular Delay

In physiology, the term cerebral blood flow (CBF), also known as cerebral perfusion, describes the process of delivery of oxygen and nutrients to a capillary bed by means of arterial blood flow. This parameter is usually measured in units of millilitres of blood per 100 grams of tissue per minute (ml/100g/min) [1][2]. The typical average value of CBF in the human brain is 50ml/100g/min, with grey matter having an average value three times higher than white matter [3][4].

CBF varies directly with cerebral perfusion pressure (CPP), which is defined as the difference between mean arterial and intracranial pressures, and varies inversely with cerebrovascular resistance (CVRe) (Equation 1.1).

$$CBF = \frac{CPP}{CVRe} \quad (1.1)$$

Cerebrovascular Reactivity (CVR) can be seen as a unique physiologic parameter that reflects the intrinsic autoregulatory capacity of the brain to alter its vasculature in order to compensate for systemic perturbations and maintain the supply of oxygen and nutrients constant (by altering the CBF). Autoregulation mechanisms include both the capacity to reduce the vascular resistance through vasodilation, in cases of decreased CPP, and the ability to increase the vascular resistance, by vasoconstriction, in cases of increased CPP [5]. The associated cerebrovascular delays (CVD) reflect the time taken for an appropriate CBF change to occur in response to a vascular challenge. However, the physiological mechanisms underlying autoregulation of CBF are still not well understood. Most likely, the autoregulatory vessel caliber changes are mediated by an interplay between myogenic and metabolic mechanisms. CBF autoregulation typically operates between mean blood pressures of the

order of 60 and 150 mm Hg [6]. These limits are not entirely fixed; in fact blood pressure fluctuations may produce slight changes in CBF even beyond these thresholds.

Disease states of the brain may impair or abolish CBF autoregulation. Impaired CVR has been shown to be associated with several pathological conditions, particularly hypoperfusion cerebrovascular disorders such as arterial stenosis/occlusion and Moyamoya disease [7][8].

It has been suggested that CVR assessment can be an important tool for treatment decision, by helping, for example, in the identification of patients that are at higher risk of stroke and that would benefit from a specific treatment for stenosis/occlusion, such as artery bypass or the angioplasty and stenting. In patients with Moyamoya disease, CVR assessment may be useful to define the areas at higher risk and guide surgical treatment [5].

Furthermore, it has been reported that even in healthy subjects there are regional differences in vascular reactivity and corresponding delays, reflecting regional differences in cerebral vascular tone, rendering the investigation of CVR and CVD distribution across the brain of great importance [9][10]. Also, CVR evaluation can be useful to assess neurovascular coupling integrity, to be used as a parameter for characterization of neurodegenerative disorders, such as dementia, or simply to validate fMRI results [5].

The assessment of CVR and CVD can be performed by employing a challenge to the brain vasculature and measuring the associated CBF changes using an appropriate imaging modality. Currently, there are several types of challenges and a number of different methods to assess CBF changes, which will be described in the next two sections.

1.1.2. Vasoactive Challenges

Cerebrovascular reactivity can be measured by employing different types of challenges that induce vasodilation or vasoconstriction and therefore elicit a corresponding increase or decrease in CBF. The ideal challenge for CVR assessment should be noninvasive, safe and isometabolic, that is, it should not cause any changes in the cerebral metabolic rate of oxygen (CMRO₂). Moreover, it should produce a CBF change that is measureable in a reproducible way using an appropriate imaging method [5].

The most common approaches to induce global cerebral vasodilation involve the intravenous injection of vasodilator drugs, like Acetazolamide [11], or the induction of hypercapnia by inhalation of CO₂ mixtures [12] or breath-holding techniques [13][14].

The vasodilatory substance Acetazolamide (ACZ) is a selective inhibitor of carbonic anhydrase that, by concerting bicarbonate and hydrogen into water and carbon dioxide, decreases the pericellular pH (local acidosis) and consequently causes vasodilation [15]. The use of ACZ is a more robust challenge than hypercapnia-based methods, but the ACZ formula needed for these types of studies isn't widely available.

Hypercapnia-based methods rely on the fact that, in arterial blood, CO₂ is a potent vasodilator. By inducing an increase in the arterial partial pressure of CO₂ (PaCO₂), CBF increases are therefore produced. It is estimated that a 1 mmHg PaCO₂ change results in a 4% change in CBF [16]. On the contrary, a reduction in PaCO₂ causes a decrease in CBF. These relations are depicted in Figure 1.1.

It is accepted that the vascular response is mediated by changes in extracellular pH [5][17], which induce alterations in smooth muscle tissue.

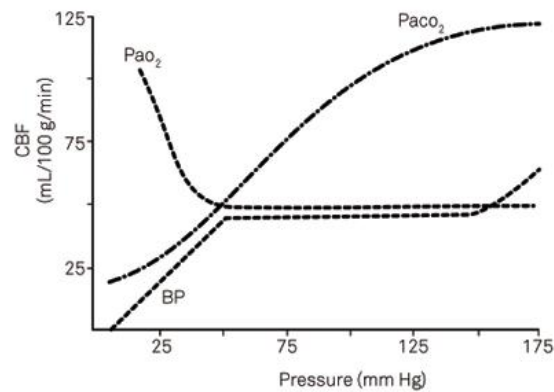


Figure 1.1: Cerebrovascular autoregulation and the effect of blood gases on CBF. An increase in arterial partial pressure of CO₂ (PaCO₂) induces an increase in CBF. Retrieved from [17].

One method to induce an increase in PaCO₂ consists of the inhalation of CO₂ mixtures with an increased CO₂ fraction (usually between 4 and 8%) [18][19][20]. Concentrations greater than 7% were reported to be exhausting [21]. The inhalation of CO₂ mixtures involves the use of a breathing apparatus that generally consists of a Douglas bag, that contains the gas mixture, and a two way valve attached to a mouthpiece combination [20].

Another method that induces an increase in PaCO₂ is the Breath Holding (BH) challenge. This method was initially proposed by Ratnatunga and Adiseshiah in 1990 [22] and consists on holding one's breath for a few seconds and then breathing normally. This cycle is repeated several times depending on the type of analysis. The timing of the holding and the regular-breathing periods are usually indicated by visual or auditory cues. The PaCO₂ increases during breath-holding, leading to a hypercapnia condition and consequently to a CBF increase.

Generally, the CBF time courses measured during breath-hold challenges exhibit a main peak that corresponds to the CBF increase motivated by the associated hypercapnia. However, the exact shape of the time course may differ between different BH protocols, in particular depending on whether or not a preparatory inspiration is performed before breath-hold. When using preparatory inspiration, the rise of CO₂ concentration in the blood after the breath-hold is not immediate, hence a time shift between breath-hold and CBF response must be expected, and due to the initial respiratory act it is difficult to determine exactly when the CO₂ accumulation triggered the brain autoregulatory response [23]. Moreover, CBF variations related with the inspiration act itself, due to factors such as reduction of pulmonary vascular tension, variation of heart rate and automatic modulation of cerebral myogenic autoregulatory responses, may also be present in the observed response [24][25].

Regarding the comparison between BH challenges and CO₂ inhalation, it has been demonstrated that both tasks provide similar vascular responses [12]. However, BH is a simple and completely noninvasive approach that does not require an exogenous CO₂ source. In fact, CO₂ inhalation may not be tolerated by elderly subjects and subjects with pulmonary diseases, for example. Nevertheless, there are some factors that should not be forgotten when using the BH task to assess CVR. Firstly, the subjects have to be able to understand and perform the task properly, and may therefore not be

appropriate for patients with cognitive deficits. Secondly, the complex dynamics associated with the act of breath-holding can trigger unwanted local CBF and oxygenation changes due to neuronal activation. Moreover, it is not possible to control for the rise rate of PaCO₂ achieved by each subject, which may lead to increased intersubject variability. Also, inconsistency in the depth of a preparatory inspiration within a single BH paradigm can also reduce the effectiveness of the measurement [26]. To avoid this, CBF measurements can be correlated with measurements of the end-tidal CO₂ pressure (P_{ET}CO₂) and/or other breathing parameters such as the respiratory volume. Recently, and in order to diminish inter and intrasubject variability, a study applied a method to control inspiration level through visual cues during the BH task paradigm. It achieved greater inter-trial reliability by reducing measurement variance [26]. Despite these potential disadvantages, studies performed in young children and elderly subjects indicate that BH can be effectively used to measure regional vascular reactivity in populations that are generally considered more difficult to train and acquire data from [27][10].

Besides vasodilating challenges that increase the CBF, vasoconstricting challenges can also be used when assessing CVR. Hyperventilation induces hypocapnia and O₂ administration leads to vasoconstriction and consequently decreased CBF [28]. Cued deep breathing is a new alternative method that has been developed to cause transient mild hypocapnia, and consequently vasoconstriction [29].

All CBF alterations induced by these techniques can be assessed using several methods that are going to be described in the next section.

1.1.3. Measurement Techniques

The main imaging methods that have been successfully used to assess CVR will now be described.

Transcranial Doppler Ultrasound (TDU) uses ultrasound waves to measure blood flow velocity through cerebral vessels with large caliber, based on the Doppler effect. Mean flow velocity can then be used as an indirect estimation of CBF [30]. Because of the much higher acoustic impedance of bone, only a few windows for ultrasound transmission exist across the skull. In particular, the temporal window allows measurement of flow velocity in the middle cerebral arteries. TDU is one of the most commonly used techniques for measuring CVR in clinical settings because it is widely available and inexpensive. However, this method depends on the presence of an adequate acoustic window and it can only measure the velocity changes in middle-sized arteries and therefore cannot evaluate the regional CBF and hence CVR across the brain [31][32].

A number of CBF imaging techniques are based on the measurement of the concentration of a radioactive compound that is administered in the circulation and diluted in the blood, hence acting as a CBF tracer. By application of appropriate tracer kinetic theory, it is then possible to quantify CBF based on the tracer concentration-time curves. Xenon computed tomography (Xe-CT) is based on the inhalation of xenon 133 gas, which is a radioactive, diffusible CBF tracer. Xe-CT provides quantitative CBF and hence CVR measurements. However, it requires the inhalation of an expensive radioactive gas making it invasive and expensive [32]. Using the same tracer kinetics principles, CBF can in principle also be measured by Positron Emission Tomography (PET) through the administration of

^{15}O -labelled water and oxygen. However, the requirement of an onsite cyclotron, extremely high costs and use of ionizing radiation severely limit the clinical applicability of this technique [33]. Single-photon emission computed tomography (SPECT) is probably the nuclear medicine technique most widely available for cerebral hemodynamics assessment. It is used to measure CBF using tracer kinetic theory, but like PET it involves the administration of a radioactive tracer, is expensive and provides poor spatial resolution [34].

More recently, it has become possible to evaluate CVR non-invasively and with relatively higher spatial and temporal resolutions by magnetic resonance imaging (MRI), using the Blood Oxygen Level Dependent (BOLD) contrast [15][8][7]. Even though the BOLD signal depends on several physiological parameters such as CBF, cerebral blood volume (CBV) and blood oxygenation, it is assumed that this contrast reflects predominantly CBF changes in the normal brain [7]. Truly quantitative CVR measurements can only be obtained if a perfusion-weighted signal is acquired, which can be achieved using the non-invasive technique of Arterial Spin Labelling (ASL) [35][36]. Previous ASL studies have focused mainly on determining baseline CBF values and CBF changes during brain activation. Only a very few studies to date have employed ASL for the study of CVR, either in healthy volunteers or clinical populations [13][7][37].

The basic concepts of fMRI and these types of techniques (BOLD and ASL) will be described in detail in the next section.

1.2. Functional Magnetic Resonance Imaging Principles

In a strict sense, fMRI usually refers to a functional imaging technique based on the BOLD contrast that allows measurement of brain activity by assessing the associated changes in haemodynamics (CBF, CBV and blood O_2 saturation) over time. However, in a broader sense, fMRI can be used to refer to all imaging techniques that reflect some functional aspect of the brain, particularly its haemodynamics. In this sense, fMRI can be based on both BOLD and ASL signals. Moreover, it can also be used to assess changes in haemodynamics in response to isometabolic vascular challenges. All MRI, including fMRI, relies on a set of physical principles that were discovered by Rabi, Bloch, Purcell and other pioneers during the first half of the twentieth century [38]. In this section these basic physical principles of MRI signal will be briefly described.

1.2.1. MRI Basic Principles

It is known that all matter is composed of atoms. Atomic nuclei contain two types of particles, protons and neutrons, and these constituents are known to possess a quantum property called spin, related to the magnetic moment. If a nucleus contains an odd number of protons and/or of neutrons, it exhibits a nonzero nuclear spin (examples: ^1H , ^{13}C , ^{14}N). In contrast, nuclei that have even number of protons and even number of neutrons have a total nuclear spin of zero and consequently no magnetic resonance signal (examples: ^{12}C , ^{16}O). Generally, hydrogen-1 nuclei (^1H) are the ones elected when studying biological tissues with MRI because, besides having the property of spin, they are a constituent of water, the most abundant substance in the human body.

At rest, in the absence of a magnetic field, non-zero magnetic moment nuclei are randomly oriented and the resulting magnetization vector M is equal to zero. However, when submitted to a

strong static magnetic field, B_0 , the nuclei achieve a relatively organized state, in which each nucleus adopts one of the $2I + 1$ energy levels (I is the nuclear spin quantum number, characteristic of each nucleus). Each energy level corresponds to a specific orientation relatively to B_0 .

In the case of ^1H nuclei, $I=1/2$ so the spins will be distributed into two energy levels, one parallel to B_0 with lower energy and another anti-parallel to B_0 with higher energy. Given the tissue's temperature, thermal agitation and typical field strengths, more spins tend to align in the parallel state rather than in the anti-parallel, so overall, there will be a net macroscopic magnetization which is parallel to B_0 .

If a second magnetic field, B_1 , transverse to B_0 and usually in the radiofrequency band, is applied, the nuclei get excited, changing their state to a higher one, creating a magnetization component in the transverse plane. But this excitation only occurs when the radiofrequency waves applied have a specific frequency entitled Larmor frequency. The Larmor frequency is proportional to the nucleus gyromagnetic constant γ and the magnetic field strength B_0 (Equation (1.2)). Each kind of nucleus has a specific gyromagnetic ratio and consequently, is only excited by a unique frequency.

$$\nu = \gamma B_0 \quad (1.2)$$

When the excitation is over, and the atomic nuclei return to the equilibrium, this transition from a high energy to a low energy level is accompanied by energy emission at the same Larmor frequency, that is recorded corresponding to the MRI signal [38].

This mechanism of relaxation is characterized by local magnetic field changes in two dimensions, longitudinal (parallel to the magnetic field) and transversal (perpendicular to the magnetic field). Both processes can be characterized by exponential functions and depend on specific time constants. These constants are also tissue specific [39].

The longitudinal component, also called spin lattice relaxation, approaches the maximum value (equilibrium value) with the time constant T_1 , longitudinal relaxation time (Equation (1.3)).

$$M_z(t) = M_z(0) \left(1 - e^{-\frac{t}{T_1}}\right) \quad (1.3)$$

This relaxation corresponds to the re-establishment of thermal equilibrium involving the transfer of energy of free water spins to the surrounding environment, the lattice.

The transverse component, also called spin-spin relaxation, vanishes with a different time constant, T_2 , transverse relaxation time (Equation (1.4)).

$$M_{xy}(t) = M_{xy}(0) e^{-\frac{t}{T_2}} \quad (1.4)$$

This relaxation results from the interaction of the different hydrogen nuclei that lead to a coherence loss in the spin phase of the nuclei, i.e. their magnetization vectors rotate at different speeds, cancelling their contributions to the net magnetization.

The nuclei also experience another mechanism of loss of transversal magnetization caused by inhomogeneities in the surround magnetic field, particularly in regions with boundaries between tissues with different magnetic susceptibilities, leading to an increase of the loss of spin coherence

between the different nuclei spins and accelerated signal decay. This process is defined as T_2^+ and is usually seen as an additive process to the T_2 relaxation. Their joint effect is known as T_2^* (Equation (1.5)), which is smaller than the T_2 alone [39].

$$\frac{1}{T_2^*} = \frac{1}{T_2} + \frac{1}{T_2^+} \quad (1.5)$$

In the brain, these inhomogeneities depend on the physiological state of the brain, predominantly on the composition of local blood supply, which is related to neural activity. This interaction will be described with more detail in the next section.

Finally, and to summarize the concepts introduced, we can describe magnetic resonance phenomena in a single equation, the Bloch Equation (Equation (1.6)), that demonstrates that the magnetization vector of a spin system processes around the main magnetic field axis at the Larmor frequency, with its change in the longitudinal plane governed by T_1 and its change in the transverse plane governed by T_2 .

$$\frac{d\vec{M}}{dt} = \gamma \vec{M} \times \vec{B} + \frac{1}{T_1} (\vec{M}_0 - \vec{M}_z) - \frac{1}{T_2} (\vec{M}_x \times \vec{M}_y) \quad (1.6)$$

The coils placed within the MR scanner measure the changes in the local magnetic field and by applying different acquisition sequences, it is possible to obtain images pondered in the different parameters, T_1 , T_2 and T_2^* .

1.2.2. Blood Oxygenation Level Dependent Contrast

The most abundant cells in human blood are red blood cells (or erythrocytes). These cells contain a protein called haemoglobin. In 1936, Pauling and Coryell discovered that haemoglobin can behave as a diamagnetic substance when bound to oxygen or as a paramagnetic substance when deoxygenated [40].

A change in the blood oxygen saturation will affect the relative concentrations of oxygenated and deoxygenated haemoglobin and will therefore affect the local magnetic susceptibility of blood. Changes in local magnetic susceptibilities will produce distortions in the applied magnetic field and hence will cause spin dephasing. As a result, the time constant T_2^* will be reduced and the signal measured using magnetic resonance pulse sequences sensitive to T_2^* will drop. Therefore, T_2^* MRI should show more signal when blood is more oxygenated and less signal when blood is deoxygenated, that is, the signal will increase with blood oxygen saturation. This is the so-called blood oxygenation level dependent (BOLD) contrast mechanism, and it was first described in 1990 by Ogawa and his co-workers [41]. The BOLD contrast is usually achieved by employing fast, strongly T_2^* -weighting MRI pulse sequences, particularly echo planar imaging (EPI) with a relatively long echo time [42].

At first glance, as consequence of neural activation, it would be expected an increase in metabolic demands and thus an increase in oxygen consumption. This would increase the amount of deoxyhemoglobin and consequently it would be detected a decreased of the BOLD contrast signal. However, it is observed a signal increase during brain activation. This is explained by the mismatch

between the increases in blood flow and O_2 metabolism during brain activation. CBF increases much more than $CMRO_2$, as a result, the delivery of O_2 to the capillary bed is increased, but less is removed from the blood, delivering an oversupply of oxygenated blood [1]. The fall in deoxyhemoglobin concentration leads to the signal increase. This mismatch led to further investigations to determine the coupling between neural activation and BOLD signal, however, this matter still is not completely known.

The BOLD contrast does not reflect a single physiological process, but rather represents the combined effects of CBF, CBV and blood oxygenation [43][44]. Although the complex nature of BOLD signal makes it difficult to interpret, imaging sequences based on the BOLD contrast are still the predominant method used for fMRI brain activation studies. Additional information (e.g., direct CBF measurements) can be extremely useful when trying to compare the magnitude of BOLD responses across brain regions, subjects or pathological states.

1.2.3. Arterial Spin Labelling

Arterial Spin Labelling (ASL) is a relatively new and extremely appealing MRI technique for measuring blood perfusion. ASL takes advantage of the high abundance of water molecules in the human body and, cleverly, uses magnetically labelled blood water protons as an endogenous CBF tracer. This allows repeated perfusion measurements. Furthermore, contrarily to BOLD methods, which are sensitive to changes in blood oxygenation depending on the combine effect of changes in CBF, CBV and O_2 saturation, ASL allows for the mapping of CBF changes directly and quantitatively.

The ASL technique's several stages are going to be described next in detail. The first step of the ASL technique is the labelling of arterial blood water molecules that are going to a region of interest (ROI) by saturating or inverting the longitudinal component, the Z-axis, of their magnetization. This tagged blood flows into the imaging slices or volume and relaxes toward equilibrium with the longitudinal relaxation time constant, T_1 of the blood [45]. After a delay, generally known as inversion time (TI), to allow for inflow of tagged blood, an image is acquired in the slice(s) or volume of interest. This image is referred as the tag image or label image. Another step is the acquisition of a second image in the same slice(s) or volumes, in a similar way but without the tagging process. In this case the blood is fully relaxed. This image is known as the control image. In the ideal case, the label and control images would be acquired at precisely the same time but since that cannot be made, tag and control images are typically acquired in a temporally interleaved way.

The subtraction of the control and tag images allows the removal of the contribution of the static tissue to the tag image and yields a magnetization difference image ($\Delta M = M_{\text{control}} - M_{\text{tag}}$) that is approximately proportional to CBF at sufficiently long acquisition times, In this case, the greater the flow into the imaging slices, the greater the signal changes in the tagged condition compared with the control condition. The exact relationship between the ASL ΔM signal and CBF can be derived by treating the magnetization difference, ΔM , as the concentration of a CBF tracer and applying appropriate tracer kinetics principles. The amount of magnetization difference present at time t will depend on the delivery of magnetization by arterial flow and the clearance of the magnetization by venous outflow and longitudinal relaxation [45]. The general kinetic model describing ΔM in pulsed ASL (PASL) is given by:

$$\Delta M(TI) = M_{0t} \frac{2\alpha f}{\lambda} \begin{cases} 0 & 0 \leq TI \leq \delta t \\ e^{-R_{1t}^{app} TI} e^{-D_1 \delta t} \frac{1 - e^{-D_1(TI - \delta t)}}{D_1} & \delta t \leq TI \leq \delta t + \tau \\ e^{-R_{1t}^{app} T_1} e^{-D_1 \delta t} \frac{1 - e^{-D_1 \tau}}{D_1} & \delta t + \tau \leq TI \end{cases} \quad (1.7)$$

with $D_1 = R_{1a} - R_{1t}^{app}$, $R_{1t}^{app} = \frac{1}{T_{1t}} + \frac{f}{\lambda}$ and $R_{1a} = \frac{1}{T_{1a}}$; where f is the CBF, δt is the arterial transit time, τ is the tag width, α is the labelling efficiency, defined as the fraction of inversion of the arterial magnetization at the time of tagging ($\alpha = 1$ for complete inversion); λ is the water partition coefficient between tissue and blood; T_{1a} and T_{1t} are the longitudinal relaxation time constants of arterial blood and tissue, respectively [46].

Several methods can be used to obtain a magnetization difference image. The simplest is the adjacent subtraction method and this is method is represented in Equation (1.8).

$$\left[P_1, P_2, \dots, P_{\frac{n}{2}} \right] = [C_1 - L_1, \quad C_2 - L_2, \dots, C_{\frac{n}{2}} - L_{\frac{n}{2}}] \quad (1.8)$$

C_i and L_i correspond to the control and labelling images respectively.

Other approaches, beyond simple subtraction, have been used in an attempt to minimize the effect of both random and systematic signal fluctuations in the source signal that are not the result of label [47]. One of these approaches is the surround subtraction (Equation (1.9)) and it dampens the effects of high-frequency changes in signal.

$$\left[P_1, P_2, \dots, P_{\frac{n}{2}} \right] = \left[C_2 - \frac{L_1 + L_2}{2}, C_3 - \frac{L_2 + L_3}{2}, \dots, C_{\frac{n}{2}} - \frac{L_{\frac{n}{2}-1} + L_{\frac{n}{2}}}{2} \right] \quad (1.9)$$

The greatest limitation of the ASL technique lies in its intrinsically very low signal-to-noise ratio, SNR, which can be alleviated by making more acquisitions due to the additive nature of the noise in the measurements. Generally, the signal produced by the delivery of blood is just about 1% of the total signal. Also there are several other confounds that should be taken into account when trying to produce accurate CBF maps. One of these confounds is the short lifetime of the label and the fact that blood requires some time to travel from the inversion band to the region of interest. For example, in some cerebrovascular diseases the delay of the inflowing blood may be so great that there is no signal left by the time the blood reaches the tissue. Another problem is the possibility of the region of interest imaged containing large vessels that are destined to perfuse a more distal capillary bed and not the imaged ROI. This can lead to an overestimate of local perfusion. Furthermore, the magnetization of the tagged blood decays in the time between the inversion/saturation pulse and the measurement, reducing the ASL signal. This decay rate is initially governed by the T_1 constant of the blood, but as water leaves the capillary bed and enters the extra-vascular space, this decay is governed by the T_1 constant of the tissue.

The ASL acquisition technique employed in this work was the quantitative imaging of perfusion using a single subtraction, second version with thin-slice T_1 periodic saturation, also known as Q2TIPS. It is an improved version of the pulsed ASL technique, QUIPSS II [48][36]. The QUIPSS II technique, by introducing a saturation pulse between the inversion pulse and the image acquisition, improves the quantification of perfusion imaging by minimizing two major systematic errors found in

conventional pulsed ASL techniques: the variable transit delay from the distal edge to the tagged region to the imaging slices and the contamination by intravascular signal from the tagged blood that flows through the imaging slices. However, residual errors remain in the experiment data. But, by replacing the original QUIPSS II saturation pulse with a train of thin-slice periodic saturation pulses applied at the distal end of the tagged region from TI_1 to TI_{1s} (Q2TIPS), the accuracy of perfusion quantification is improved [36]. The Q2TIPS sequence starts with a double in-plane pre-saturation pulse followed by a hyperbolic secant (sech) inversion tagging pulse. After the delay time TI_1 and before TI_{1s} (TI_1 stop time) periodic thin-slice saturation pulses are applied at the distal end of the tagged region. Finally, the image is acquired at time TI_2 by EPI (Echo Planar Imaging) acquisition. The general kinetic model describing ΔM for this sequence corresponds to Equation (1.7) when $TI \geq \delta t + \tau$.

ASL data are usually acquired with an EPI sequence. If sufficiently long echo times are used, the raw ASL images therefore also exhibit BOLD contrast. However, due to the fact that the echo time used in this type of acquisition is usually shorter than the ideal one, the perfusion time series that is obtained has weak BOLD weighting. In fact, previous reports have shown a reduction on the order of 15% in the BOLD signal acquired simultaneously with ASL compared with conventional BOLD measurements [36].

The advantages of ASL over other CBF measurement techniques are its complete non-invasiveness nature, its relatively high spatial and temporal resolution [47].

To obtain the $BOLD_{ASL}$ time series a surround average was computed, consisting of the average of each image with the average of its two nearest neighbours (Equation (1.10)).

$$\left[B_1, B_2, \dots, B_{\frac{n}{2}} \right] = \left[\frac{\left(\frac{C_1 + L_1}{2} + \frac{L_1 + C_2}{2} \right)}{2}, \frac{\left(\frac{L_1 + C_2}{2} + \frac{C_2 + L_2}{2} \right)}{2}, \dots \right] \quad (1.10)$$

1.2.4. General Linear Modelling

Analysis of fMRI data can generally be divided into model-based and model-free (data-driven) methods. In the former, a model of the expected response is generated and compared with the data, and in the latter, effects or components of interest in the data are found on the basis of some specific criteria. The General Linear Model (GLM) is a model-based method, which is the most common approach to fMRI data analysis. The GLM can be seen as a generalization of a multiple linear regression model. In this approach, several different statistical models can be incorporated, such as analysis of variance, ANOVA, analysis of covariance (ANCOVA), ordinary linear regression, t-test and F-test. Hypotheses testing with GLM can also be made using two different approaches: multivariate or univariate tests. Univariate models analyse each voxel's time series independently. In contrast, multivariate methods make use of spatial relationships within the data, and process all the information together. The GLM used in our fMRI study is univariate.

The GLM describes the observed data as a linear combination of model functions and a noise term. These model functions describe patterns that are expected to be seen in the data. It can be patterns related to effects of interest, but can be also confounds that are not related to the

experimental hypothesis [49]. A very simple example of general linear modelling is represented in Equation (1.11)

$$y(t) = \beta \times x(t) + e(t) \quad (1.11)$$

$y(t)$ corresponds to the observed data and is represented by a 1D vector of intensity values, one for each time point. $x(t)$ is the model chosen, also known as regressor or explanatory variable (EV). When there is only one regressor, $x(t)$ is also a 1D vector with a value for each time point. β is the parameter estimate (PE) for $x(t)$, i.e. the value that the regressor must be multiplied by to best fit the experimental data. This parameter weight indicates how much the model effect contributes to the observed data and is computed during the GLM analysis. The error term, $e(t)$, accounts for the residual error between the fitted model and the experimental data. This is assumed to be normally distributed such that the vector has a mean of 0, a variance σ^2 and correlation of 0 [50].

Equation (1.11) can be extended to include several regressors. Therefore, it is easier to formulate the GLM in matrix notation (Equation (1.12)).

$$Y = \beta X + e \quad (1.12)$$

This way, all of the model time-courses (explanatory variables, EVs) are grouped together into a matrix X , often referred as the design matrix, and parameter estimates (PE) are also grouped together into a vector β , such that each cell indicates the relative contribution of each component for the total signal. During GLM analysis, the combination of parameters that minimizes the noise term is calculated. The minimum error obtained is called residual error and this error, for a given voxel, must be combined across all time points into a single value. Each regressor in the design matrix results in a PE. This estimate tells you how strongly that regressor fits the data at each voxel. The higher it is, the better the fit. Contrasts of parameter estimates (COPE) are finally setup between specific EV's, expressing the effects of interest.

To evaluate the statistical significance of a model effect for a given voxel, it is necessary to convert COPEs into statistical maps and this is done by dividing the actual parameter estimate value (β_i) by the corresponding residual error. This results in a T-value.

$$T - value = \frac{\beta_i}{residual\ error} \quad (1.13)$$

In order to compare several contrasts at the same time, for example to see whether any of them (or any combination of them) is significantly non-zero, we use a F-test. Also, the F-test allows you to compare the contribution of each contrast to the model and decide on significant and non-significant ones [51]. After combining statistical tests of all voxels, the result is a statistical parameter map of activity for each explanatory variable. This map is then transformed into a Z-statistic image using standard statistical transformations, giving rise to a statistical parametric map (SPM).

A thresholding procedure is then applied according to a pre-defined level of statistical confidence.

If voxel thresholding is selected, GRF-theory-based maximum height thresholding is carried out, with thresholding at the level set, using one-tailed testing. When using cluster thresholding, a Z-

statistic threshold is used to define continuous clusters. Then each cluster's estimated significance level (from GRF theory) is compared with the cluster probability threshold. Significant clusters are then used to mask the original Z statistic image for later production of color blobs. Generally, the cluster thresholding method is more sensitive to activation in relation to the voxel-based correction. It is also possible to simply threshold the uncorrected Z statistic values, or to apply no thresholding at all [51].

By incorporating into the design matrix appropriate regressors of interest, and incorporating nuisance regressors that exclude unwanted variability, GLM has become a powerful and flexible technique for testing hypotheses. However, there are several assumptions that can lead to incorrect conclusions such as assuming that the design matrix (model) is the same throughout the brain. It is also assumed that the noise level is time invariant and there is a lack of use of spatial information, by analysing each voxel independently. Furthermore, conclusions are drawn assuming a given model and there is no guarantee that the model itself is appropriate.

1.3. State of the Art

In this section, the state of the art most closely relevant to the goals of this Thesis is presented, by first comparing the BOLD and ASL contrasts for fMRI, and then specifically reviewing the literature on CVR assessment using BOLD and ASL BH responses.

1.3.1. BOLD and ASL Sequences

Even though imaging sequences based on the BOLD contrast are still the predominant method for fMRI studies of the brain, ASL is contributing to the field's understanding of healthy and disordered brain in a new and improved way. Several studies were made in order to compare the ASL and BOLD data.

Firstly, it should be noted that the ASL perfusion signal measures a well-defined physiological quantity, CBF, whereas the BOLD signal is a complex function of CBF, blood oxygenation and CBV [45][44], even though it is thought to reflect predominantly CBF changes. Also, it was determined that ASL provides improved sensitivity relative to BOLD for low-frequency tasks [52], as the ASL processing methods make use of a differencing approach that minimizes the effects of low frequency signal drifts [47]. Both within- and between-subject variability have been found to be smaller when measured with ASL perfusion fMRI when compared with BOLD fMRI [45][53][54]. Perfusion changes have greater spatial specificity than BOLD changes during functional activation, suggesting that ASL may more accurately localize the region of neuronal activity [55][54]. Another study focused on the relative location of the activation areas with regard to proximal draining veins, showing bias for the BOLD signal to be shifted toward the venous compartment relative to the ASL contrast. It should, however, be noted that the venous contamination of BOLD signal can be reduced at high and ultrahigh field strengths [56].

Nevertheless, the biggest disadvantage of ASL relies on its intrinsic low SNR. Typically it is less than half that of the BOLD response [45]. Also, the temporal resolution of ASL methods is poorer than that of typical BOLD acquisitions because it requires the acquisition of two sets of images (tag and control) and also needs a waiting period to allow the inflow of blood into the imaging region.

Furthermore, the maximum number of slices acquired with ASL is usually less than that of BOLD due to the necessity to acquire data before the tagged blood signal has fully relaxed [45].

1.3.2. CVR assessment using BOLD and ASL BH responses

BH techniques have been successfully employed to measure CVR with fMRI, particularly using the BOLD contrast. Several studies were made to better understand the differences between subjects, different BH protocols, different sequences and regions of the brain.

Kastrup et al. measured regional BOLD responses using to a BH task [57]. BH-induced BOLD signal changes in the sensorimotor cortex, frontal cortex, basal ganglia, visual cortex, and cerebellum were significantly different and varied from 1.8 to 5.1%. The highest BOLD signal changes were found in the cerebellum and visual cortex, whereas the lowest BOLD signal increase was observed in the frontal cortex.

In another work by the same group, regional CBF changes in response to different BH protocols were assessed using an ASL sequence [13]. Repeated BH challenges induced an overall rise in CBF, which was greatest in grey matter and insignificant in white matter. Quantitative analysis yielded a CBF increase of 47% to 87% after BH. The CBF changes clearly depended on the BH duration and technique; however, for one given BH paradigm the results showed relatively small interindividual variability.

Chang et al. investigate the use of a BH task for characterizing and correcting for voxel-wise neurovascular latency differences across the whole brain using BOLD data [58]. They demonstrate that BH yields reliable measurements of relative timing differences between voxel. They noticed that several features of the latency maps (notably, delayed responses in the cerebellum as well as in major vessels, such as the sagittal sinus) were common across the group. They also showed that a BH-derived latency correction can impact both functional connectivity maps of the resting-state default-mode network and activation maps of an event-related working memory task.

Leoni et al. have quantitatively investigated the varied dynamics of BOLD response to hypercapnia in the different brain regions supplied by the main cerebral arteries, using two different BH protocols, one with BH after inspiration and another with BH after expiration [59]. They used an auto-regressive method that estimated three latency parameters (onset delay, full-width half maximum (FWHM), time-to-peak) and the response amplitude. The onset delay was significantly longer for the posterior cerebral artery (PCA) than for middle cerebral artery (MCA) and anterior cerebral arteries (ACA). FWHM and time-to-peak were larger in the ACA territory, indicating a slower blood flow in this region. Differences were also observed in the amplitude among the three areas, where MCA and PCA territories showed the smallest and the highest amplitudes, respectively. Moreover, differences were found in amplitude and onset when BH was performed after inspiration as compared to BH after expiration. Time-to-peak and FWHM showed no statistical differences between these two challenges. They observed a biphasic shape pattern in BH with inspiration.

Chu et al. evaluated quantitatively the dynamics of CBF changes in the same specific territories (ACA, MCA and PCA), following a hypercapnia BH challenge without inspiration, using an ASL technique, and compared the results with those obtained with BOLD contrast, through their time-courses and percent signal changes measurements [60]. In BOLD data, contrarily to the results found

by Leoni et al., MCA and PCA territories had greater signal changes than the ACA, whereas in ASL time courses the PCA had greater signal changes than the other two. PCA territory had a more delayed response than the ACA and MCA, which was consistent between BOLD and ASL.

Work done by Li et al. demonstrated that BOLD-weighted images showed lower values of signal intensity increase (1-4%) relative to CBF-weighted images (30-70%) [37]. They also found that the activated voxels in CBF-weighted images were about three times less than those seen in BOLD-weighted images. Signal intensities in both types of images were dependent on the breathing techniques used. BH after expiration gives rise to immediate signal intensity increase in BOLD and CBF weighted images, whereas BH performed after deep inspiration showed a biphasic change in both CBF and BOLD images. They state that these biphasic changes, due to inspiration, may be related to the effects of an incomplete Valsalva maneuver after deep inspiration. During this process a marked elevation of intrathoracic pressure will produce a transient rise in cerebral venous pressure, intracranial pressure, and venous pressure within the great veins, thus decreasing arterial blood pressure, CBF, and PaCO₂.

Another work done by Li et al. that used ASL with BH, as well as a finger tapping task, verified that the regulatory mechanisms for vasodilatory reaction to CO₂ and CBF response to neural activation in motor cortex region are independent [14].

Magon et al. studied the impact of having different BH periods (9, 15 and 21 sec) after inspiration [24]. Their data also showed that the BOLD response to breath holding after inspiration results in a complex shape due to physiological factors that influence the signal variation with a timing that is highly reproducible. Time courses, instead of having a biphasic shape, seem to have a triphasic shape. After an initial short positive phase, the signal became negative and then started increasing again, reaching the maximum peak within a variable delay depending on BH duration. Then, the signal smoothly decreased back to baseline with a variable delay.

Spatiotemporal dynamics were assessed by Blockley et al. using Fourier analysis techniques to measure both the amplitude and phase delay of the BOLD CVR response to CO₂ inhalation [61]. Their results show that frontal and parietal lobes reacted earlier than the occipital lobe.

It has been observed that it is possible to reduce variability of BOLD fMRI results of brain activation between subjects with different vasculature (children/adult, young/elderly), by correcting for CVR differences using BOLD BH measures [10] [27] [62].

1.4. Goals and approach

As previously stated, temporal dynamics and spatial variations of both BOLD and CBF responses to breath-holding challenges still remain relatively unexplored. Although a number of BH BOLD studies have been reported, only sparse and inconsistent results exist regarding the spatial variations of cerebrovascular delays across the brain. Most critically, no studies have been reported on either the temporal dynamics or the spatial variations of BH CBF responses measured directly using ASL.

The main goal of this work is to characterize the spatiotemporal dynamics of both the CBF and BOLD signals measured in response to two different breath-hold tasks, one with preparatory inspiration and one without preparatory inspiration. This is achieved by estimating two parameters,

cerebrovascular reactivity amplitudes (CVR) and associated cerebrovascular delays (CVD), using two different modelling approaches in a GLM framework: global delay optimization, the Sine Delay Optimization (SDO); and voxelwise delay estimation, the Sine Cosine Linear Combination (SCC). While the former corresponds to a widely used approach for modelling fMRI responses to BH protocols, the latter has been used in only one previous BOLD study [61]. Here, we employ this approach with the aim of better characterizing the spatiotemporal dynamics of both BOLD and CBF responses. A comparison between the two different modelling approaches will then be performed. Finally, the chosen modelling approach will be used to compare the two breath-hold protocols. The criteria chosen to compare the different modelling approaches / BH challenges are the number of responsive voxels, the cerebrovascular reactivity maps/values and the respective cerebrovascular delay maps/values. Also, the corresponding time courses are analysed.

1.4.1. Thesis Outline

In the first chapter an introduction of the theoretical concepts related with this work were presented. The remainder of this dissertation is organized as it follows: Chapter 2 is going to present the methods used in the data acquisition experiment, which include the acquisition sequences employed and the approaches chosen to model the data. Chapter 3 will then present the parameters estimated, a comparison between the analysis methods and the two BH protocols. Finally, Chapter 4 will provide the discussion and conclusions of the developed work.

1.5. Contributions arising from this work

We implemented a new method that allows the characterization of spatiotemporal dynamics of both BOLD and CBF responses to a BH paradigm and applied it to data collected from a group of 7 healthy volunteers. The results obtained with this new method were presented in two conferences:

- Pinto, J.; Jorge J.; Vilela, P.; Figueiredo, J.; “Spatiotemporal dynamics of the ASL CBF and BOLD responses to breath-holding”, Proceedings 29th Annual Scientific Meeting of the European Society of Magnetic Resonance in Medicine and Biology, October 2012 – Oral presentation
- Pinto, J.; Jorge J.; Vilela, P.; Figueiredo, J.; “Study of cerebrovascular dynamics using functional MRI”, Proceedings 18th Edition of the Portuguese Conference on Pattern Recognition, October 2012 - Poster presentation.

2

Methods

This chapter addresses the methods and materials used for the assessment of cerebrovascular reactivity and the corresponding cerebrovascular delays.

Two different BH protocols were employed, one with a preparatory inspiration and one without the preparatory inspiration. Also, two different types of data were acquired, BOLD and ASL.

Prior to statistical analysis, fMRI data underwent a series of standard pre-processing steps aiming to remove artefacts and to validate model assumptions.

Afterwards, GLM analyses were performed of the several types of data, BOLD with and without preparatory inspiration and ASL with and without preparatory inspiration, using two approaches: the Sine Delay Optimization and the Sine Cosine Linear Combination.

In the next sections, the several steps involved in data acquisition and data analysis are presented in detail.

2.1. Data Acquisition

The data used in this Thesis were acquired previously by the team (João Jorge, Pedro Vilela and Patrícia Figueiredo, Proc. Organization for Human Brain Mapping 2012 [63]) and the data acquisition details are described in the section.

2.1.1. Subjects and Tasks

A group of 7 healthy subjects (4M, age: 25.7 ± 9.8 years) was studied at Hospital da Luz.

Two different breath-hold challenges were employed during these BOLD/ASL acquisitions, which involved 20s periods of breath-holding with or without a preparatory inspiration. Previous studies have verified that breath-hold duration of approximately 20s yields an acceptable reproducibility of cerebrovascular maps and is associated with a lower dispersion of the magnitude of the response across subjects compare with lower breath-hold duration [24]. Throughout the experiment $P_{ET}CO_2$ was monitored using a capnograph in 3 subjects.

Both breath-hold tasks were presented to the subjects using a stimulus presentation software, NORDIC NEURO LAB's Nordic fMRI solution (www.nordicneurolab.com). The visual instructions used are represented in Figure 2.1 and Figure 2.2.



Figure 2.1: Breath-Hold without preparatory inspiration protocol presented to the subjects.

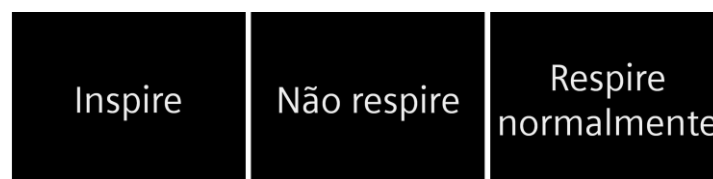


Figure 2.2: Breath-Hold with preparatory inspiration protocol presented to the subjects.

For the first challenge, without the preparatory inspiration, the breath-holding, “Não respire”, and the normal breathing, “Respire Normalmente”, instructions were shown during 20s and 55s, respectively. For the second challenge, with the preparatory inspiration, the inspiration, “Inspire”, and the breath-holding, “Não respire”, were shown during 20s and the normal-breathing, “Respire Normalmente”, was shown during 55s. The total length of each cycle was 75s for both challenges. Also, at the beginning of the experiments, a 50s period of normal breathing was acquired with the purpose of extracting a clean baseline for each subject.

Two different types of data were acquired, BOLD and ASL. ASL acquisition sequences, besides providing CBF contrast, also exhibit BOLD contrast ($BOLD_{ASL}$). An optimized BOLD acquisition was performed for comparison purposes. Figure 2.3 summarizes the different types of BH challenges employed, imaging sequences used, as well as the resulting types of signal contrast obtained.

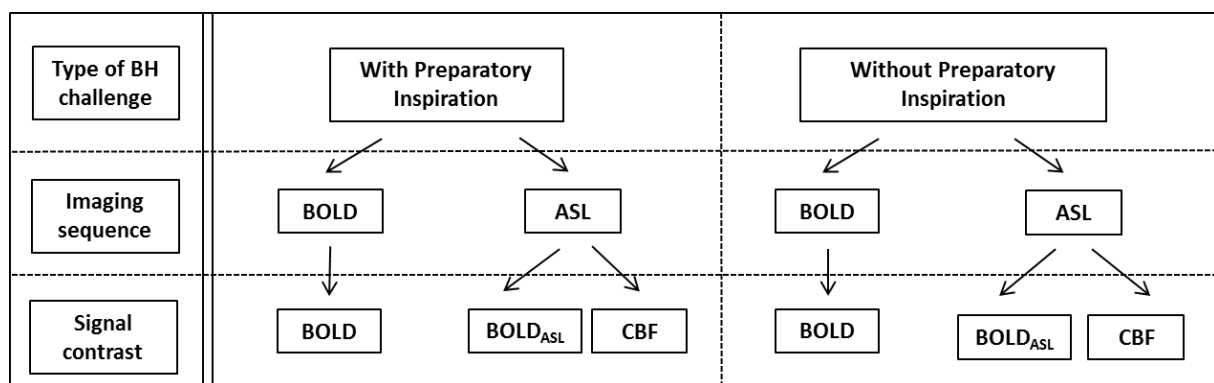


Figure 2.3: Summary of the different types of BH challenges and image acquisition sequences and resulting signal contrasts.

For the BOLD acquisition sequence, the BH/normal breathing cycles were repeated 3 times, yielding a total time of 275s (4 minutes and 35 seconds). For the ASL sequence, the cycles were repeated 8 times, yielding a total time of 650s (10 minutes and 50 seconds). The different numbers of repetitions used with the two sequences are related with the fact that the ASL CBF signal has much lower SNR than the BOLD signal, therefore requiring more averaging in order to yield sufficient sensitivity. Figure 2.4 and Figure 2.5 represent the breath-hold paradigms for the BOLD and ASL acquisitions.

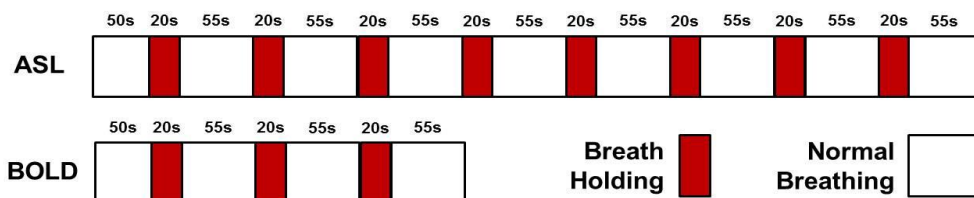


Figure 2.4: The breath-hold without preparatory inspiration time course for the BOLD and ASL protocols.

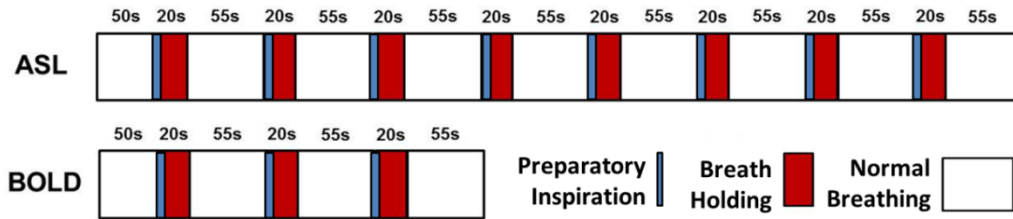


Figure 2.5: The breath-hold with preparatory inspiration time course for the BOLD and ASL data.

2.1.2. Acquisition Sequences

Imaging was performed on a 3T Siemens Verio scanner using a 12-channel radio frequency coil.

The BOLD images were obtained using a gradient echo – echoplanar imaging (GE-EPI) sequence, with repetition time (TR) of 2500ms, echo time (TE) of 50ms, collecting 110 brain volumes from 18 contiguous slices, with voxel resolution of $3.5 \times 3.5 \times 7.0 \text{ mm}^3$, yielding an image size of $64 \times 64 \times 18$.

Pulsed ASL data were collected using a PICORE-Q2TIPS sequence, with TR/TE=2500/25ms, T11/T11s/TI2=750/900/1700ms, collecting 261 brain volumes from 9 contiguous slices positioned parallel to the AC-PC line, with voxel resolution of $3.5 \times 3.5 \times 7.0 \text{ mm}^3$, yielding an image size of $64 \times 64 \times 9$.

A T1-weighted image was also acquired using an MP-RAGE sequence (TR/TE=2250/2.26ms, 144 slices, voxel resolution of $1 \times 1 \times 1 \text{ mm}^3$, image size $232 \times 256 \times 144$) in order to provide a high-resolution structural image for each subject.

During acquisitions subjects were submitted to a head restraint system of lateral padding in order to prevent head motion.

2.2. Data Analysis

Image analysis was conducted on both types of data, BOLD and ASL, using FMRIB Software Library (FSL 4.1.7, <http://fsl.fmrib.ox.ac.uk/fsl/fslwiki/FSL>) and self-written MATLAB routines (version 2011a, <http://mathworks.com>). In particular, pre-processing and statistical analysis steps were mainly conducted using FSL fMRI expert analysis tool (FEAT). This is an advanced model-based fMRI analysis tool, that allows data pre-processing, first-level general linear model (GLM) analysis, post-statistical thresholding, image registration and mixed-effects group analysis [10].

The steps applied to analyse the data will be described in detail over the next sections.

2.2.1. Pre-Processing

The structural images were first re-oriented to the same orientation as the functional images. Both structural and functional images were brain-extracted using the FSL brain extraction tool (BET) [64] before being used by FEAT. BET removes non-brain structures, such as the skull, from an image of the whole head. After performing BET extraction each brain was checked since the algorithm sets default coordinates as the centre of the brain. These coordinates may not correspond to the centre of the subject's head, so some coordinates were set by hand after careful visual analysis. An example of BET input and output is depicted in Figure 2.6.

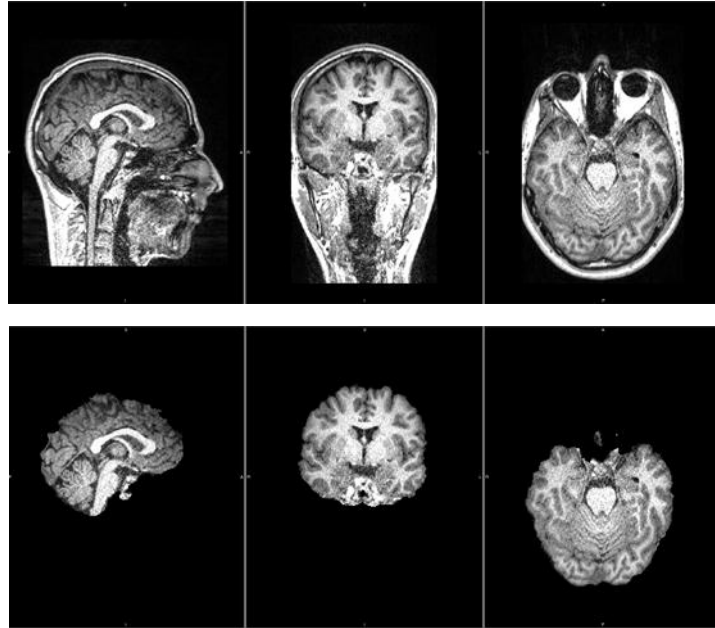


Figure 2.6: Example of a subject's structural images (left to right: coronal, sagittal and axial) before (top) and after (bottom) brain extraction using BET.

An important issue involved in any fMRI study is the proper handling of any subject movement that may have taken place during data acquisition, especially when handling data derived from respiratory challenges. For this reason, a motion correction step was applied to the 4D functional data. The MCFLIRT tool was used in order to remove the effect of subject head motion during the experiment. MCFLIRT is based on optimization and registration techniques used in FLIRT (FMRIB's Linear Registration Tool), an automated and robust tool for linear (affine) brain image registration [65]. An example of a motion correction report is represented in Figure 2.7.

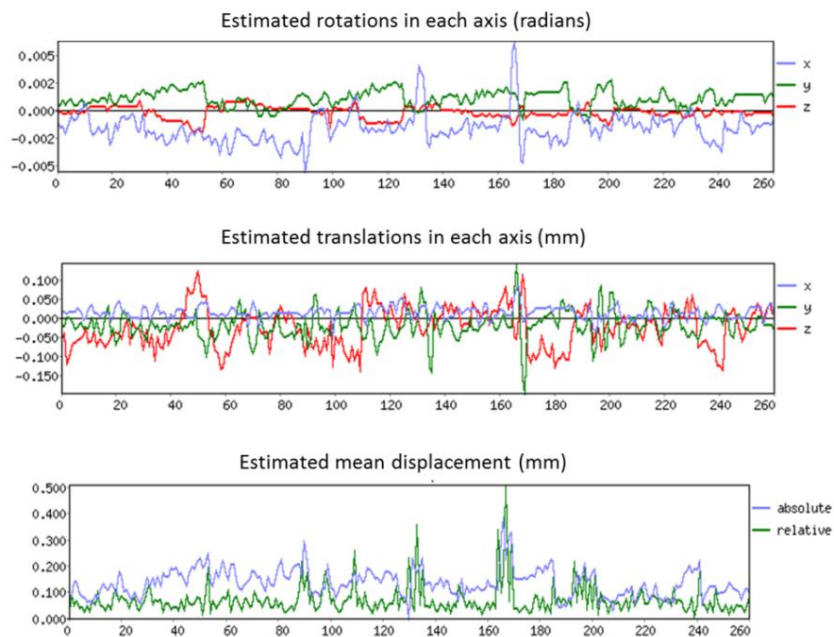


Figure 2.7: Motion correction results for one example subject. The relative displacement corresponds to the head position at each time point relative to the previous time point. The absolute displacement is calculated relative to the volume in the middle of the time series. The x axis represents the number of imaging volumes (TR=2.5s).

Each subject's motion correction report was verified in order to see if there was a pattern that could be correlated with the BH paradigm. However, MCFLIRT results showed no significant correlation with the BH task.

Temporal filtering was performed, using a 100 seconds high-pass filter cutoff for both BOLD and ASL signal. This cutoff controls the longest temporal period that it is allowed for the cycle time. In our analysis this filter was used to deprive the signal of the intrinsic low frequency drift and leave the event-related design intact. In general, the cutoff chosen should be higher or at least equal to the total time of the paradigm cycle. Since the paradigm used consisted in several 75s cycles, the value of 100s seemed appropriate. To be noted that in FEAT this value also affects the generation of the model, meaning that the same high pass filtering is applied to the model as to the data, to get the best possible match between them.

Spatial smoothing was employed to reduce the high-frequency noise spatial components, as well as to force the data to comply with the assumptions of Gaussian random field theory. It was carried out on each volume of the fMRI data set separately. This is done in order to reduce noise without reducing valid activation. However, this is only successful as long as the underlying activation area is larger than the extent of the smoothing value defined as FWHM. The FWHM chosen for the ASL data was 8 mm and for the BOLD data 5 mm. We chose a smaller value for the BOLD data because the signal is strong enough to appear in smaller activation regions.

Finally, fMRI images were analysed to determine the matrix parameters for image registration to a Montreal Neurological Institute (MNI) standard space. Registration is an essential step for presentation purposes or multi-subject analysis. This step was performed using FLIRT (FMRIB's Linear Image Registration Tool) [66]. Registration in FEAT is a several-stage process.

For the BOLD signal, the fMRI low-resolution image (the subject's 4D original image with BOLD contrast) is registered to an example high-resolution image (the same subject's T1-weighted structural image after brain extraction). Then the high-resolution image is registered to a standard space (in this case, the MNI 152 T1-weighted image). Finally the two transformations are combined into a third, which will take the low-resolution FMRI image straight into the standard space. All transformations are saved for posterior analysis.

For the ASL signal, the same transformations are applied to the data but an additional transformation is performed in the beginning. The low-resolution fMRI image (in this case the ASL 4D image) is first registered to an initial structural image (for example a 3D BOLD contrast image) and then this initial structural image is registered to the main structural image. This additional registration step is required because of the limited brain coverage of the ASL data (only 6.3 cm in the Z direction), in contrast with the full brain coverage of the BOLD data.

FMRIB's Automated Segmentation Tool (FAST) [67] was also used to segment the MNI image of the brain into different tissue types (grey matter, white matter and cerebrospinal fluid (CSF), for example). This was done in order to obtain specific regions of interest corresponding to the different types of tissue in the standard space, to allow further comparisons of the results between these regions.

2.2.2. General Linear Modelling

Time series analysis was performed for both types of data, BOLD and ASL, following a General Linear Model (GLM), using two different approaches: Sine Delay Optimization (SDO) and Sine Cosine Linear Combination (SCC). In both cases, the BOLD/CBF response to the BH paradigm is modelled by sinusoids, with the period of the task, 75s. The main difference between the two modelling approaches is the way the response delay is incorporated in the model. In the SDO approach, a number of GLM's containing a single sine regressor are fit to the data, each with a different delay value. The globally optimal delay value is selected as the one yielding the greatest number of significantly responsive voxels. Therefore, a CVR map is estimated, but only the globally optimal CVD is obtained. For the SCC, a single GLM is fit to the data containing two regressors (a sine and a cosine), from which both the amplitude and the delay of the response can be estimated in each voxel. In this case, we can obtain both CVD and CVR values voxelwise. Figure 2.8 summarizes some of the statistical analysis steps that were applied to the data and the difference between the two approaches. The general statistical analysis is first described and the specific modelling approaches implemented in this work are then presented in detail over the next sub-sections.

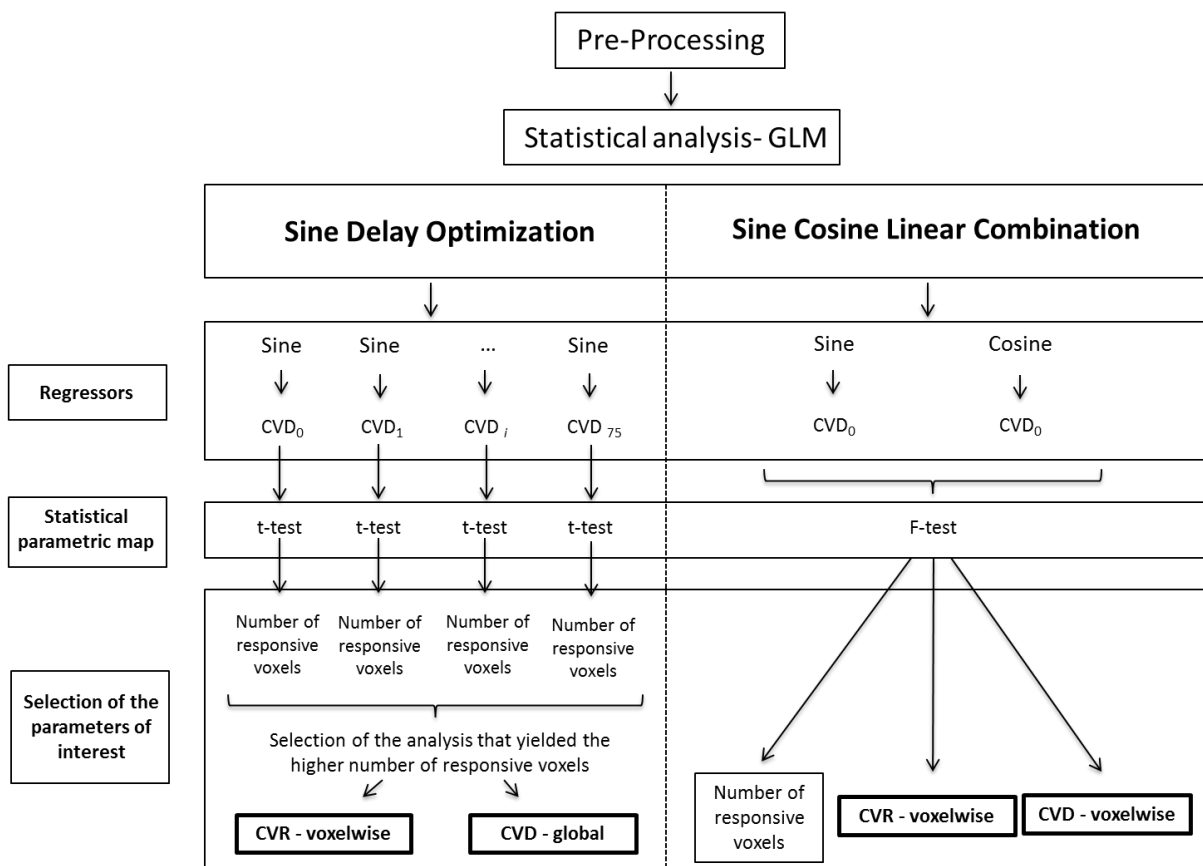


Figure 2.8: Comparison between the two GLM approaches and summary of the steps performed during statistical analysis.

After fitting the GLM to the data and obtaining parameter estimates, contrasts of interest are defined between parameter estimates and statistical tests are then employed in order to establish the significance of the contrasts in each voxel. Either t tests or F tests are performed in each voxel and

converted into maps of Z-statistics. Appropriate thresholding is then applied at a pre-defined significance level and the so-called statistical parametric maps (SPM's) are thus obtained. SPM's show which voxels or clusters of voxels are activated at a particular significance level.

For ASL data set “thresholding”, cluster thresholding was performed, with voxel $Z > 0.5$ and cluster $p < 0.05$. For the $BOLD_{ASL}$ data set, cluster thresholding was performed, with voxel $Z > 2.3$ and cluster $p < 0.05$.

We considered a greater cluster Z-threshold for the $BOLD_{ASL}$ data because of the higher sensitivity of this contrast. Moreover, after thresholding all contrasts, the SPM's of the interaction contrasts (perfusion) were additionally masked by voxels with positive perfusion baseline (from the control-tag regressor contrast).

2.2.2.1. Breath Hold Response Model

The BOLD and CBF responses to the BH protocols will be described in this work by a sinusoid. As it is mentioned before, the parameters chosen to characterize the BOLD, $BOLD_{ASL}$ and CBF responses to the respiratory challenge in terms of spatiotemporal dynamics are the CVR and the CVD. The CVR corresponds to the peak-to-peak amplitude of the response to the BH challenge, whereas the CVD corresponds to the time to peak of the response since the beginning of the BH task. These relations are depicted in Figure 2.9.

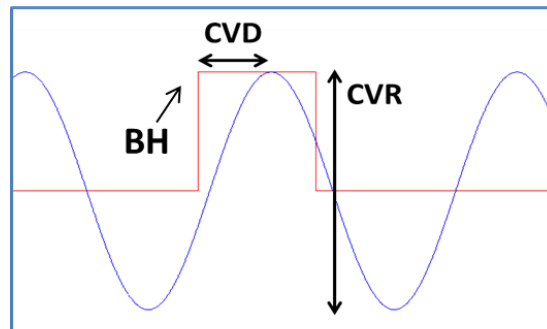


Figure 2.9: Relation between cerebrovascular delay (CVD), cerebrovascular reactivity (CVR) and breath-hold (BH) period. The sinusoid (blue) corresponds to the regressor used to model the response to BH and the red line corresponds to the BH period.

Both BOLD and ASL responses to the BH task were modelled using a sinusoid.

$$y(t) = a \sin (\omega t + \phi) \quad (2.1)$$

characterized by an amplitude, a , an angular frequency, ω (corresponding to the BH task period, $T = \frac{2\pi}{\omega}$) and a phase, ϕ .

Since our paradigm has an initial baseline period of T_0 before BH, the relationship between the sinusoid's phase (ϕ) and the response delay (CVD) (time to peak relative to the next sinusoid's maximum after the beginning of the BH) is given by:

$$CVD = \text{mod} \left(\frac{1}{4}T - T_0 - \phi, T \right) \quad (2.2)$$

where $\text{mod}(a, b)$ gives the remainder of the integer division between a and b .

2.2.2.2. Sine Delay Optimization

The Sine Delay Optimization (SDO) is a global approach, i.e., parameter estimation consists on finding one optimized global CVD value for the whole brain and an associated CVR map.

While doing a voxelwise analysis, Equation (2.1) can be written as

$$y_i(t) = a_i \sin(\omega t + \phi), \quad i = 1 \dots N \quad (2.3)$$

where the index i represents each voxel in the brain and N is the total number of voxels in the brain.

In this approach we consider a fixed sine phase/delay in each GLM analysis. Several analyses were made with different values of delay, ranging from 0 to 75s (the paradigm period) with 1s increments, in order to find the one that yielded the maximum number of significantly responsive voxels in the whole brain.

2.2.2.2.1. BOLD Signal Regressors

For the BOLD signal, only one paradigm-related (BOLD activation) regressor or explanatory variable (EV) was defined (EV1). This corresponds to 1 column in the matrix X in Equation (1.12), as shown in the design matrix (Figure 2.10). A sine wave with a period of 75s was used to model the BOLD response to the BH task. Several analyses with different values of delay (ranging from 0 to 75s) were made.

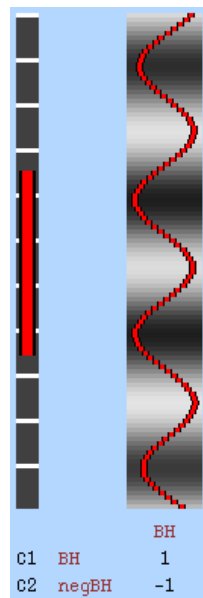


Figure 2.10: Design matrix for the BOLD data set analysis (time runs vertically) and corresponding contrasts. The left red rectangle corresponds to the temporal filtering cutoff of 100s applied to the data. The regressor used to model the data is represented on the right (sinusoid) and the corresponding 2 contrasts are represented on the bottom of the image.

Additionally, two contrasts were setup for EV1, one with a positive sign (C1, BH) and the other with a negative sign (C2, negBH).

2.2.2.2.2. ASL Signal Regressors

For the ASL protocol, there are two ways of analysing this type of data with FSL FEAT:

- Subtraction of control and tag time points, converting data into a perfusion-only signal;
- Full perfusion signal modelling.

It has been shown that the control-tag differencing approach suffers from a loss in efficiency and produces biased estimates of the standard errors so we chose to apply instead the full perfusion signal model approach [68].

For the full perfusion model three regressors were defined. These regressors correspond to 3 columns in the matrix X in Equation (1.12).

The first regressor (EV1) models the baseline control-tag alternating intensity variation. This represents the alternation between control and tag conditions when there isn't functional activation. This regressor was adjusted to start at the tag point of the data by changing its phase so as to yield a positive baseline value.

The second explanatory variable (EV2) models the intrinsic $BOLD_{ASL}$ signal present. It was used a sine wave with a period of 75s and delays ranging from 0 to 75s.

The final and third regressor (EV3) is the interaction between EV1 and EV2, and is formed by multiplying the control-tag and the paradigm-related BOLD explanatory variables together, and models the activation component of the control-tag signal. It is close to zero during rest and rises in amplitude when there is activation. This regressor corresponds to the perfusion signal.

The design matrix is depicted in Figure 2.11.

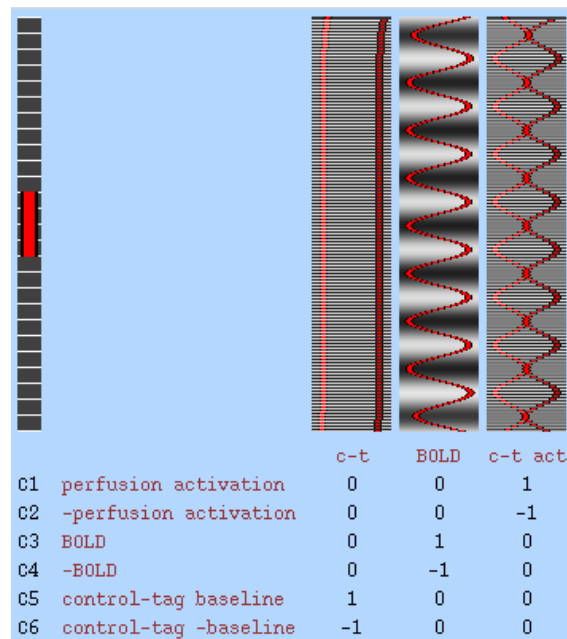


Figure 2.11: Design matrix for the ASL data set analysis (time runs vertically) and corresponding contrasts. The left red rectangle corresponds to the temporal filtering cutoff of 100s applied to the data. The three regressors used to model the data are represented on the right and the corresponding 6 contrasts are represented on the bottom of the image.

Two contrasts were set up for each of the EVs. C1 (perfusion activation), C3 (BOLD) and C5 (control-tag baseline) correspond to EV3, EV2, and EV1 with positive signs, respectively. C2 (-perfusion activation), C4 (-BOLD) and C6 (control-tag -baseline) correspond to the same EVs but with negative signs.

2.2.2.2.3. Calculation of CVR and CVD

In this approach, the two principal parameters to be estimated are the optimal CVD value and the corresponding CVR values/map.

CVR measurements were obtained as the percent signal changes (PSC) over time and using only the voxels inside the region of interest (ROI) obtained by statistical thresholding.

For the computation of the PSC values, the images of the COPEs of each contrast of interest (BOLD, BOLD_{ASL} and CBF) were imported to MATLAB to further calculations.

All PSC computations were done using Equation (2.4).

$$PSC (\%) = \frac{COPE \text{ of interest}}{COPE \text{ baseline}} \times 100 \quad (2.4)$$

In this approach, for the BOLD and BOLD_{ASL} contrasts, the COPE of interest corresponds to the sinusoid contrast that modelled the BOLD response to the BH task, COPE 1 in the BOLD analysis and COPE 3 in the ASL analysis. The baseline COPE for the BOLD contrasts corresponds to the pre-processed original signal, time averaged.

For the CBF contrast, the COPE of interest corresponds to the COPE related to interaction between the baseline perfusion signal and the BOLD_{ASL} signal, COPE1 in the ASL analysis. The baseline COPE to the CBF analysis corresponds to the contrast related to the baseline perfusion signal, COPE 5 in the ASL analysis.

So the CVR values were computed voxelwise (correspond to values a_i in Equation 2.5).

Relatively to the delay values, an optimal value of delay was obtained for the whole brain, as the one used in the analysis that yielded the maximum number of responsive voxels, so no further calculations were made in order to obtain this value.

2.2.2.2.4. Using Motion Parameters and Harmonics

A new analysis was performed with the addition of harmonics. The inclusion of these parameters was motivated by a study performed by Friman et al. [69].

Three harmonics were added to the fundamental frequency. However, the results obtained with the inclusion of harmonics, compared to the ones obtained not using them, were not significantly different. The values of the number of activated voxels with harmonics were of the same order of magnitude, with a slight dependence on the subject being analysed.

Another analysis was made but this time with the inclusion of motion parameters, from MCFLIRT. Again, the results obtained were not significantly different.

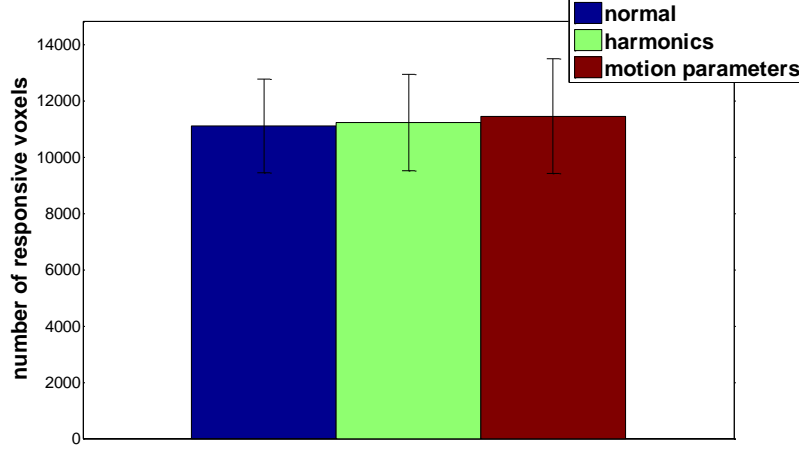


Figure 2.12: Mean number of responsive voxels of subjects obtained with a normal analysis and with analysis using harmonics and motion parameters as regressors. Error bars represent standard deviations of the mean.

Since the full model was easier to interpret without the motion parameters and harmonics, we decided not to add them to the model.

2.2.2.3. Sine Cosine Linear Combination

The Sine Cosine Linear Combination (SCC) is a voxel-by-voxel approach, i.e., the parameters to be estimated are a value of optimal delay for each voxel and the corresponding cerebrovascular reactivity amplitude, also for each voxel.

To obtain the delay of each voxel, a linear combination of two regressors, a sine and a cosine wave, was modelled.

The reason why we used these two regressors to model the BOLD response to the BH task is that any linear combination of a sine and a cosine with equal periods is equivalent to a single sine with the same period but with a phase shift and different amplitude.

Given any a_1 and a_2 , we can find A (amplitude) and ϕ (phase shift) such that

$$a_{1i} \sin(\omega t) + a_{2i} \cos(\omega t) = a_i \sin(\omega t + \phi_i) \quad (2.5)$$

Using the identity

$$\sin(\alpha + \beta) = \sin(\alpha) \cos(\beta) + \cos(\alpha) \sin(\beta) \quad (2.6)$$

Equation (2.5) is equivalent to

$$a_{1i} \sin(\omega t) + a_{2i} \cos(\omega t) = a_i \sin(\omega t) \cos(\phi_i) + a_i \cos(\omega t) \sin(\phi_i) \quad (2.7)$$

By setting equal the coefficients of $\cos(\omega t)$ and $\sin(\omega t)$ to a_1 and a_2 , respectively.

$$a_i \sin(\phi_i) = a_{2i} \quad (2.8)$$

$$a_i \cos(\phi_i) = a_{1i} \quad (2.9)$$

If $a_{2i} \neq 0$ we can find a_i and ϕ_i using

$$a_i = \sqrt{a_{1i}^2 + a_{2i}^2} \quad (2.10)$$

$$\phi_i = \arctan \frac{a_{2i}}{a_{1i}} + \begin{cases} 0 & \text{if } a_{1i} \geq 0 \\ \pi & \text{if } a_{1i} < 0 \end{cases} \quad (2.11)$$

The phase shift can be also calculated using the function `atan2` that is already implemented in MATLAB.

This way we can obtain a CVD and a CVR value for each voxel by doing just one GLM analysis.

2.2.2.3.1. BOLD Signal Regressors

For the $BOLD_{ASL}$ signal, two paradigm-related explanatory variables (EV1 and EV2) or regressors were defined to explain the BOLD response to the BH task, corresponding to 2 columns in the matrix X (Equation 1.12). EV1 is a sine wave with a period of 75 s and EV2 is a cosine wave with the same period. However, in order to use a cosine as a regressor in FEAT, we selected a sine wave but with a phase shift.

$$\cos(\theta) = \sin\left(\frac{\pi}{2} - \theta\right) \quad (2.12)$$

This way, EV2 is a sine wave with period of 75s and with a phase of 18,75s ($\pi/2 \times 75s$).

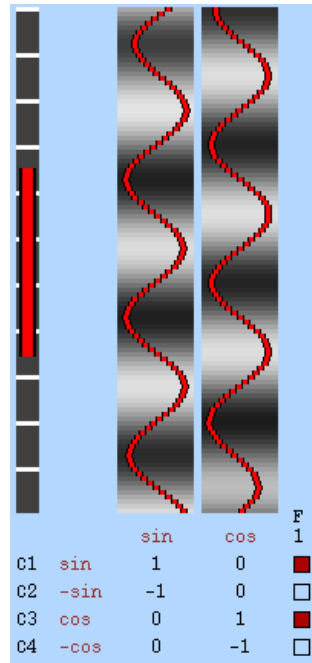


Figure 2.13: Design matrix for the BOLD data set analysis (time runs vertically) and corresponding contrasts. The left red rectangle corresponds to the temporal filtering cutoff of 100s applied to the data. The two regressors used to model the data are represented on the right and the corresponding 4 contrasts are represented on the bottom of the image. The red squares, on the right bottom of the image, define the contrasts that were combined for f-test.

Additionally two contrasts were setup for EV1 and EV2. C1 (sin) and C3 (cos) correspond to EV1 and EV2 with positive sign, respectively. C2 (-sin) and C4 (-cos) correspond to the same explanatory variables but the opposite sign.

One additional f-test was done for the $BOLD_{ASL}$ signal, combining the positive contrasts, C1 (sin) and C3 (cos).

2.2.2.3.2. ASL Signal Regressors

For the same reasons that were mentioned before in Section 2.2.2.2.2 , for the ASL protocol we decided to use the full perfusion signal modelling.

A total of five regressors were defined. These regressors correspond to 5 columns in the matrix X of Equation (1.12). One explanatory variable models the baseline control-tag alternating intensity variation (EV1). Again, this regressor was adjusted to start at the tag point of the data by changing its phase so as to yield a positive baseline value. The second explanatory variable (EV2) models with a sine wave the $BOLD_{ASL}$ signal present with a period of 75s and a phase of 0s. The third explanatory variable (EV3) models also the $BOLD_{ASL}$ signal present but with a cosine wave (period 75s, phase 18.75s). The fourth and fifth explanatory variables are formed by multiplying the control-tag and the respective paradigm-related $BOLD_{ASL}$ explanatory variables together (cosine or sine wave), and model the activation component of the control-tag signal (EV4 and EV5).

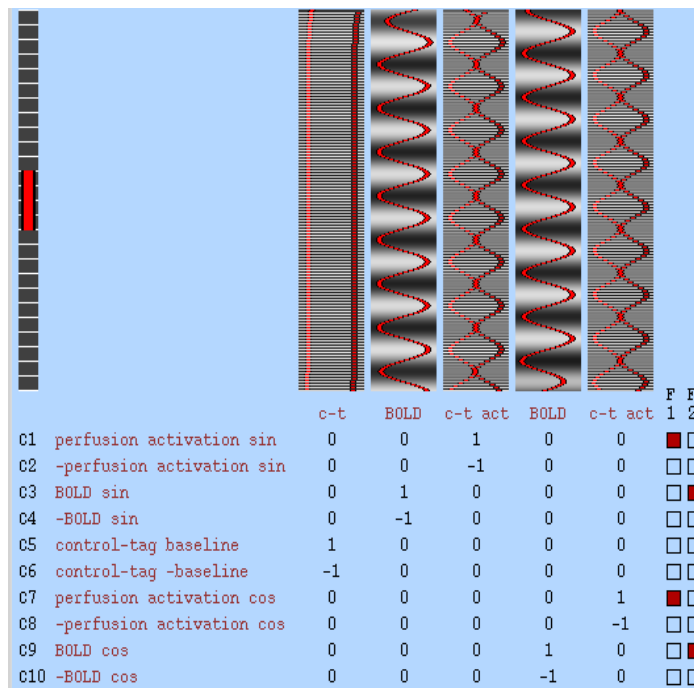


Figure 2.14. Design matrix for the ASL data set analysis(time runs vertically) and corresponding contrasts. The left red rectangle corresponds to the temporal filtering cutoff of 100s applied to the data. The 5 regressors used to model the data are represented on the right and the corresponding 10 contrasts are represented on the bottom of the image. The red squares, on the right bottom of the image, define the contrasts that were combined for f-tests.

Two contrasts were set up for each of the EV's. C1 (perfusion activation sin), C3 (BOLD sin), C5 (control-tag baseline), C7 (perfusion activation cos) and C9 (BOLD cos) correspond to EV3, EV2, EV1, EV5 and EV4 with positive signs, respectively. C2 (-perfusion activation sin), C4 (-BOLD sin), C6

(control-tag -baseline), C8 (-perfusion activation cos) and C10 (-BOLD cos) correspond to EV3, EV2, EV1, EV5 and EV4 with negative signs, respectively.

Additionally, two f-tests were made. The first was a combination of the sine (C3) and the cosine (C9) contrasts for the BOLD_{ASL} signal. The second was a combination of both perfusion activation contrasts (C1 and C7) for the CBF signal.

2.2.2.3.3. Calculation of CVR and CVD

In this approach the two principal parameters to be estimated are the cerebrovascular reactivity and cerebrovascular optimal delay maps.

The main difference between the two GLM approaches is the way the CVR and CVD values are obtained. Particularly for the CVD assessment, in the SDO approach, the value of delay was fixed, and by doing so, an optimal delay was found for the whole brain. In the SCC approach, the use of two regressors to model the response to BH, allows the delay not to be fixed, meaning that there is more flexibility in the sense that each voxel can have a specific delay.

For the CVR measurements, just like in the SDO approach, these values were obtained as percent signal changes (PSC) over time and using only the voxels inside the region of interest (ROI) obtained in the post-statistical analysis.

$$PSC (\%) = \frac{COPE \text{ of interest}}{COPE \text{ baseline}} \times 100 \quad (2.13)$$

For the computation of the PSC values, the images of the COPEs of each contrast of interest (BOLD, BOLD_{ASL} and CBF) were imported to MATLAB to further calculations.

For the calculation of the COPE of interest using the SCC approach, it was used a relation obtained in Equation (2.10) which relates the amplitude with sine and cosine coefficients. In this case the amplitude correspond to the values of PSC and the sine and cosine coefficients correspond to the COPE's values obtained with the GLM analysis using the sine and cosine regressors, respectively.

For the BOLD and BOLD_{ASL} contrasts, the final COPE of interest corresponded to the root mean of the sum of squares of the COPEs of interest, the COPE related with the sine function contrast and the COPE related with the cosine function. In short, the values of the COPE of interest were obtained using the Equation (2.14). This was done in a voxel-by-voxel manner.

$$COPE \text{ of interest} = \sqrt{(COPE \text{ sine})^2 + (COPE \text{ cosine})^2} \quad (2.14)$$

The baseline COPE corresponded to the pre-processed signal.

For the CBF contrast, the final COPE of interest is

$$COPE \text{ of interest} = \sqrt{(COPE \text{ interaction sine})^2 + (COPE \text{ interaction cosine})^2} \quad (2.15)$$

Where COPE interaction sine corresponded to the COPE related with activation component of the control-tag signal using a sine wave to model the BOLD signal and COPE interaction cosine corresponded to the COPE related with activation component of the control-tag signal but using a

cosine wave to model the BOLD signal. The baseline COPE corresponded to the contrast related to the baseline perfusion signal, COPE 5 in the design matrix.

Relatively to the delay values, it was used a relation obtained in Equation (2.11) which relates the delay with sine and cosine coefficients. Again, the sine and cosine coefficients correspond to the COPE's values obtained with the GLM analysis using the sine and cosine regressors. By using Equation (2.16) or Equation (2.17) a phase value is obtained for each voxel.

In the BOLD and BOLD_{ASL} contrasts case the relation between the COPEs and the delays is:

$$CVD = \text{atan2} \left(\frac{COPE \text{ cosine}}{COPE \text{ sine}} \right) \quad (2.16)$$

In the case of CBF contrast:

$$CVD = \text{atan2} \left(\frac{COPE \text{ interaction cosine}}{COPE \text{ interaction sine}} \right) \quad (2.17)$$

After the computation of the values of CVD for each voxel we need to convert them to delays using the Equation (2.2). Note that by doing so, some voxels may exhibit negative delay values. Nevertheless, due to the periodicity of the signal, we can convert these negative values to the correct ones by adding 2π to the negative values. This way delay values range from 0s to 75s.

2.2.3. Time Courses

Time courses of the corresponding region of interest that showed the desired activation were obtained for each type of data and each type of BH protocol.

ASL pre-processed data underwent surround subtraction in order to obtain the CBF-weighted time course (Equation (2.18)).

$$\left[P_1, P_2, \dots, P_{\frac{n}{2}} \right] = \left[C_2 - \frac{L_1 + L_2}{2}, C_3 - \frac{L_2 + L_3}{2}, \dots, C_{\frac{n}{2}} - \frac{L_{\frac{n}{2}-1} + L_{\frac{n}{2}}}{2} \right] \quad (2.18)$$

To obtain the BOLD_{ASL} time series a surround average was computed, consisting of the average of each image with the average of its two nearest neighbours (Equation (2.19)).

$$\left[B_1, B_2, \dots, B_{\frac{n}{2}} \right] = \left[\frac{\left(\frac{C_1 + L_1}{2} + \frac{L_1 + C_2}{2} \right)}{2}, \frac{\left(\frac{L_1 + C_2}{2} + \frac{C_2 + L_2}{2} \right)}{2}, \dots \right] \quad (2.19)$$

Then a spatial mean was computed for each subject, across the respective ROI of significantly responsive voxels, followed by a temporal mean across all breath-hold periods in the task. Each time course begins with the breath-hold period (20s).

3

Results

In this chapter the results obtained using the materials and methods described in the previous chapter are presented. It is organized as it follows: in the first two sections the partial pressure of end-tidal carbon dioxide and the head motion values are presented. In Section 3.3 the comparison between the two GLM analysis methods is described (Sine Delay Optimization and Sine Cosine Linear Combination). This comparison was done using only the BH protocol without preparatory inspiration dataset and the criteria used to compare the approaches were the spatial measurements (number of responsive voxels, CVD and CVR) and the corresponding subjects' CVR and CVD maps. Section 3.4 compares the two breath-hold protocols (with and without preparatory inspiration). Only the results from the Sine Cosine Linear Combination modelling approach were used for this comparison. Again the criteria used were the spatial measurements and the group CVD and CVR maps. Furthermore, the time courses of signals derived from both BH protocols were presented.

3.1. Partial Pressure of End Tidal Carbon Dioxide

The end-tidal CO₂ pressure (P_{ET}CO₂) was monitored throughout the experiment using a capnograph. However, this data were only acquired in three subjects (R5, R6 and R7). The values of P_{ET}CO₂ change after BH, obtained during the different types of acquisitions, are represented in Table 3.1 and in Figure 3.1. The results show that the values of P_{ET}CO₂ increased after BH, as expected. Moreover, the P_{ET}CO₂ changes observed in the experiment with preparatory inspiration were significantly higher than those without the preparatory inspiration.

Generally, the CVR values are obtained as percent signal change per mm Hg change in P_{ET}CO₂. However, due to the fact that we only acquired values of P_{ET}CO₂ for three subjects, the CVR measures in this paper are presented as the percent signal change of the signal relative to its baseline (Equations 2.4 and 2.13).

Table 3.1: P_{ET}CO₂ values in mmHg acquired during the two BH challenges, without preparatory inspiration (left) and with preparatory inspiration (right).

P _{ET} CO ₂ (mmHg)	Without Preparatory Inspiration			With Preparatory Inspiration		
Subjects	BOLD	ASL	mean	BOLD	ASL	mean
R5	7.30	10.40	8.85	19.70	9.10	14.40
R6	2.30	7.60	4.95	8.00	7.10	7.55
R7	6.00	8.75	7.37	11.00	14.50	12.75
mean ± standard deviation	5 ± 3	9 ± 1	7 ± 2	13 ± 6	12 ± 4	12 ± 4

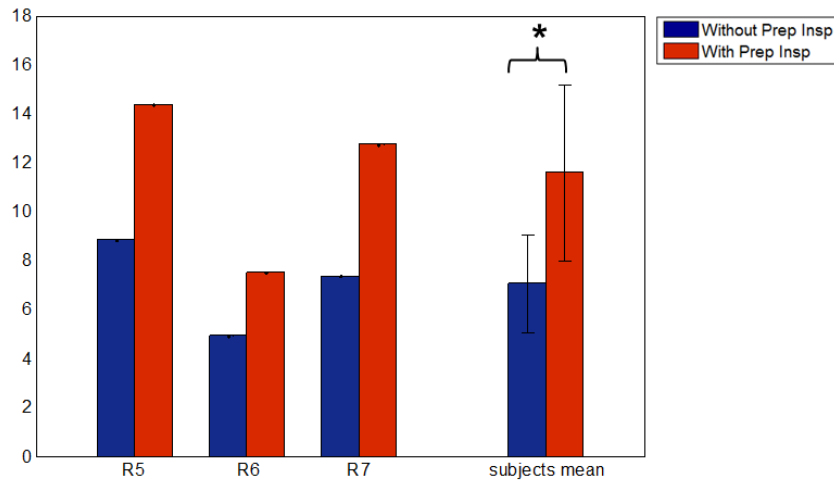


Figure 3.1: Bar charts of the $P_{ET}CO_2$ values during the two BH challenges (with and without preparatory inspiration) for each subject (left) and for the subjects mean (right). Error bars represent standard deviations of the mean and * represents significant differences ($p < 0.05$).

3.2. Head Motion – Subject Exclusion

The re-alignment of the fMRI volume time series yields head motion parameters values, which can be used to compute mean head displacements over time. These values are shown in Table 3.2 for each subject, acquisition type and protocol type.

An exclusion threshold was applied in order to exclude the subjects who have a value of absolute head motion greater than 0.25mm ($\delta > 0.25$ mm). Subject R1 in the BH protocol with preparatory inspiration BOLD analysis and subject R3 in the BH protocol with preparatory inspiration ASL analysis showed values of head movement greater than the threshold. Further analyses using the Inspiration datasets were done without these subjects.

Table 3.2: Mean head motion in mm during acquisitions for each type of sequence and BH protocol.

Head motion (mm)	Without Preparatory Inspiration		With Preparatory Inspiration	
	BOLD	ASL	BOLD	ASL
R1	0.13	0.12	0.38	0.18
R2	0.14	0.13	0.12	0.2
R3	0.14	0.23	0.21	0.29
R4	0.16	0.12	0.14	0.09
R5	0.09	0.1	0.15	0.18
R6	0.12	0.2	0.1	0.16
R7	0.09	0.13	0.16	0.2

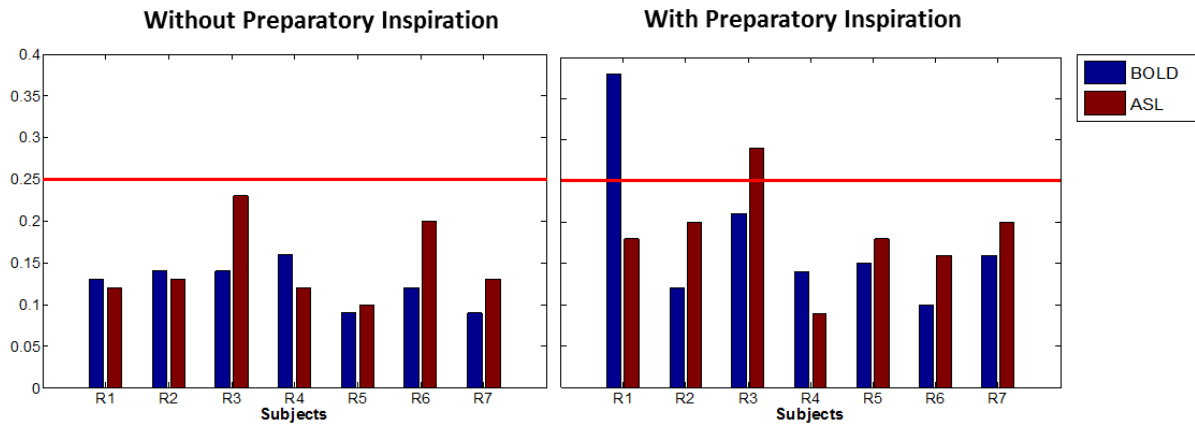


Figure 3.2: Bar charts of mean head displacement in mm during BH challenge without preparatory inspiration (left) and with preparatory inspiration (right) for the two sequences. The red horizontal line corresponds to a threshold (0.25 mm).

3.3. Analysis Method Comparison

In this section the two GLM analysis approaches (Sine Delay Optimization and Sine Cosine Linear Combination) are going to be compared. Only the results obtained using the BH protocol without preparatory inspiration dataset will be used for this purpose.

3.3.1. Spatial Measurements

The comparison will be performed in terms of spatial measurements of each subject: number of responsive voxels, mean CVR values and optimal/most representative CVD values.

3.3.1.1. Number of Responsive Voxels

The number of responsive voxels obtained using the two modelling approaches (SDO and SCC) are presented in Table 3.3, Figure 3.3 and Figure 3.4, for the three contrasts considered, BOLD, BOLD_{ASL} and CBF.

Table 3.3: Number of responsive voxels for each subject using the two modelling approaches (SDO and SCC), for each of the contrasts considered (BOLD, BOLD_{ASL} and CBF).

Number of responsive voxels	Sine Delay Optimization			Sine Cosine Linear Combination		
	Subjects	BOLD	BOLD _{ASL}	CBF	BOLD	BOLD _{ASL}
R1	10603	9320	4233	10455	10007	3759
R2	10743	11856	5244	11912	12425	6054
R3	9020	6714	4604	9544	7998	6159
R4	14168	11039	4049	13995	11467	3101
R5	9949	10239	4466	11648	10703	3837
R6	11018	9783	4669	11847	10346	3808
R7	12210	10952	4887	13777	12244	5331
mean ± standard deviation	$(11 \pm 2) \times 10^3$	$(10 \pm 2) \times 10^3$	$(4 \pm 0.4) \times 10^3$	$(12 \pm 2) \times 10^3$	$(11 \pm 2) \times 10^3$	$(5 \pm 0.1) \times 10^3$

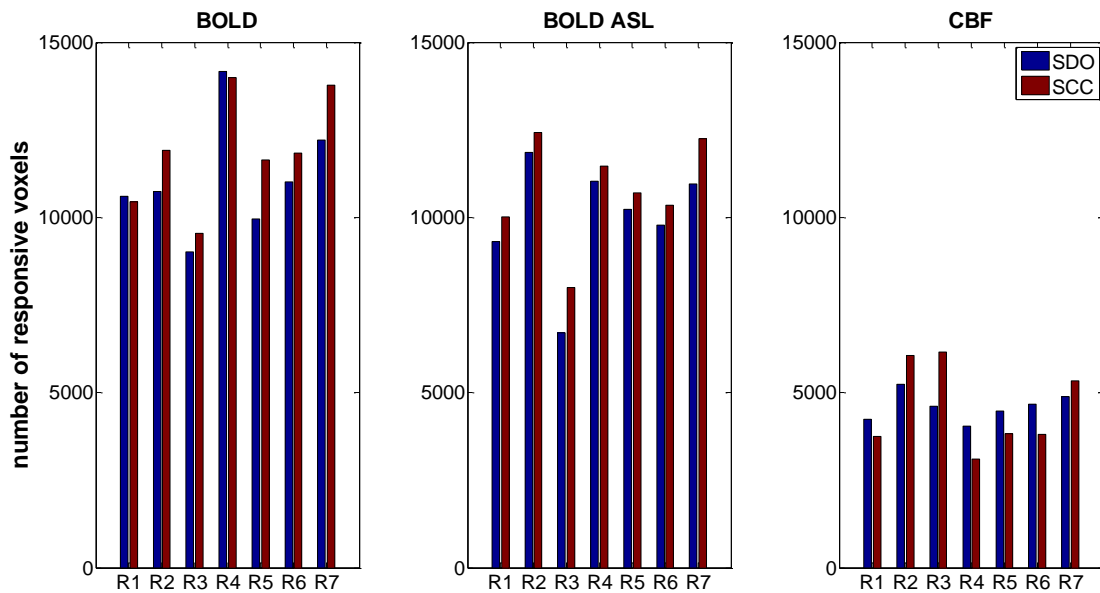


Figure 3.3: Bar chart of number of responsive voxels for each subject using the two modelling approaches (SDO and SCC), for each of the contrasts considered (BOLD, BOLD_{ASL} and CBF).

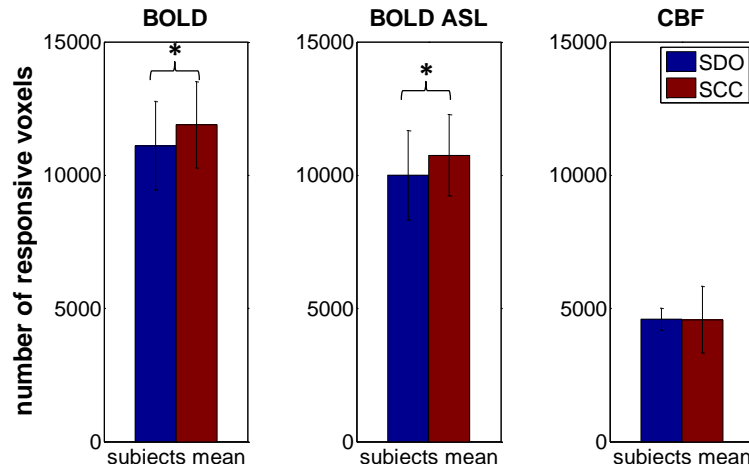


Figure 3.4: Bar chart of number of responsive voxels of the mean of all subjects using the two modelling approaches (SDO and SCC), for each of the contrasts considered (BOLD, BOLD_{ASL} and CBF). Error bars represent standard deviations of the mean and * represents significant differences ($p < 0.005$).

The BOLD and BOLD_{ASL} number of responsive voxels are much higher than the CBF number of responsive voxels in both approaches. This is at least partly due to the much lower SNR of the CBF data. Most interestingly, the results show that the SCC method significantly improves the sensitivity of both BOLD and BOLD_{ASL} responses to the BH paradigm relative to the SDO method (Figure 3.4). However, no significant improvements are found for CBF data.

3.3.1.2. Cerebrovascular Delay Values

The most representative CVD values obtained using the two modelling approaches, for each contrast considered (BOLD, BOLD_{ASL} and CBF) are presented in Table 3.4, Figure 3.5 and Figure 3.6. For the SDO approach, the optimal CVD values were obtained as the ones that yielded the maximum number of responsive voxels for each subject. For the SCC approach, the most representative CVD values were chosen as the ones yielding the maximum of the histogram across all responsive voxels, i.e., the value of delay that appears more often in the brain of each subject.

Table 3.4: Global delay values in seconds for each subject using the two modelling approaches (SDO and SCC), for each of the contrasts considered (BOLD, BOLD_{ASL} and CBF).

CVD (s)	Sine Delay Optimization			Sine Cosine Linear Combination		
	BOLD	BOLD _{ASL}	CBF	BOLD	BOLD _{ASL}	CBF
Subjects						
R1	21.25	16.25	68.25	19.00	14.00	58.00
R2	34.25	34.25	35.25	32.00	30.00	29.00
R3	22.25	22.25	33.25	21.00	20.00	26.00
R4	33.25	32.25	74.25	31.00	29.00	46.00
R5	24.25	26.25	38.25	20.00	22.00	50.00
R6	34.25	40.25	23.25	31.00	34.00	16.00
R7	29.25	29.25	37.25	29.00	29.00	27.00
mean ± standard deviation	28 ± 6	29 ± 8	44 ± 19	26 ± 6	25 ± 7	36 ± 15

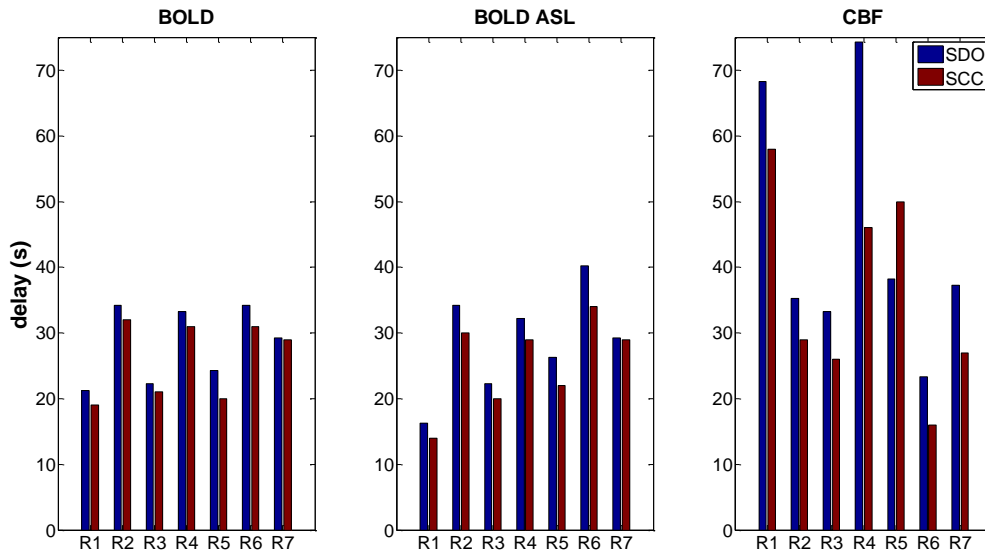


Figure 3.5: Bar chart of global CVD values for each subject using the two modelling approaches (SDO and SCC) approaches, for each of the contrasts considered (BOLD, BOLD_{ASL} and CBF).

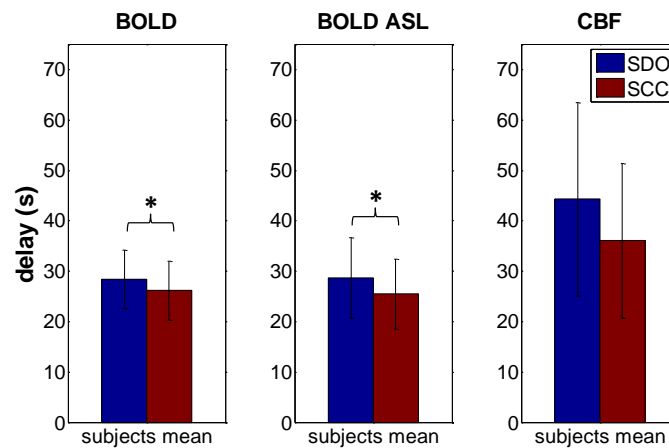


Figure 3.6: Bar chart of the mean CVD values of all subjects using the SDO approach and the SCC approach. Error bars represent standard deviations of the mean and * represents significant differences ($p < 0.005$).

Significant differences were found for the CVD values of BOLD and BOLD_{ASL} responses between the two approaches, with the SCC approach having, on average, lower values of delay. No significant differences were found for the CBF data.

Bar charts and histograms of the number of responsive voxels for each type of approach and for each subject will be presented, in Figure 3.7 to Figure 3.20. The SDO approach results are depicted on the left bar charts whereas the SCC approach results are depicted on the right histograms. The BOLD_{ASL} results are presented firstly and then the CBF results are presented. The red line corresponds to the global delay values estimated for each type of GLM approaches. The SDO charts show the number of responsive voxels (y axis) obtained for each GLM analysis with a specific delay (x axis). The SCC chart shows the histogram of the values of delay for the whole brain.

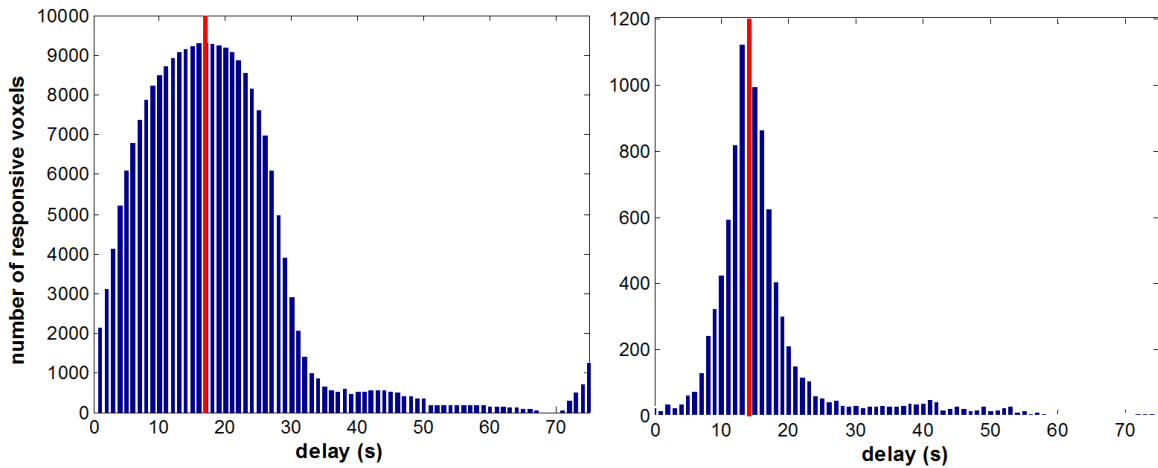


Figure 3.7: Bar chart (SDO approach, left) and histogram (SCC approach, right) of the number of responsive voxels of the $BOLD_{ASL}$ data of subject R1. The red vertical lines represent the optimal (SDO approach, left) or the most representative (SCC approach, right) delay.

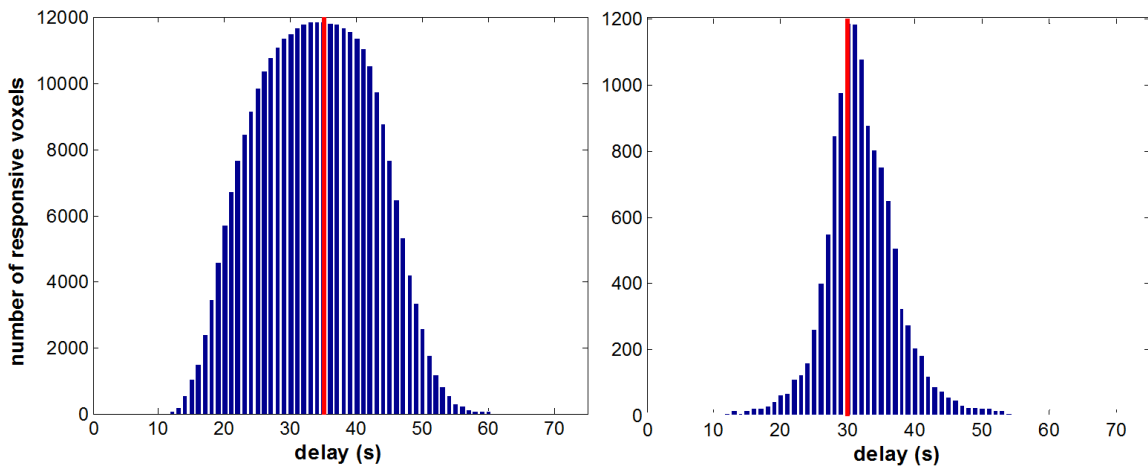


Figure 3.8: Bar chart (SDO approach, left) and histogram (SCC approach, right) of the number of responsive voxels of the $BOLD_{ASL}$ data of subject R2. The red vertical lines represent the optimal (SDO approach, left) or the most representative (SCC approach, right) delay.

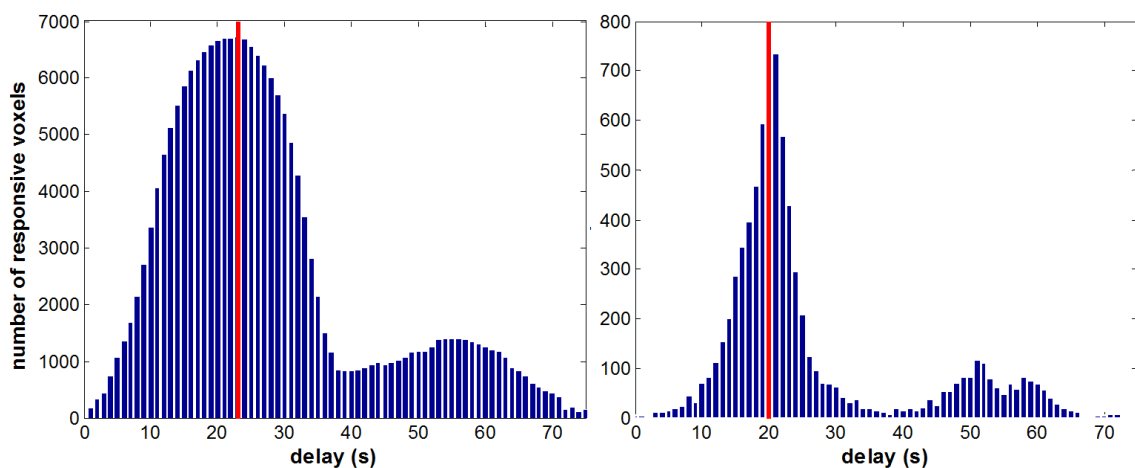


Figure 3.9: Bar chart (SDO approach, left) and histogram (SCC approach, right) of the number of responsive voxels of the $BOLD_{ASL}$ data of subject R3. The red vertical lines represent the optimal (SDO approach, left) or the most representative (SCC approach, right) delay.

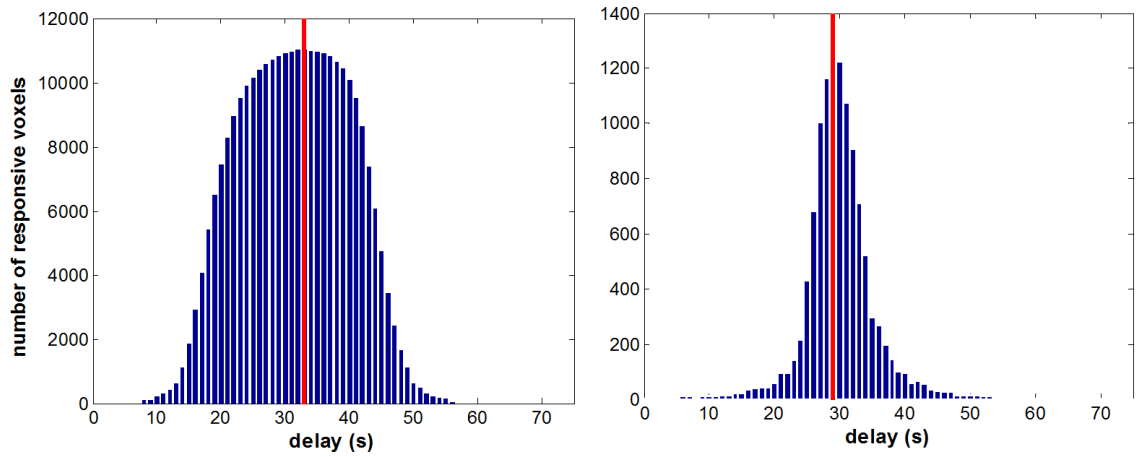


Figure 3.10: Bar chart (SDO approach, left) and histogram (SCC approach, right) of the number of responsive voxels of the $BOLD_{ASL}$ data of subject R4. The red vertical lines represent the optimal (SDO approach, left) or the most representative (SCC approach, right) delay.

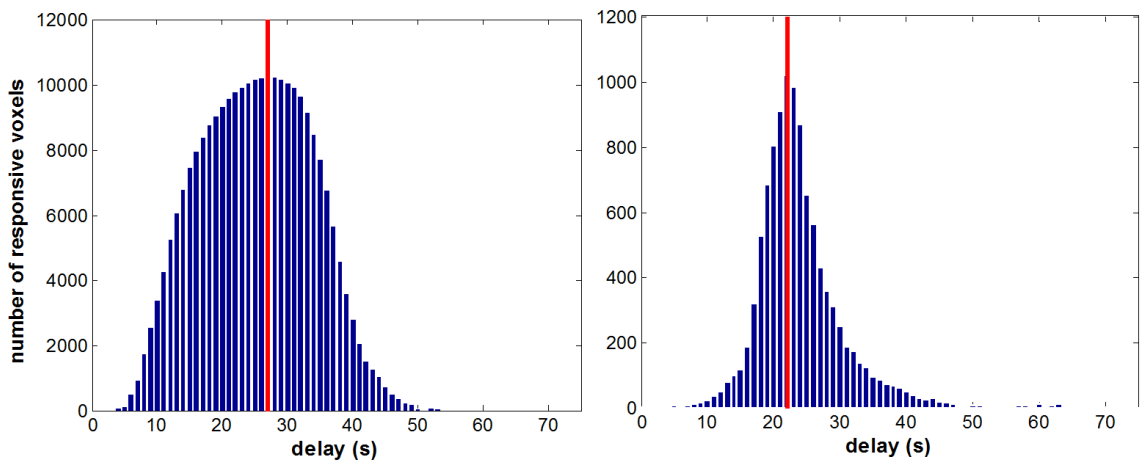


Figure 3.11: Bar chart (SDO approach, left) and histogram (SCC approach, right) of the number of responsive voxels of the $BOLD_{ASL}$ data of subject R5. The red vertical lines represent the optimal (SDO approach, left) or the most representative (SCC approach, right) delay.

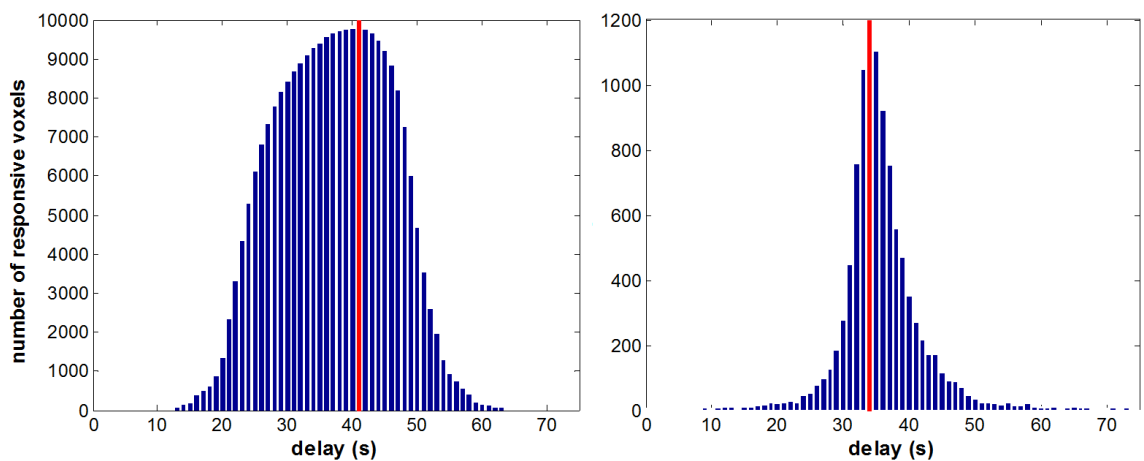


Figure 3.12: Bar chart (SDO approach, left) and histogram (SCC approach, right) of the number of responsive voxels of the $BOLD_{ASL}$ data of subject R6. The red vertical lines represent the optimal (SDO approach, left) or the most representative (SCC approach, right) delay.

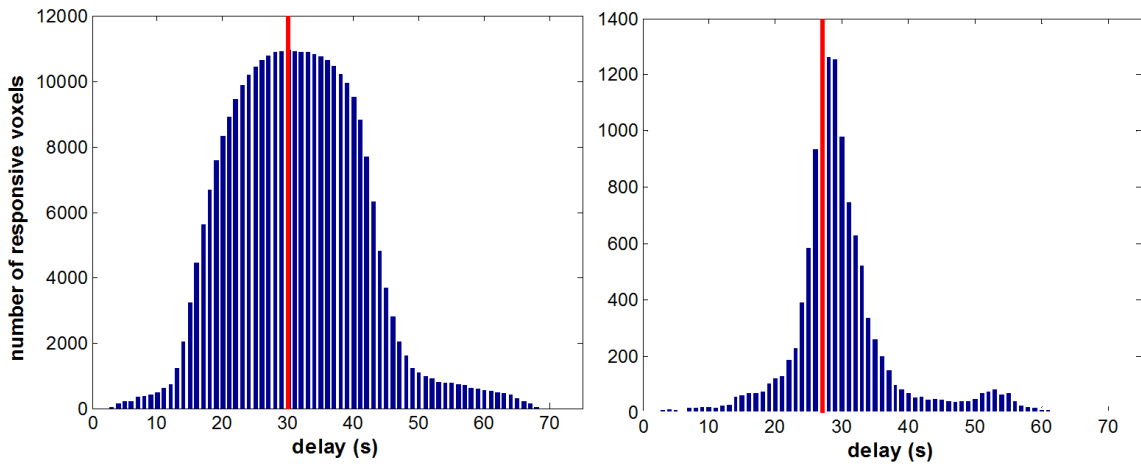


Figure 3.13: Bar chart (SDO approach, left) and histogram (SCC approach, right) of the number of responsive voxels of the $BOLD_{ASL}$ data of subject R7. The red vertical lines represent the optimal (SDO approach, left) or the most representative (SCC approach, right) delay.

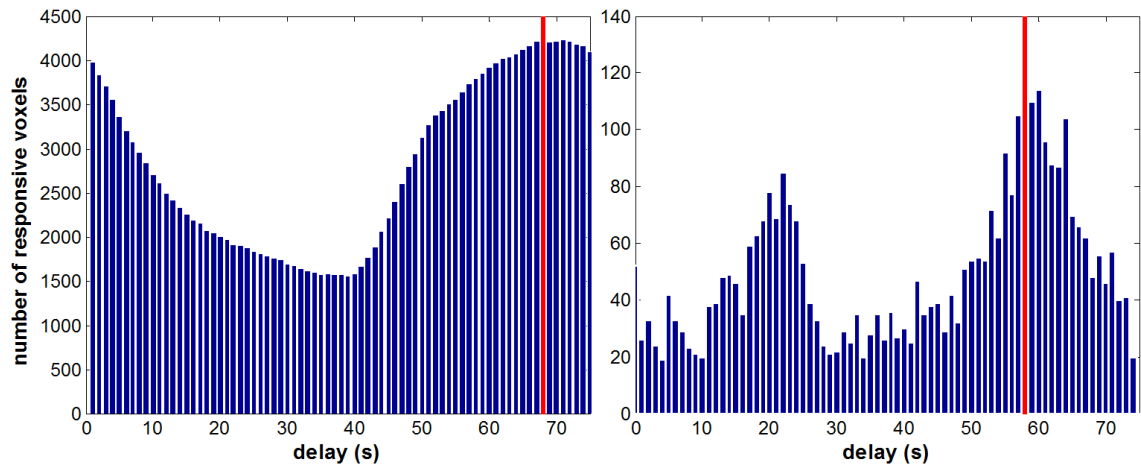


Figure 3.14: Bar chart (SDO approach, left) and histogram (SCC approach, right) of the number of responsive voxels of the CBF data of subject R1. The red vertical lines represent the optimal (SDO approach, left) or the most representative (SCC approach, right) delay.

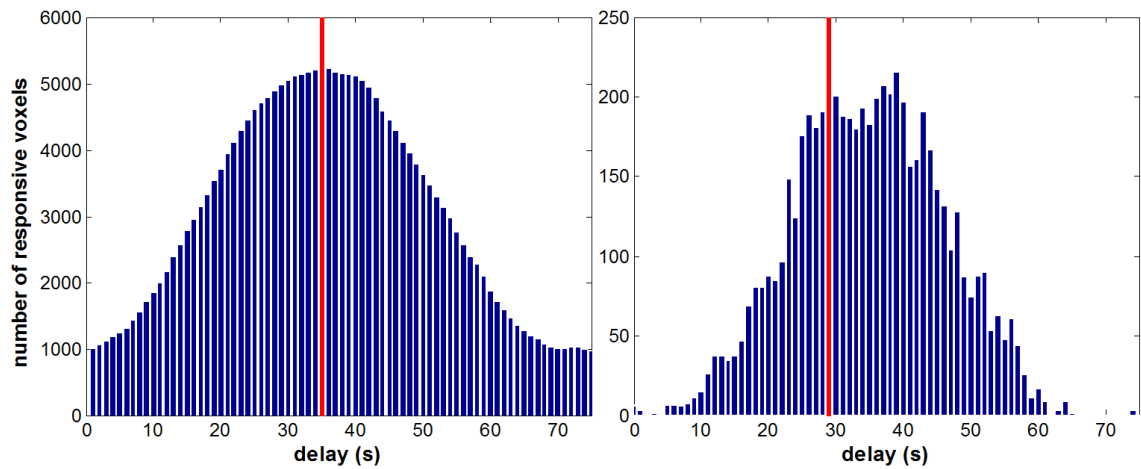


Figure 3.15: Bar chart (SDO approach, left) and histogram (SCC approach, right) of the number of responsive voxels of the CBF data of subject R2. The red vertical lines represent the optimal (SDO approach, left) or the most representative (SCC approach, right) delay.

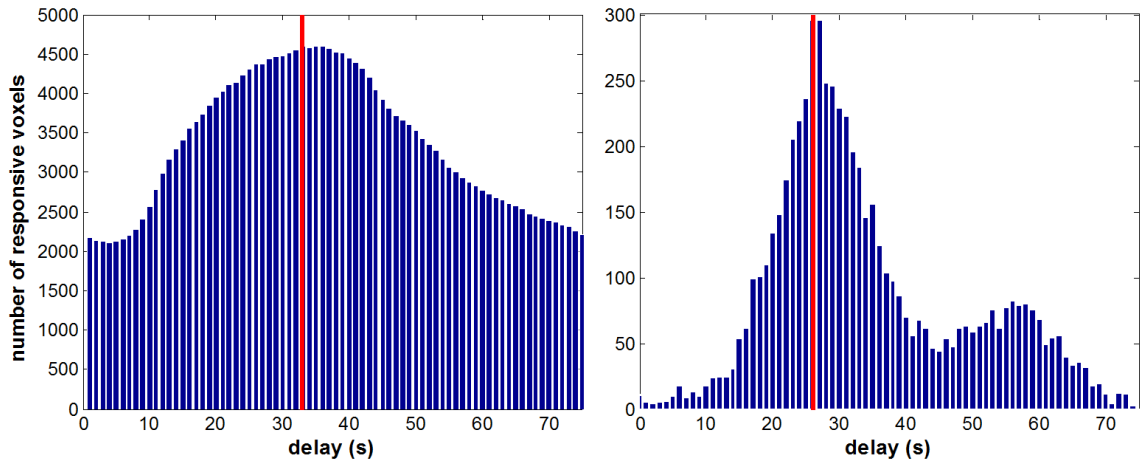


Figure 3.16: Bar chart (SDO approach, left) and histogram (SCC approach, right) of the number of responsive voxels of the CBF data of subject R3. The red vertical lines represent the optimal (SDO approach, left) or the most representative (SCC approach, right) delay.

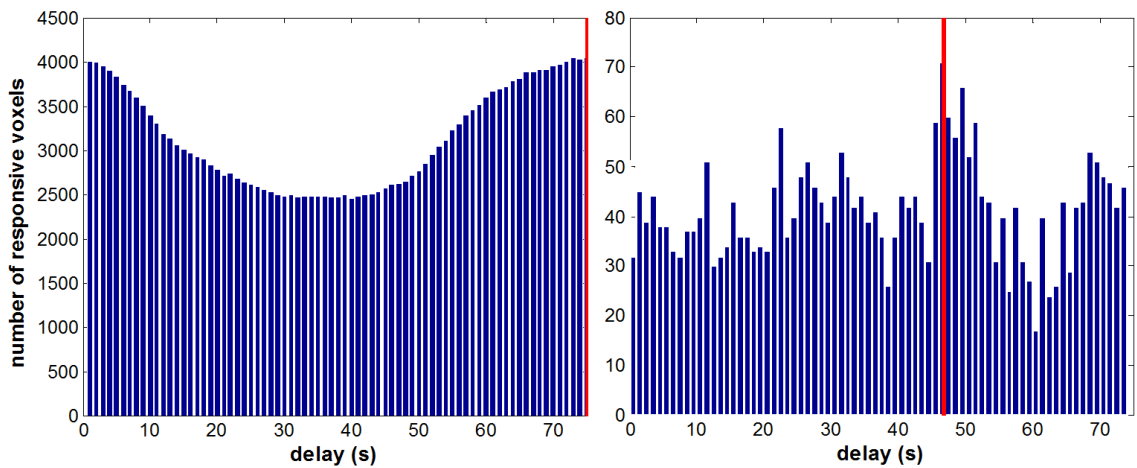


Figure 3.17: Bar chart (SDO approach, left) and histogram (SCC approach, right) of the number of responsive voxels of the CBF data of subject R4. The red vertical lines represent the optimal (SDO approach, left) or the most representative (SCC approach, right) delay.

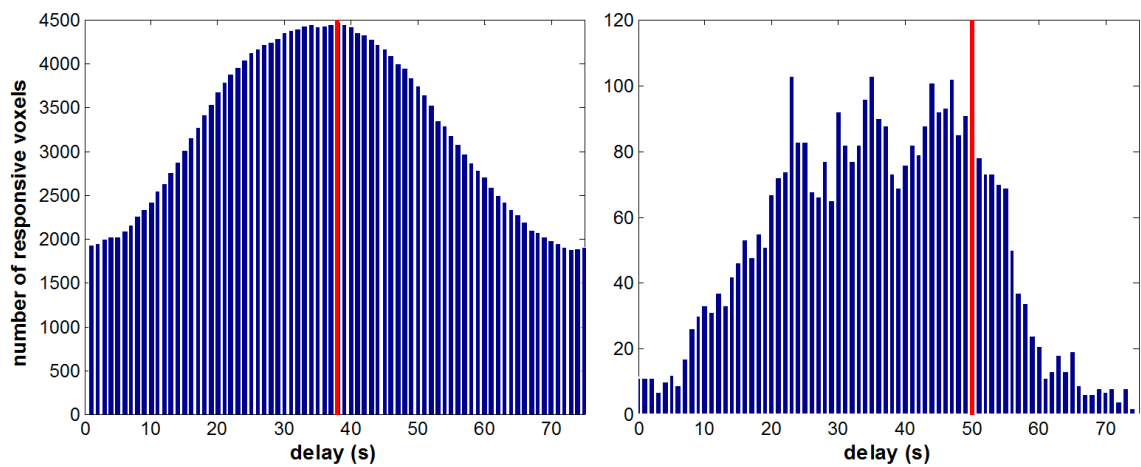


Figure 3.18: Bar chart (SDO approach, left) and histogram (SCC approach, right) of the number of responsive voxels of the CBF data of subject R5. The red vertical lines represent the optimal (SDO approach, left) or the most representative (SCC approach, right) delay.

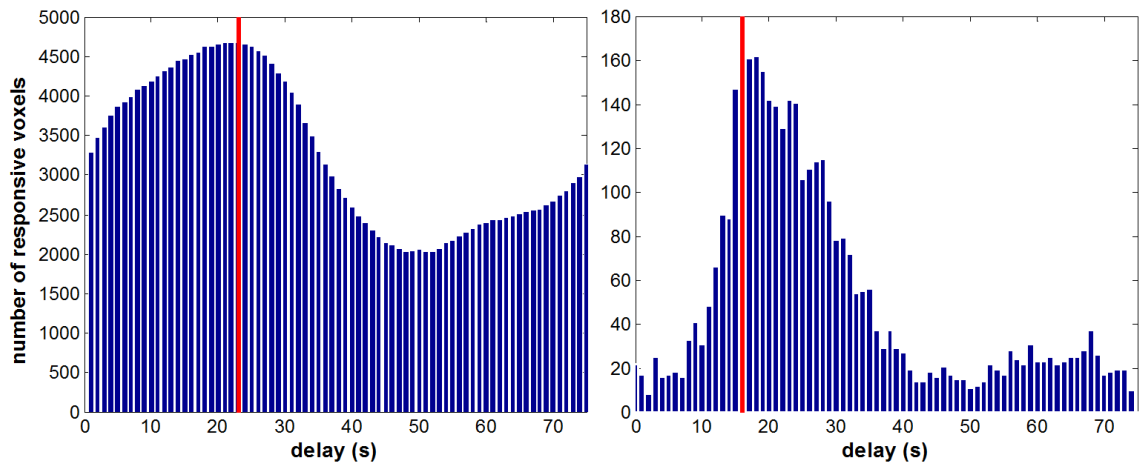


Figure 3.19: Bar chart (SDO approach, left) and histogram (SCC approach, right) of the number of responsive voxels of the CBF data of subject R6. The red vertical lines represent the optimal (SDO approach, left) or the most representative (SCC approach, right) delay.

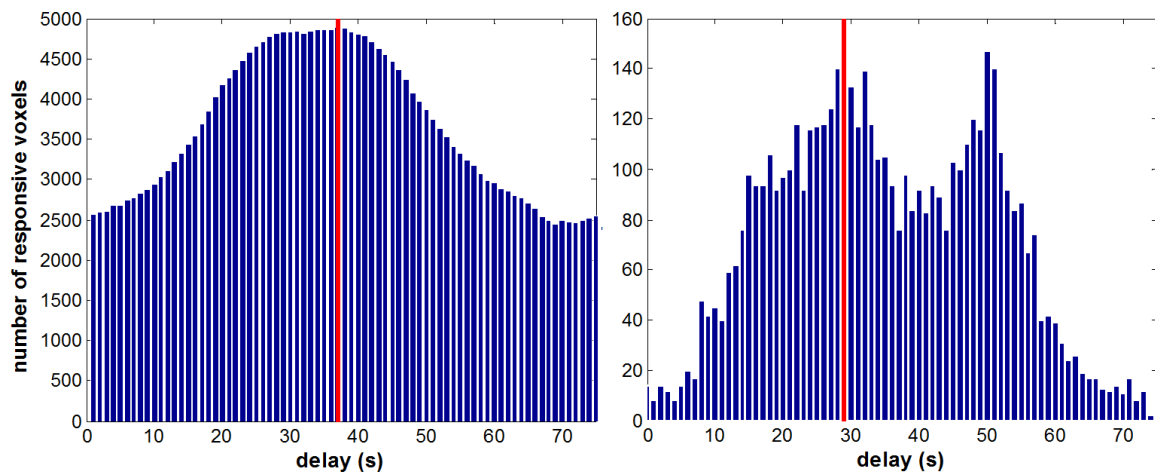


Figure 3.20: Bar chart (SDO approach, left) and histogram (SCC approach, right) of the number of responsive voxels of the CBF data of subject R7. The red vertical lines represent the optimal (SDO approach, left) or the most representative (SCC approach, right) delay.

The $BOLD_{ASL}$ results tend to show a well-defined shape and peak, both for the SDO and SCC methods. In contrast, the values of CBF delay varied much more across the brain in both approaches.

3.3.1.3. Cerebrovascular Reactivity Values

The CVR values obtained by both modelling approaches, for each of the three contrasts considered (BOLD, $BOLD_{ASL}$ and CBF), are presented in Table 3.5, Figure 3.21 and Figure 3.22.

Table 3.5: CVR values in percent signal change for each subject using the two modelling approaches (SDO and SCC), for each of the contrasts considered (BOLD, BOLD_{ASL} and CBF).

CVR (%)	Sine Delay Optimization			Sine Cosine Linear Combination		
Subjects	BOLD	BOLD _{ASL}	CBF	BOLD	BOLD _{ASL}	CBF
R1	2.55	0.88	103.60	2.82	0.98	127.70
R2	2.63	1.06	117.50	2.96	1.13	89.30
R3	2.56	0.93	97.70	2.93	1.05	92.00
R4	2.80	0.92	79.20	3.00	0.97	115.40
R5	2.16	0.72	69.50	2.41	0.78	76.10
R6	1.87	0.61	72.20	2.05	0.68	81.50
R7	2.25	0.64	68.70	2.35	0.78	88.40
mean ± standard deviation	2.4 ± 0.3	0.8 ± 0.2	87 ± 19	2.7 ± 0.4	0.9 ± 0.2	96±19

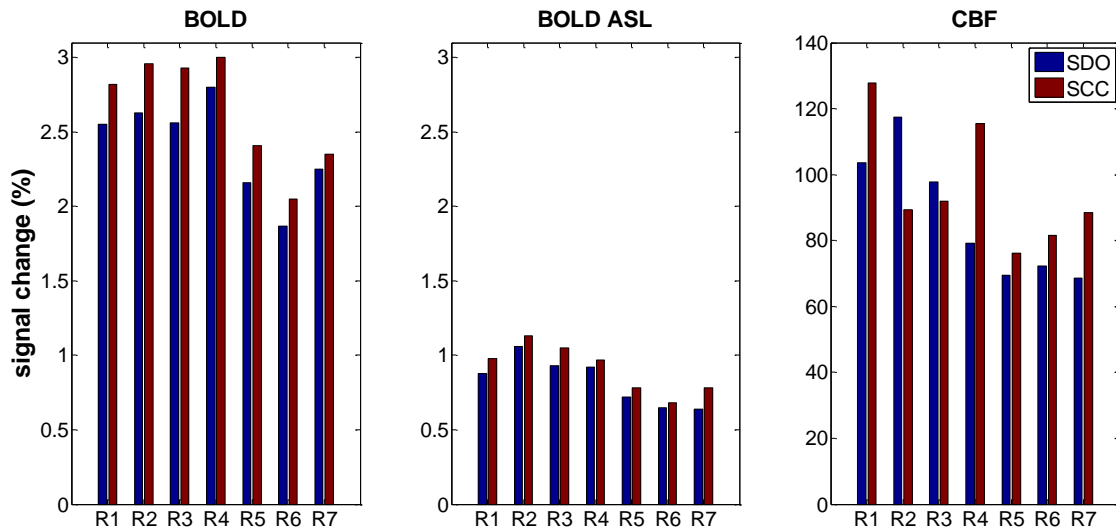


Figure 3.21: Bar chart of global CVR values for each subject using the two modelling approaches (SDO and SCC) approaches, for each of the contrasts considered (BOLD, BOLD_{ASL} and CBF).

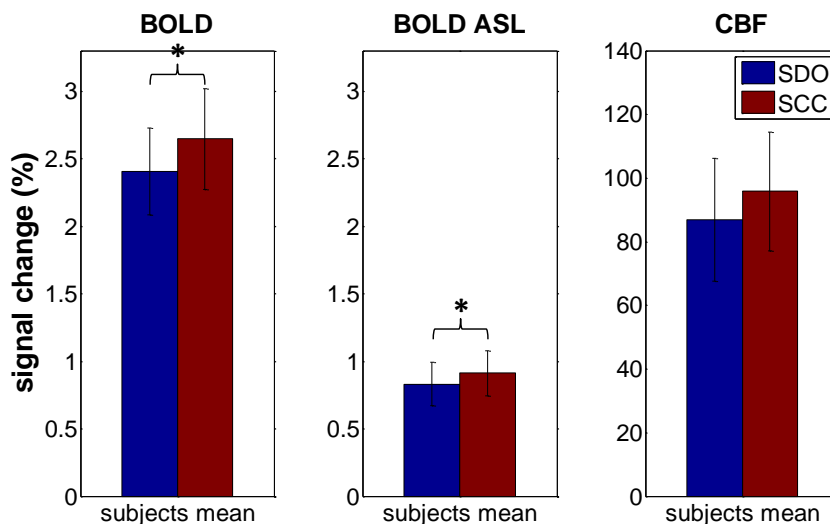


Figure 3.22: Bar chart of the mean CVR values of all subjects using the SDO approach and the SCC approach. Error bars represent standard deviations of the mean and * represents significant differences ($p < 0.005$).

The CVR percent signal change values are according with the ones reported in the literature, even though these values are not normalized by $P_{ET}CO_2$. As expected, CVR values for CBF are much higher than BOLD or $BOLD_{ASL}$ values. $BOLD_{ASL}$ reactivity values are smaller than BOLD, due to the lower sensitivity of the former as a consequence of the fact that a non-optimal BOLD acquisition sequence was used in the ASL experiment. As it was described in the Methods chapter, the ASL acquisition sequence was optimized for the CBF signal, and thus, the $BOLD_{ASL}$ signal obtained does not have as higher PSC as the optimized BOLD signal alone.

Significant differences between the CVR values of the two approaches were found for the BOLD and $BOLD_{ASL}$ data, with the SCC approach having, on average, higher CVR values. However, CBF data didn't show significant differences. Correlation between the CVR and $P_{ET}CO_2$ was also computed. The results are shown in Table 3.6.

Table 3.6: Correlation between CVR values and $P_{ET}CO_2$.

	BOLD	$BOLD_{ASL}$	CBF
correlation p-value	0.1459	0.2453	0.7994

No correlation was observed between the values of $P_{ET}CO_2$ and the CVR values for each subject. However these results were obtained using data of only three subjects due to reasons that were enumerated in Section 3.1.

3.3.2. Cerebrovascular Reactivity and Delay Maps

The individual CVD and CVR maps obtained using the two approaches are going to be presented in the next section.

3.3.2.1. Individual Maps

Maps of CVR and CVD were obtained using the methods described in Sections 2.2.2.2 and 2.2.2.3.

Further thresholding was applied to the CVR and CVD maps for better visualization. Regarding the $BOLD_{ASL}$ results, only the voxels with reactivity values below 2.5% are presented in the CVR and CVD maps. For the CBF maps, the same strategy was defined, but in this case the CVR threshold is voxels with CVR values below 200%.

A more complex threshold was applied using the CVD values. For each subject's analysis, the maximum number of responsive voxels and the corresponding delay were computed. Then using a cycle beginning at 0s and with increments of 1s and another cycle beginning at 75s and with increments of -1s, the first values of delay that yield a number of responsive voxels above 5% of the maximum (first threshold) are found, creating two new thresholds, one for lower values of delay and one for higher values. After finding these two thresholds, only the delays above the first threshold and below the second threshold are represented in the maps. This CVD mask was also applied to the CVR maps. This way, CVD and CVR maps have the same masks, i.e., are shown for the same voxels in each subject.

All nine slices of the resulting maps are represented in Figure 3.23, Figure 3.24, Figure 3.25, Figure 3.26, Figure 3.27, Figure 3.28 and Figure 3.29. The maps obtained using the SDO approach are depicted on the top row and the maps obtained using the SCC approach are represented on the two bottom rows. For the former approach, SDO, only the CVR maps are represented since the CVD measure was obtained as a global optimal delay for the whole brain. For the SCC approach, both the CVR and CVD maps are depicted in the figures, since both parameters were estimated in a voxelwise manner.

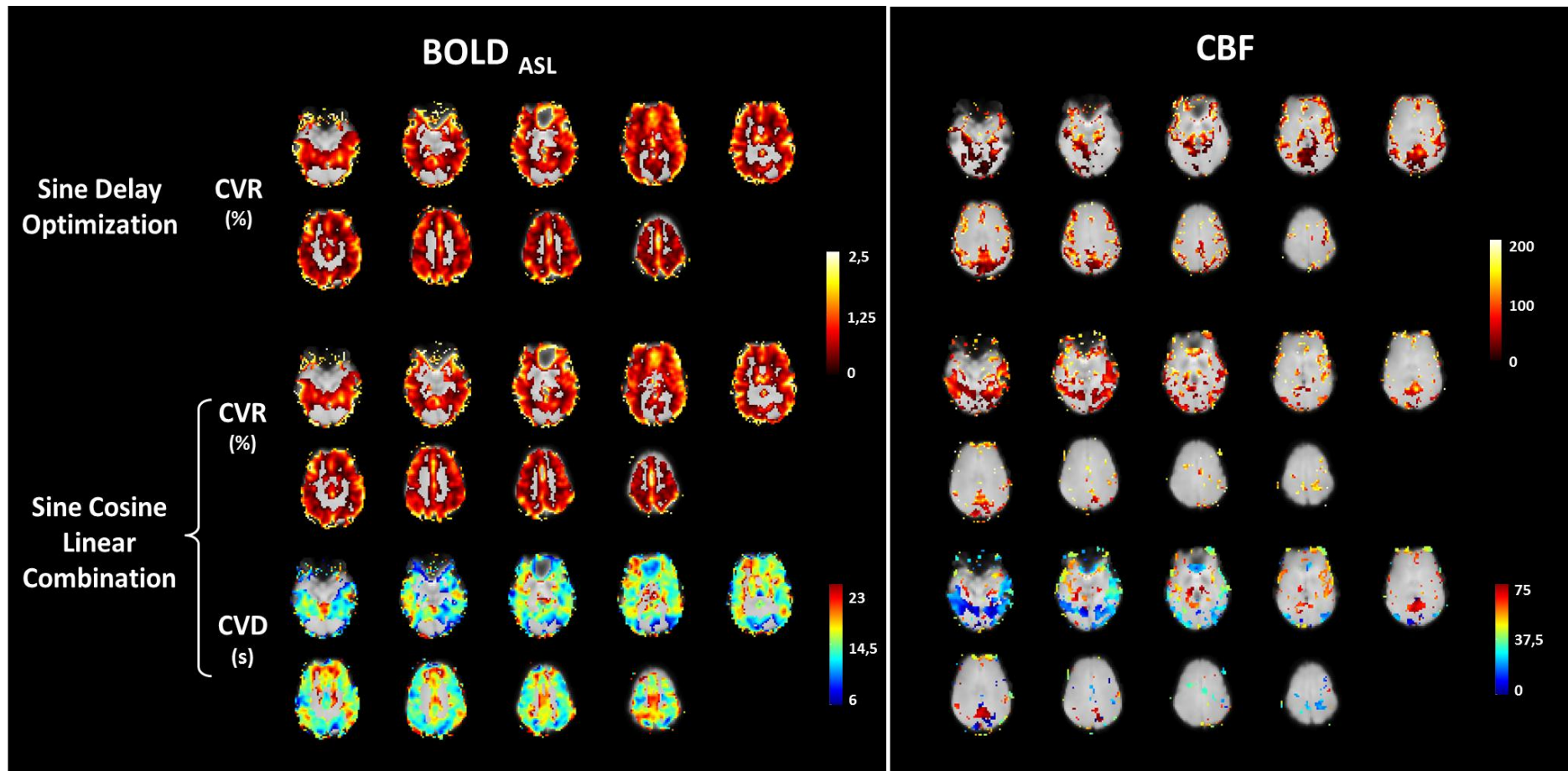


Figure 3.23: CVR and CVD maps obtained for subject R1, using the two modelling approaches (SDO and SCC) and for the two ASL contrasts, BOLD_{ASL} and CBF. For the SDO approach only the CVR maps (top rows) are presented since the value of delay obtained is global (not voxel-by-voxel). For the SCC approach both CVR (third and fourth rows) and CVD maps (last two rows) are presented. The CVR values are in percentage and the CVD values are in seconds.

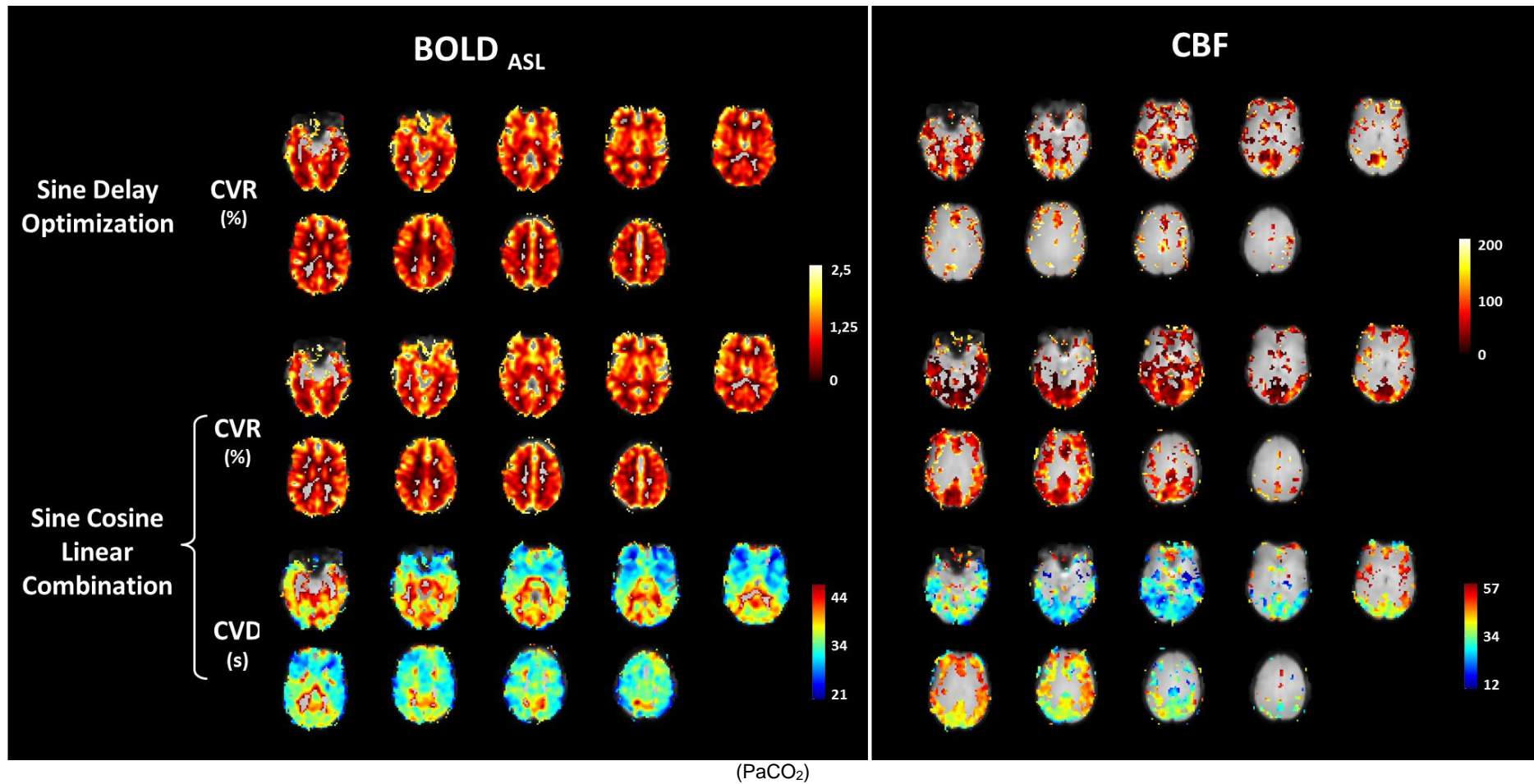


Figure 3.24: CVR and CVD maps obtained for subject R2, using the two modelling approaches (SDO and SCC) and for the two ASL contrasts, $BOLD_{ASL}$ and CBF. For the SDO approach only the CVR maps (top rows) are presented since the value of delay obtained is global (not voxel-by-voxel). For the SCC approach both CVR (third and fourth rows) and CVD maps (last two rows) are presented. The CVR values are in percentage and the CVD values are in seconds.

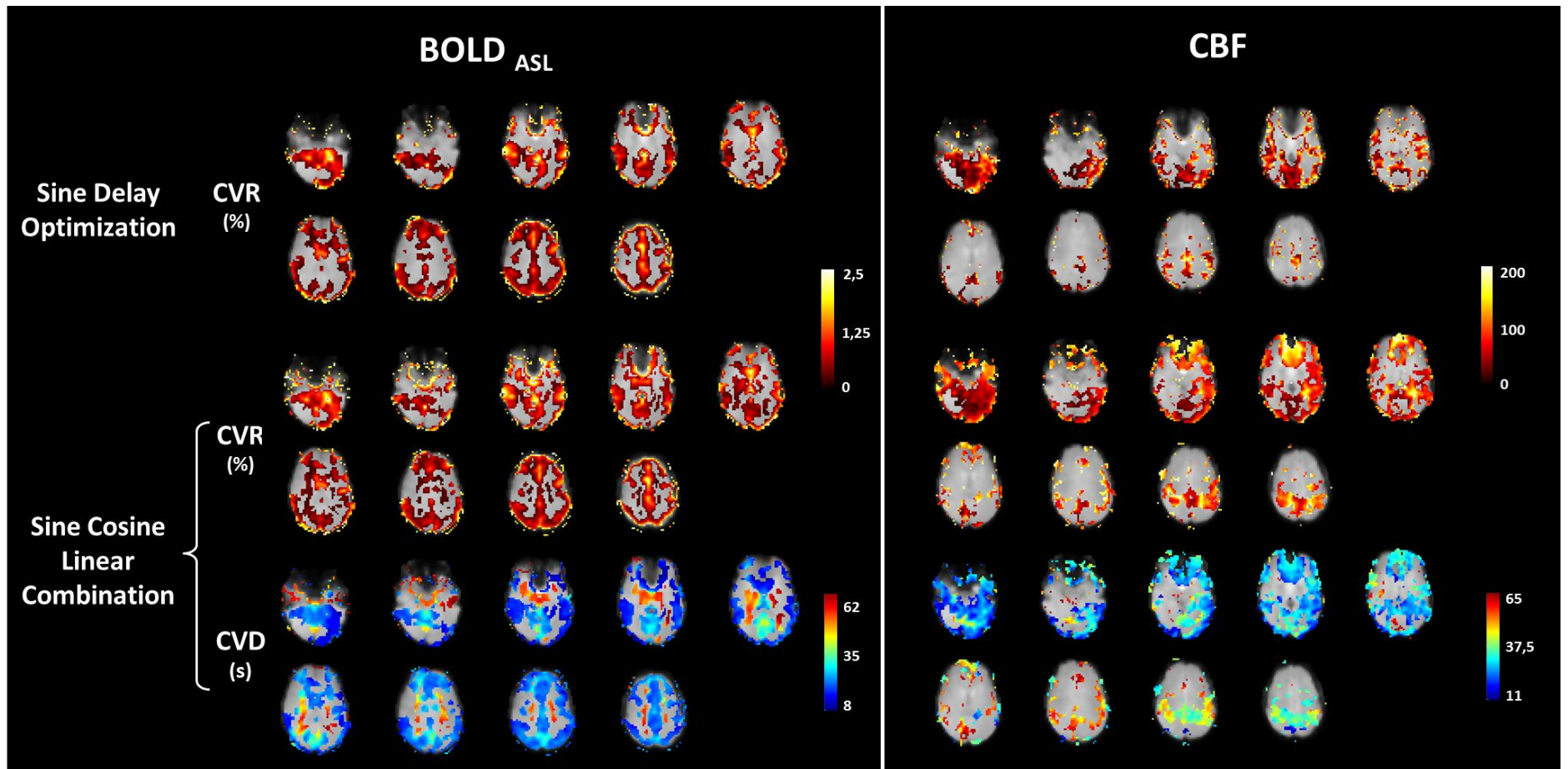


Figure 3.25: CVR and CVD maps obtained for subject R3, using the two modelling approaches (SDO and SCC) and for the two ASL contrasts, $BOLD_{ASL}$ and CBF. For the SDO approach only the CVR maps (top rows) are presented since the value of delay obtained is global (not voxel-by-voxel). For the SCC approach both CVR (third and fourth rows) and CVD maps (last two rows) are presented. The CVR values are in percentage and the CVD values are in seconds.

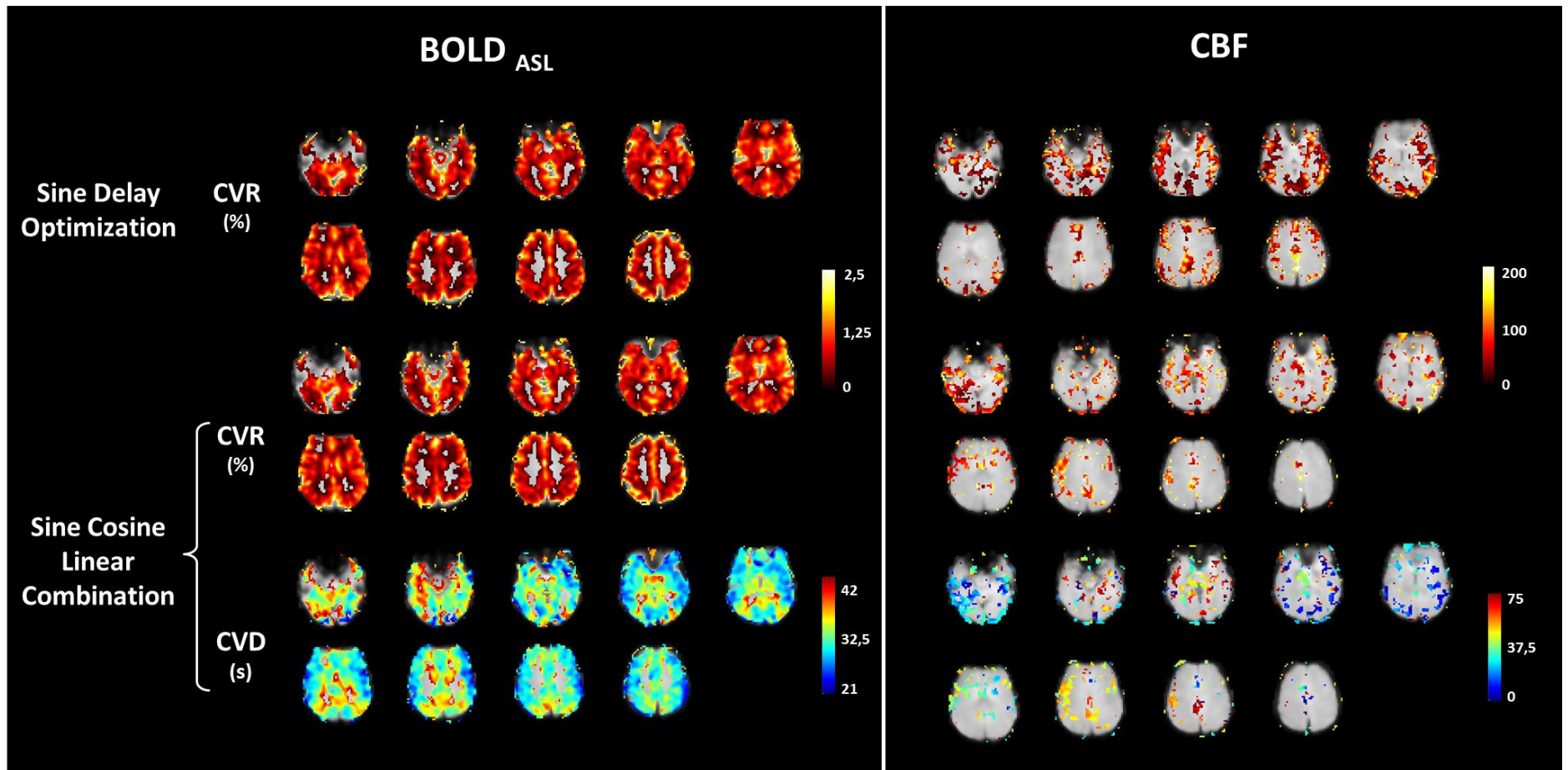


Figure 3.26. CVR and CVD maps obtained for subject R4, using the two modelling approaches (SDO and SCC) and for the two ASL contrasts, BOLD_{ASL} and CBF. For the SDO approach only the CVR maps (top rows) are presented since the value of delay obtained is global (not voxel-by-voxel). For the SCC approach both CVR (third and fourth rows) and CVD maps (last two rows) are presented. The CVR values are in percentage and the CVD values are in seconds.

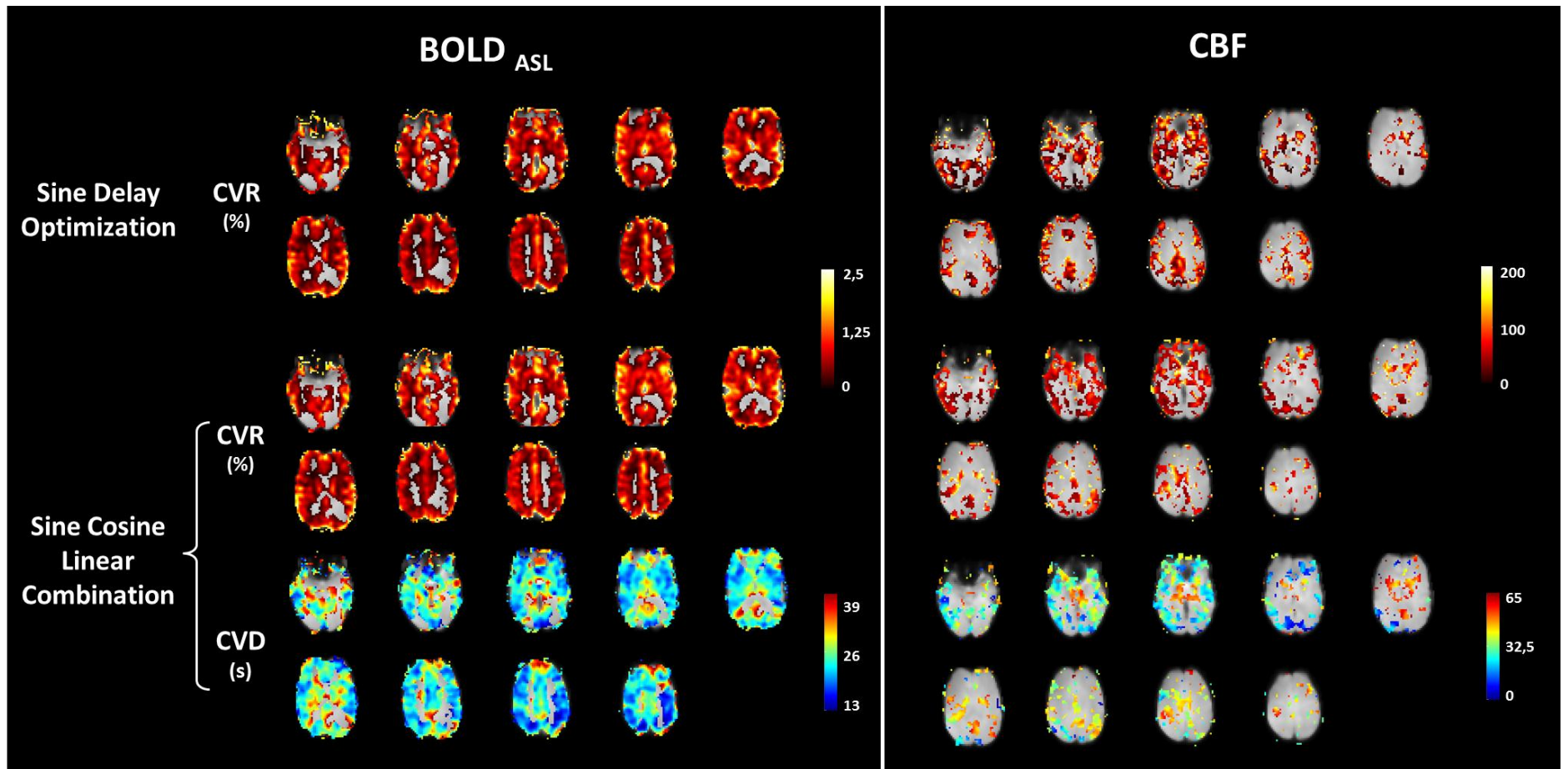


Figure 3.27: CVR and CVD maps obtained for subject R5, using the two modelling approaches (SDO and SCC) and for the two ASL contrasts, BOLD_{ASL} and CBF. For the SDO approach only the CVR maps (top rows) are presented since the value of delay obtained is global (not voxel-by-voxel). For the SCC approach both CVR (third and fourth rows) and CVD maps (last two rows) are presented. The CVR values are in percentage and the CVD values are in seconds.

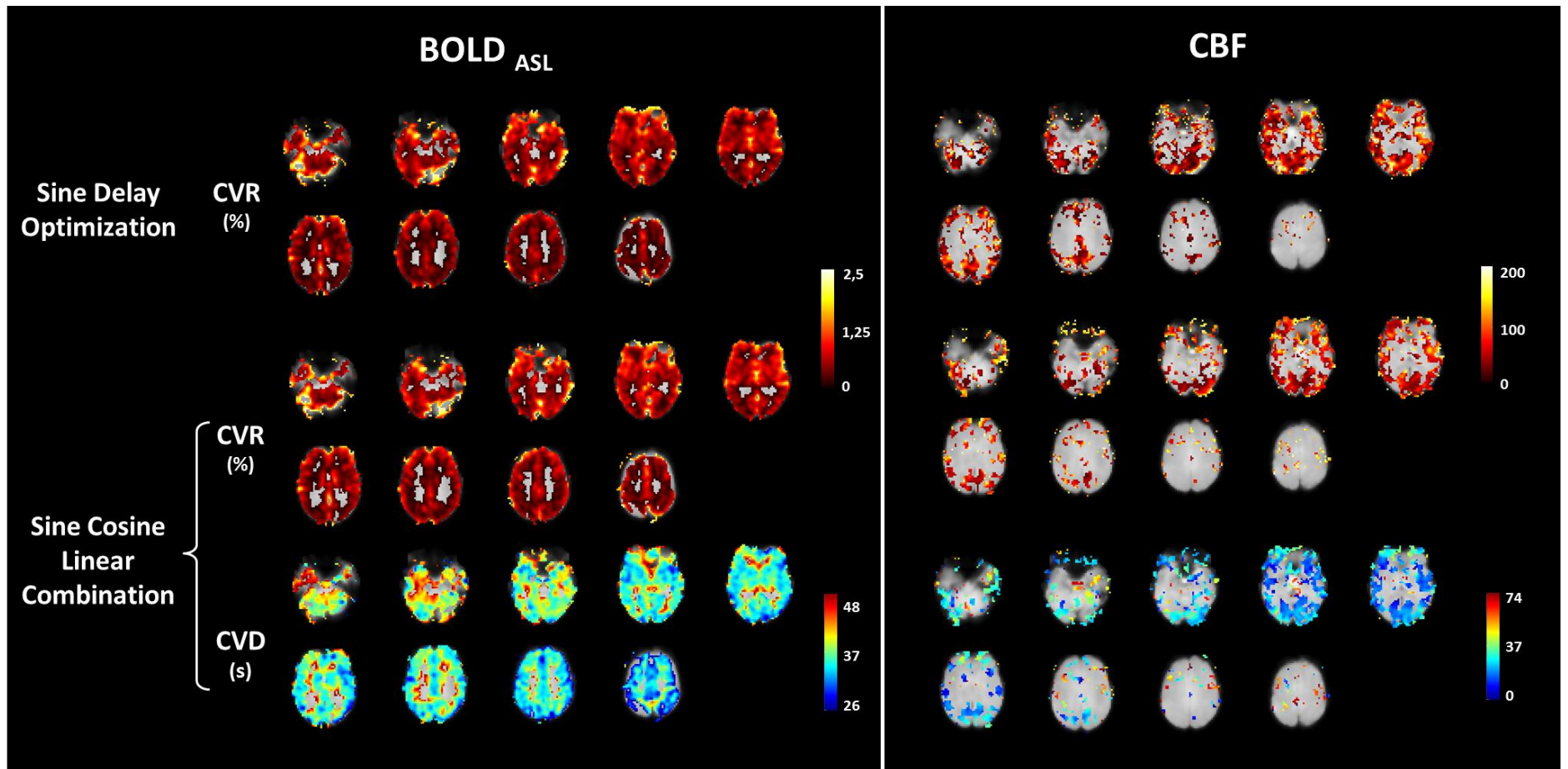


Figure 3.28: CVR and CVD maps obtained for subject R6, using the two modelling approaches (SDO and SCC) and for the two ASL contrasts, $BOLD_{ASL}$ and CBF. For the SDO approach only the CVR maps (top rows) are presented since the value of delay obtained is global (not voxel-by-voxel). For the SCC approach both CVR (third and fourth rows) and CVD maps (last two rows) are presented. The CVR values are in percentage and the CVD values are in seconds.

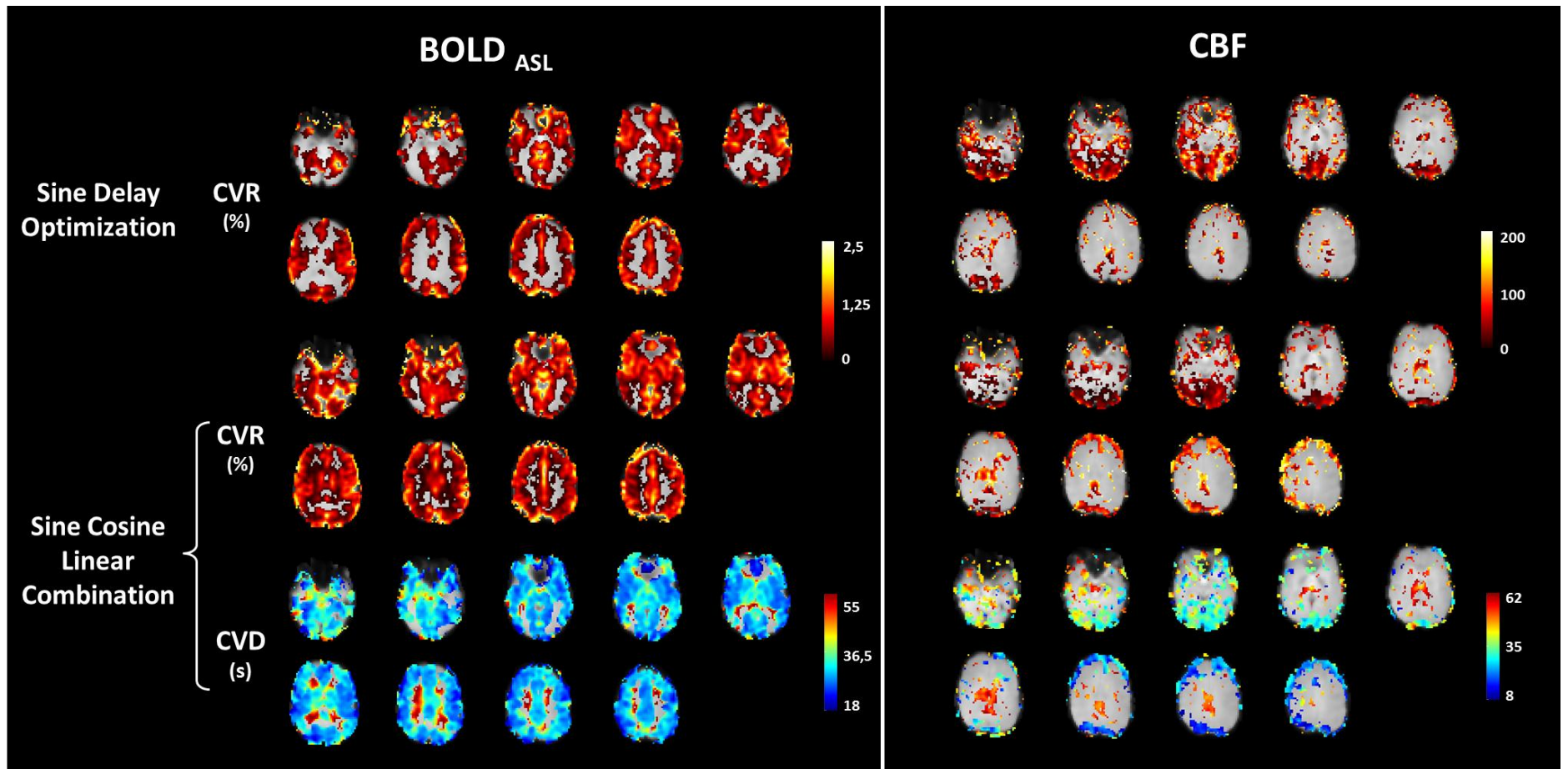


Figure 3.29: CVR and CVD maps obtained for subject R7, using the two modelling approaches (SDO and SCC) and for the two ASL contrasts, BOLD_{ASL} and CBF. For the SDO approach only the CVR maps (top rows) are presented since the value of delay obtained is global (not voxel-by-voxel). For the SCC approach both CVR (third and fourth rows) and CVD maps (last two rows) are presented. The CVR values are in percentage and the CVD values are in seconds.

The maps obtained are more extended for BOLD_{ASL} than CBF contrast, as expected, due to the higher sensitivity of the former.

Also, CVR values for the grey matter seem to be higher than the CVR values of white matter. Relatively to the delays, a pattern between grey/white matters can be seen, particularly in Subject R7, where white matter areas seem to have relatively longer delays. This is consistent with other studies [21].

3.4. Breath-Hold Protocol Comparison

In this section the two BH protocols employed (with and without preparatory inspiration) are going to be compared. Only the results obtained using the SCC approach will be used for this purpose.

3.4.1. Spatial Measurements

The comparison will be performed in terms of spatial measurements of each subject: number of responsive voxels, mean CVR values and optimal/most representative CVD values.

The spatial measurements values for the BH protocol without preparatory inspiration and using the SCC approach were already presented in Section 3.3.1. Nevertheless, these results will be repeated in the next sections to allow better comparison.

Group maps will be showed in order to see if there are any patterns between subjects and different protocols.

Data from subject R1 in the BOLD analyses and subject R3 in CBF and BOLD_{ASL} analyses were excluded for reasons stated in Section 3.2 (head motion).

3.4.1.1. Number of Responsive Voxels

The values of the number of responsive voxels obtained for each subject using the two BH protocols for each of three contrasts considered are presented in Table 3.7 and Figure 3.10 and Figure 3.11.

Table 3.7: Number of responsive voxels for each subject using the two BH protocols for each of the contrasts considered (BOLD, BOLD_{ASL} and CBF).

Number of responsive voxels	With Preparatory Inspiration			Without Preparatory Inspiration		
	Subjects	BOLD	BOLD _{ASL}	CBF	BOLD	BOLD _{ASL}
R1	-	7071	6039	10455	10007	3759
R2	13228	12158	5370	11912	12425	6054
R3	7988	-	-	9544	7998	6159
R4	14918	12617	3646	13995	11467	3101
R5	13780	10835	3860	11648	10703	3837
R6	8909	10007	4627	11847	10346	3808
R7	10304	11730	6438	13777	12244	5331
mean ± standard deviation	(11 ± 3)×10 ³	(11± 2) ×10 ³	(5±1)×10 ³	(12±2)×10 ³	(11±1)×10 ³	(5±1)×10 ³

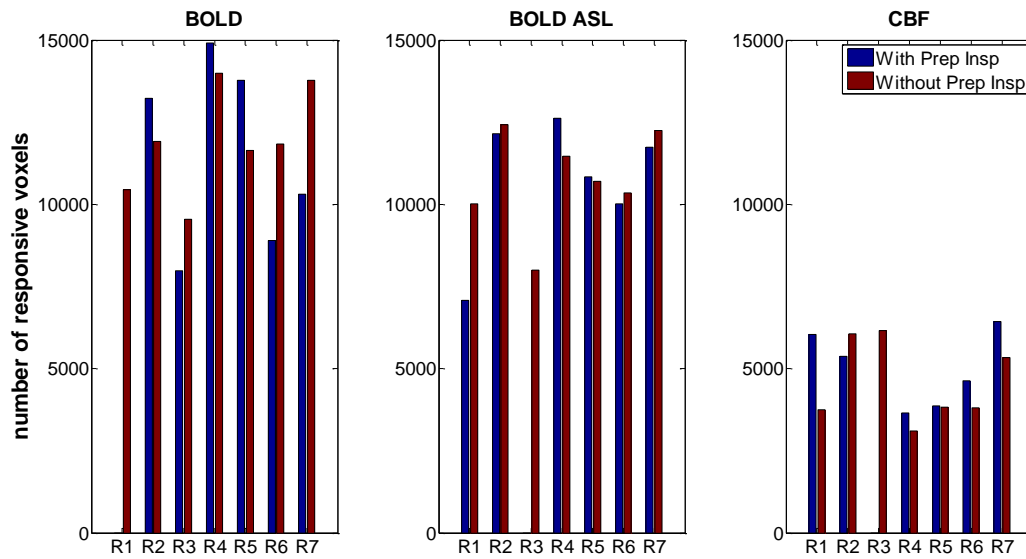


Figure 3.30: Bar chart of number of responsive voxels for each subject using the BH protocol with preparatory inspiration (With Prep Insp) and without preparatory inspiration (Without Prep Insp) for each of the contrasts considered (BOLD, BOLD_{ASL} and CBF).

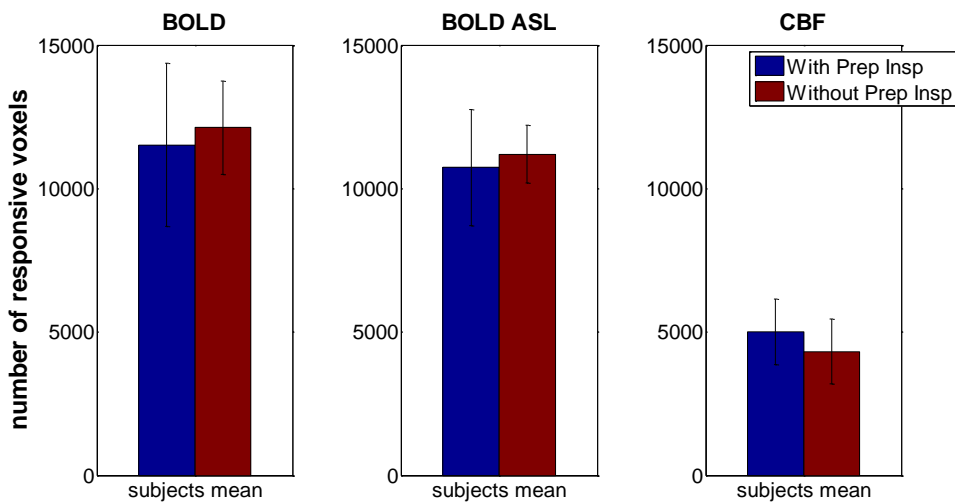


Figure 3.31: Bar chart of the mean number of responsive voxels across subjects using the BH protocol with preparatory inspiration (With Prep Insp) and without preparatory inspiration (Without Prep Insp) for each of the contrasts considered (BOLD, BOLD_{ASL} and CBF). Error bars represent standard deviations of the mean.

The BOLD and BOLD_{ASL} number of responsive voxels are much higher than the CBF number of responsive voxels in both BH protocols. No significant differences in the number of responsive voxels were found for BOLD, BOLD_{ASL} and CBF data by using the two BH protocols.

3.4.1.2. Cerebrovascular Delay Values

The representative CVD values obtained using the two protocols, for the three contrasts, in each subject, are presented in Table 3.8, Figure 3.32 and Figure 3.33.

Table 3.8: Global delay values in seconds for each subject using the two BH protocols, for each of the contrasts considered (BOLD, BOLD_{ASL} and CBF).

CVD (s)	With Preparatory Inspiration			Without Preparatory Inspiration		
Subjects	BOLD	BOLD _{ASL}	CBF	BOLD	BOLD _{ASL}	CBF
R1	-	49	41	19	14	58
R2	47	42	45	32	30	29
R3	26	-	-	21	20	26
R4	35	38	37	31	29	46
R5	26	33	42	20	22	50
R6	42	40	42	31	34	16
R7	37	39	12	29	29	27
mean ± standard deviation	36±9	40±5	37±12	26±6	25±7	36±15

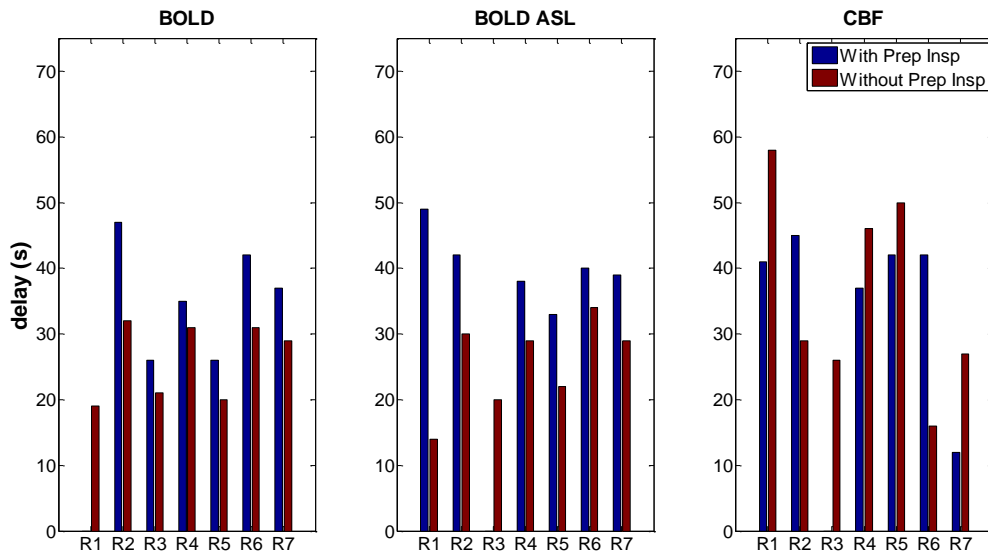


Figure 3.32: Bar chart of global delays of each subject using the BH protocol with preparatory inspiration (With Prep Insp) and without preparatory inspiration (Without Prep Insp) for each of the contrasts considered (BOLD, BOLD_{ASL} and CBF).

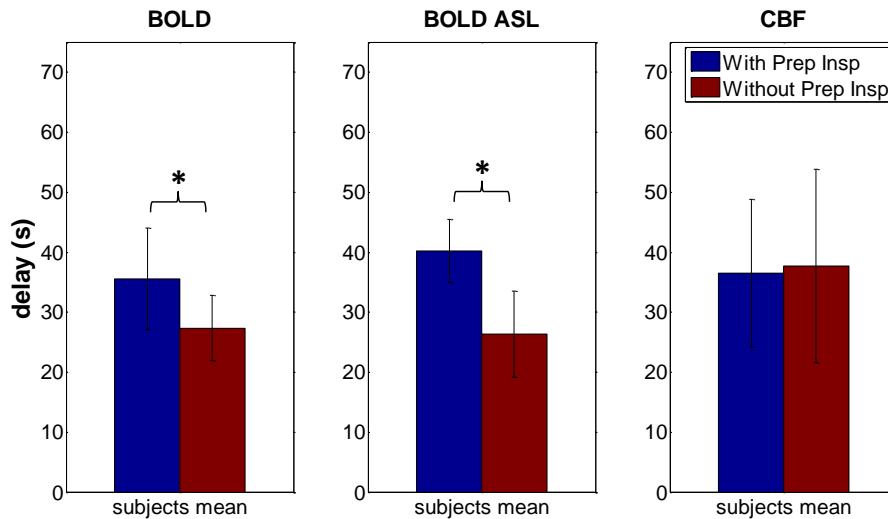


Figure 3.33: Bar chart of the mean CVD values across subjects using the BH protocol with preparatory inspiration (With Prep Insp) and without preparatory inspiration (Without Prep Insp) for each of the contrasts considered (BOLD, BOLD_{ASL} and CBF). Error bars represent standard deviations of the mean and * represents significant differences ($p < 0.005$).

The BOLD and BOLD_{ASL} CVD values using a BH protocol with preparatory inspiration are, in all subjects, higher than the CVD values using a BH protocol without a preparatory inspiration. This probably occurs because the initial response to the preparatory inspiration shifts the BOLD increase in response to the BH in that case. No significant differences were observed for CBF data.

3.4.1.3. Cerebrovascular Reactivity Values

The mean CVR values for each subject using the two BH protocols for each of three contrasts considered are shown in Table 3.9 and Figure 3.34 and Figure 3.35.

Table 3.9: CVR values in percent signal change for each subject using the two BH protocols, for each of the contrasts considered (BOLD, BOLD_{ASL} and CBF).

CVR (%)	With Preparatory Inspiration			Without Preparatory Inspiration		
	BOLD	BOLD _{ASL}	CBF	BOLD	BOLD _{ASL}	CBF
Subjects						
R1	-	1.05	121.00	2.82	0.98	127.70
R2	3.26	1.09	138.00	2.96	1.13	89.30
R3	3.22	-	-	2.93	1.05	92.00
R4	2.68	0.86	118.00	3.00	0.97	115.40
R5	2.50	0.99	107.00	2.41	0.78	76.10
R6	1.70	0.56	74.00	2.05	0.68	81.50
R7	2.35	0.78	105.00	2.35	0.78	88.40
Mean ± standard deviation	2.6±0.6	0.9±0.2	111±22	2.7±0.4	0.9±0.2	96±19

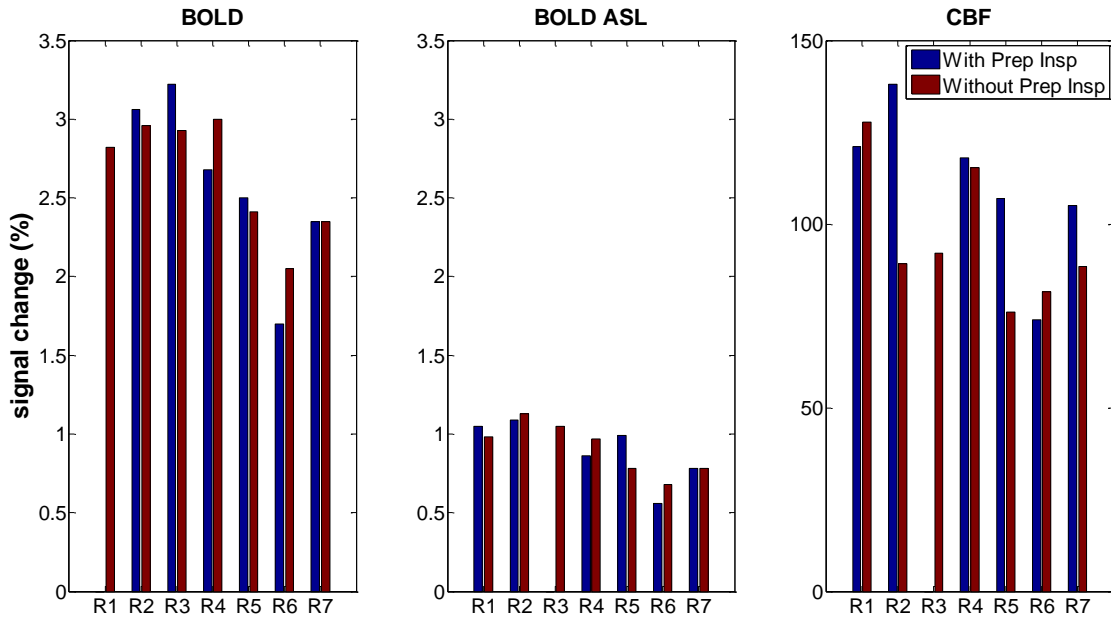


Figure 3.34: Bar chart of global reactivity values of each subject using the BH protocol with preparatory inspiration (With Prep Insp) and without preparatory inspiration (Without Prep Insp) for each of the contrasts considered (BOLD, BOLD_{ASL} and CBF)..

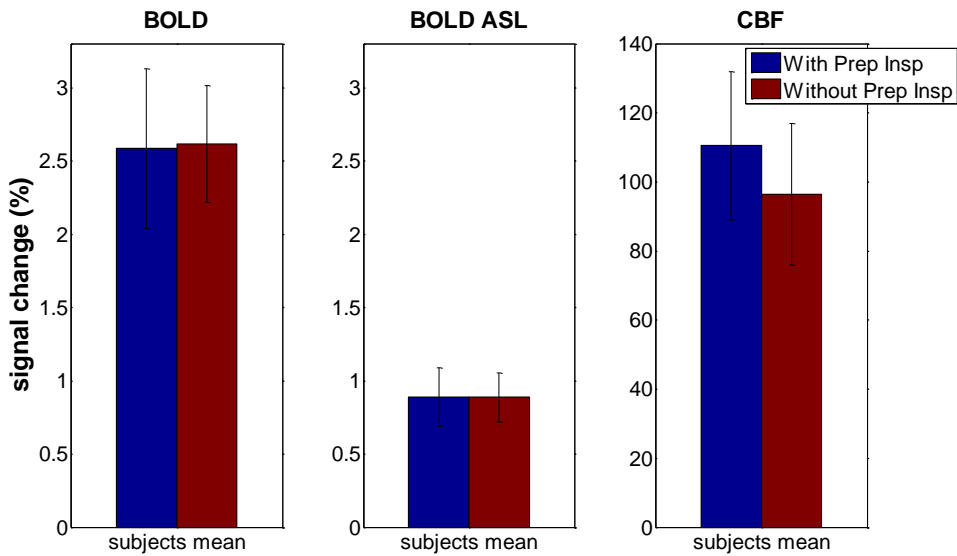


Figure 3.35: Bar chart of the mean CVR values across subjects using the BH protocol with preparatory inspiration (With Prep Insp) and without preparatory inspiration (Without Prep Insp) for each of the contrasts considered (BOLD, BOLD_{ASL} and CBF). Error bars represent standard deviations of the mean

The CVR values for CBF are much higher than the corresponding BOLD or BOLD_{ASL} values, as expected. BOLD_{ASL} reactivity values are smaller than BOLD due to the not optimal acquisition sequence used in the ASL experiment. No significant differences between CVR values of both BH protocols were found for BOLD, BOLD_{ASL} and CBF data.

3.4.2. Cerebrovascular Reactivity and Delay Maps

3.4.2.1. Group Maps

Group maps and measurements were computed in order to identify spatial patterns across subjects. Only the results obtained using the SCC approach will be analysed, since they provide CVD maps as well as CVR maps. The maps obtained using the BH protocol with preparatory inspiration will be present firstly and the maps obtained using the BH protocol without preparatory inspiration will be present after.

The CVD and CVR maps of each subject were registered to the standard MNI space. The masks obtained after registration are depicted in Figure 3.36 and Figure 3.50 for the BH protocol with and without preparatory inspiration, respectively. Subject R7 data was not used in group analysis due to the fact that we didn't acquired a MPRAGE image (structural) for this subject. For analysis using the BH protocol with preparatory inspiration datasets, subject R3 was also not used due to high levels of motion. A total of 6 and 5 subjects were used in the group analysis of the BH protocol without preparatory inspiration and in the group analysis of the BH protocol with preparatory inspiration, respectively. Group maps were then obtained by averaging the corresponding maps of all subjects already thresholded as described in Section 3.3.2. For the maps using the BH protocol with preparatory inspiration only the voxels that were responsive in more than two subjects are displayed on the mean maps. For the maps using the BH protocol without preparatory inspiration only the voxels that were responsive in more than three subjects are displayed on the mean maps. Also, if the voxel's standard deviation was greater than 25, those voxels are not shown in the maps.

With Preparatory Inspiration

The next eight figures are relative to the BH protocol with preparatory inspiration.

Figure 3.36 shows the sum of all subject masks, registered to the MNI standard space, showing degree of overlap of acquired ASL data coverage across all subjects.

Figure 3.37 and Figure 3.38 display the CVD and CVR group maps of the $BOLD_{ASL}$ BH responses, respectively.

Figure 3.39 corresponds to the map of number of subjects exhibiting a significant $BOLD_{ASL}$ response and Figure 3.54 corresponds to the standard deviation of the delays of $BOLD_{ASL}$ response.

Figure 3.55 and Figure 3.56 display the CVD and CVR group maps of the CBF BH responses respectively.

Figure 3.57 corresponds to the map of number of subjects exhibiting a significant CBF response and Figure 3.58 corresponds to the standard deviation of the delays of CBF data.

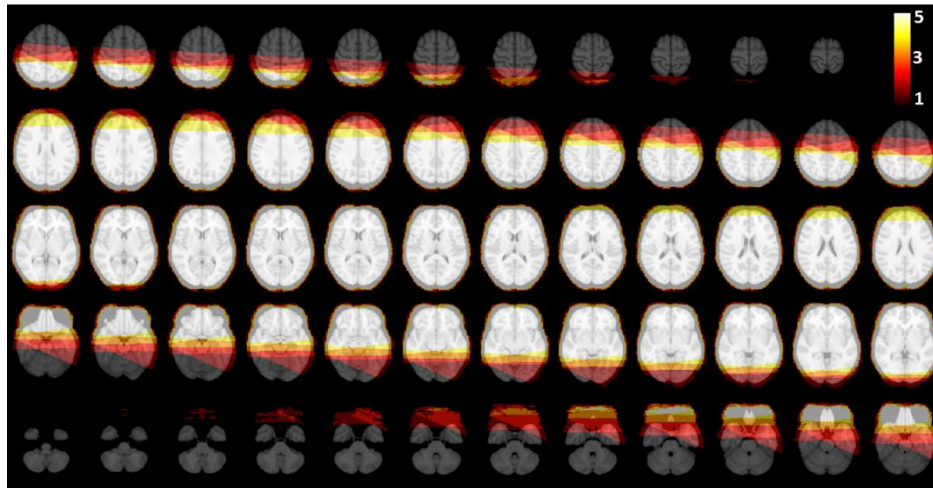


Figure 3.36: Sum of all subject masks, overlaid on the T1-weighted structural image of the MNI standard brain.

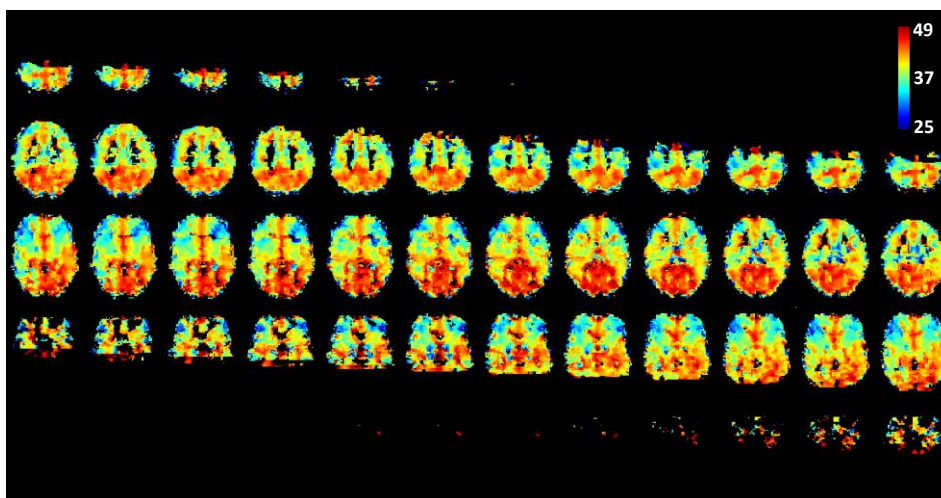


Figure 3.37: Mean CVD map of $BOLD_{ASL}$ responses across subjects, in the MNI standard space, using the BH protocol with preparatory inspiration. Delays are in seconds.

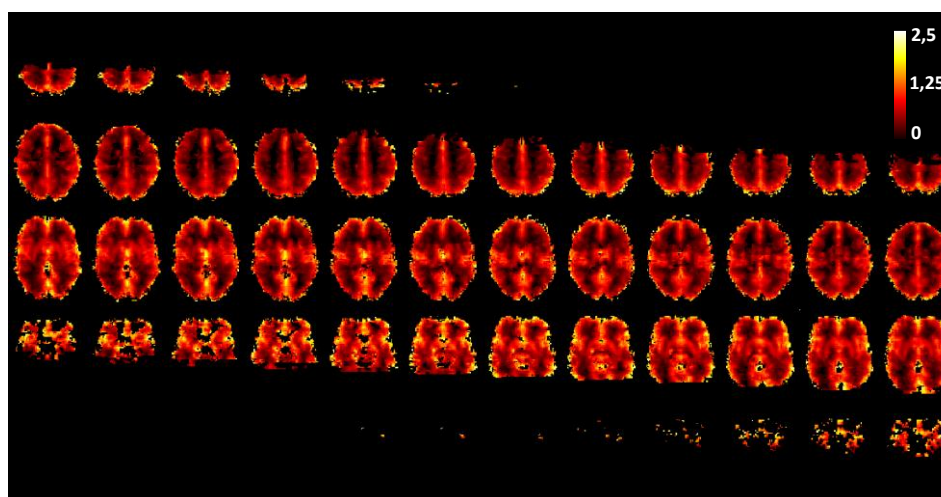


Figure 3.38: Mean CVR map of $BOLD_{ASL}$ responses across subjects, in the MNI standard space, using the BH protocol with preparatory inspiration. Reactivity is in percentage.

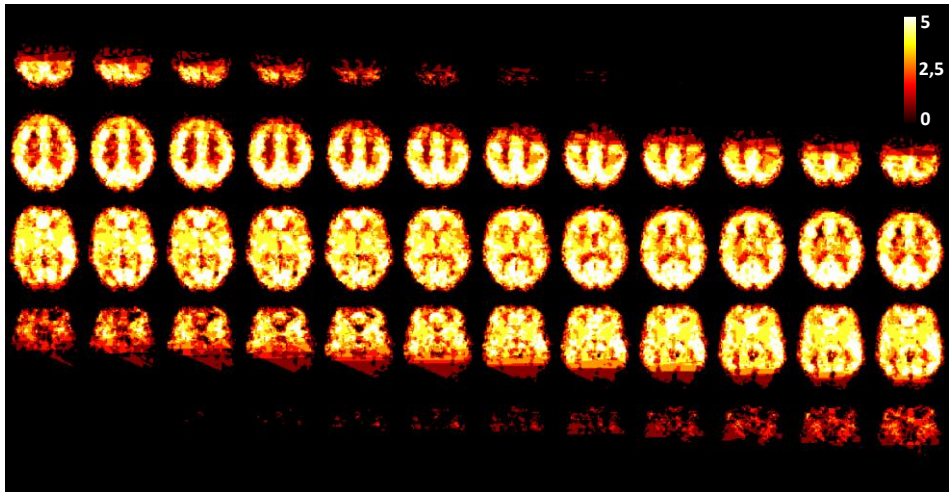


Figure 3.39: Map of number of subjects exhibiting a significant $BOLD_{ASL}$ response, using the BH protocol with preparatory inspiration in the MNI standard space.

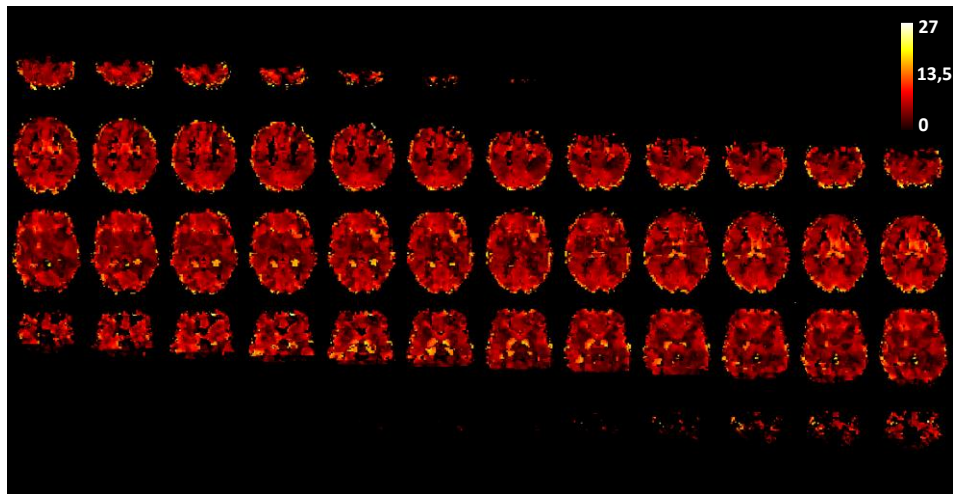


Figure 3.40: Standard deviation of the values of CVD of $BOLD_{ASL}$ responses across subjects, in the MNI standard space, using the BH protocol with preparatory inspiration .

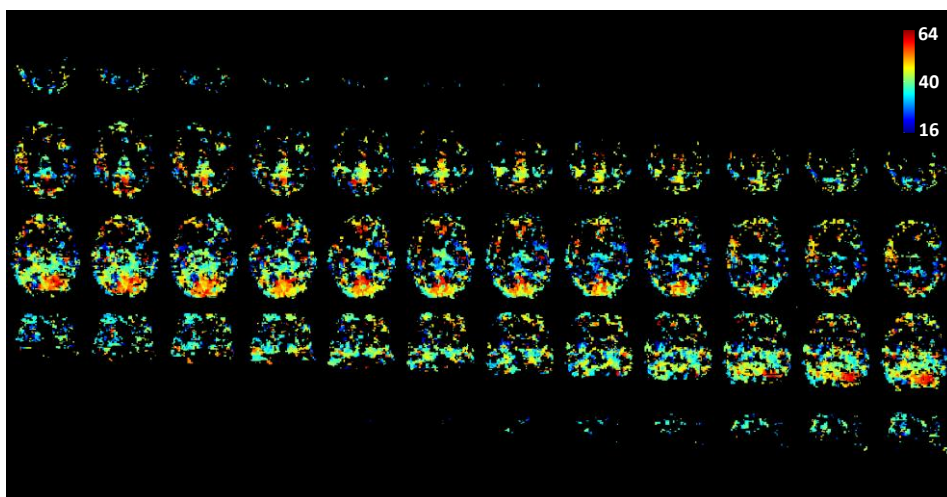


Figure 3.41: Mean CVD map of CBF responses across subjects, in the MNI standard space, using the BH protocol with preparatory inspiration. Delays are in seconds.

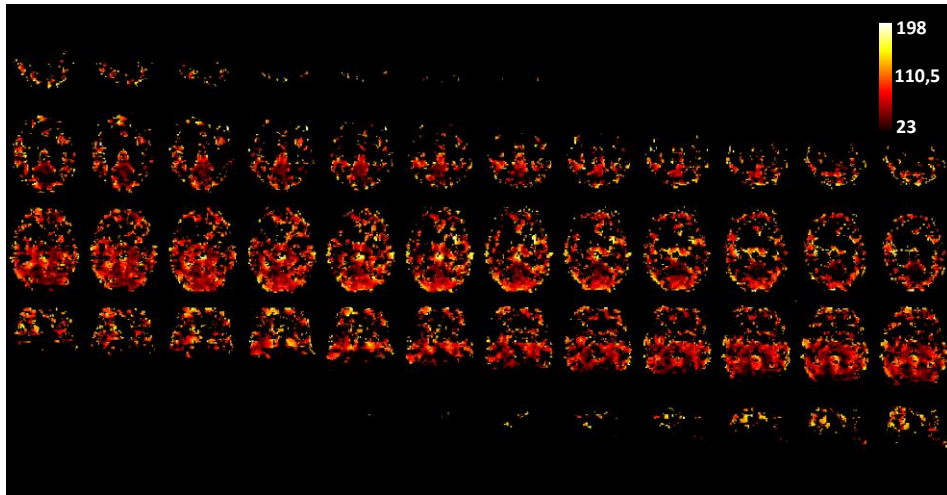


Figure 3.42: Mean CVR map of CBF responses across subjects, in the MNI standard space, using the BH protocol with preparatory inspiration. Reactivity is in percentage.

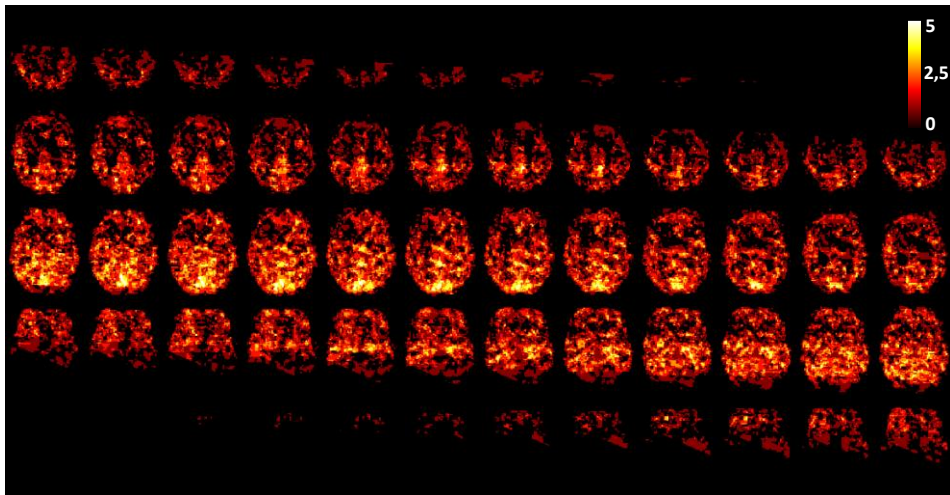


Figure 3.43: Map of number of subjects exhibiting a significant CBF response, in the MNI standard space, using the BH protocol with preparatory inspiration.

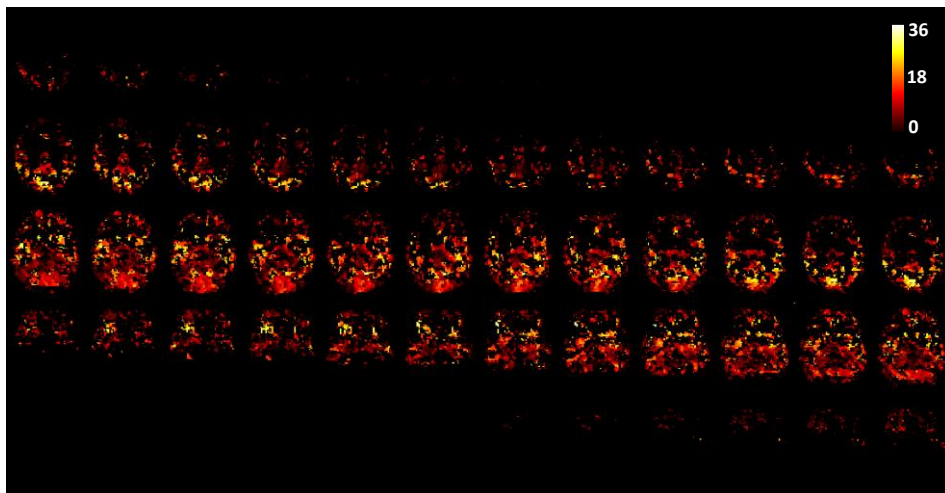


Figure 3.44: Standard deviation of the values of CVD of CBF responses across subjects, in the MNI standard space using the BH protocol with preparatory inspiration.

BOLD_{ASL} and CBF CVD maps show that occipital areas have longer delays than non-occipital areas. For that reason, we computed mean CVD values in those areas (Figure 3.45).

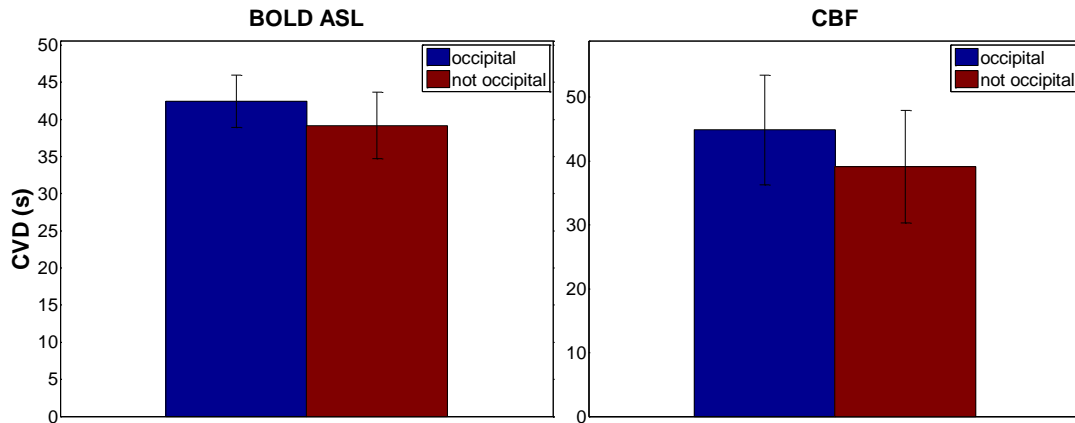


Figure 3.45: Mean of CVD values of subjects across specific brain regions (occipital and non-occipital), using the BH protocol with preparatory inspiration. Error bars represent standard deviations of the mean.

The occipital region of the brain indeed has, on average, longer delays.

BOLD_{ASL} CVR maps show that white matter regions have lower values of CVR relative to the grey matter regions. We computed mean grey and white matter values for each subject (Figure 3.46 and Figure 3.47) and the mean values for all subjects (Figure 3.48 and Figure 3.49).

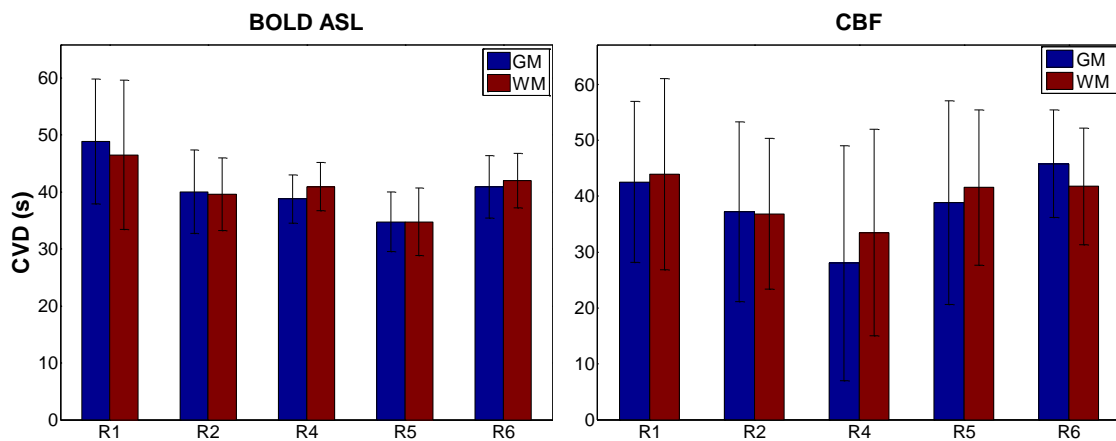


Figure 3.46: Mean of CVD values across specific brain regions for each subject, using the BH protocol with preparatory inspiration. Error bars represent standard deviations of the mean. GM and WM correspond to grey matter and white matter, respectively.

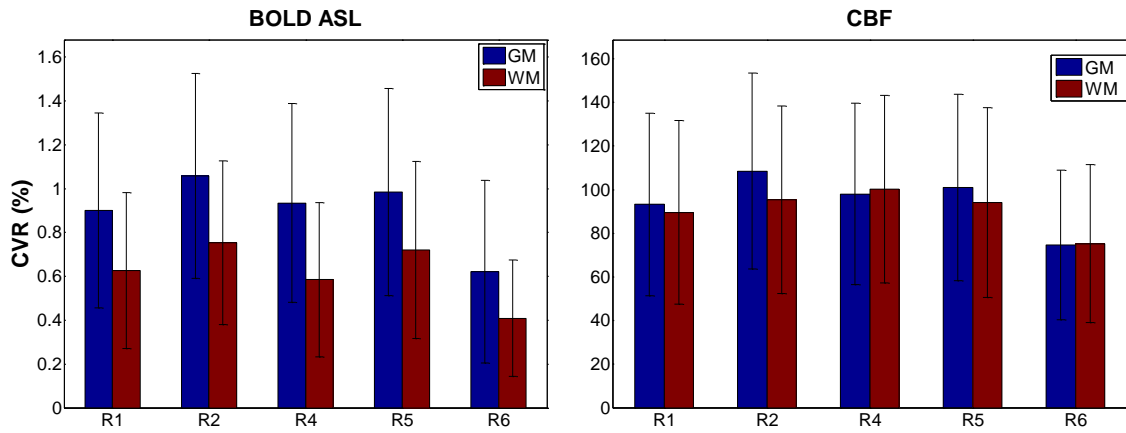


Figure 3.47: Mean of CVR values across specific brain regions for each subject, using the BH protocol with preparatory inspiration. Error bars represent standard deviations of the mean. GM and WM correspond to grey matter and white matter, respectively.

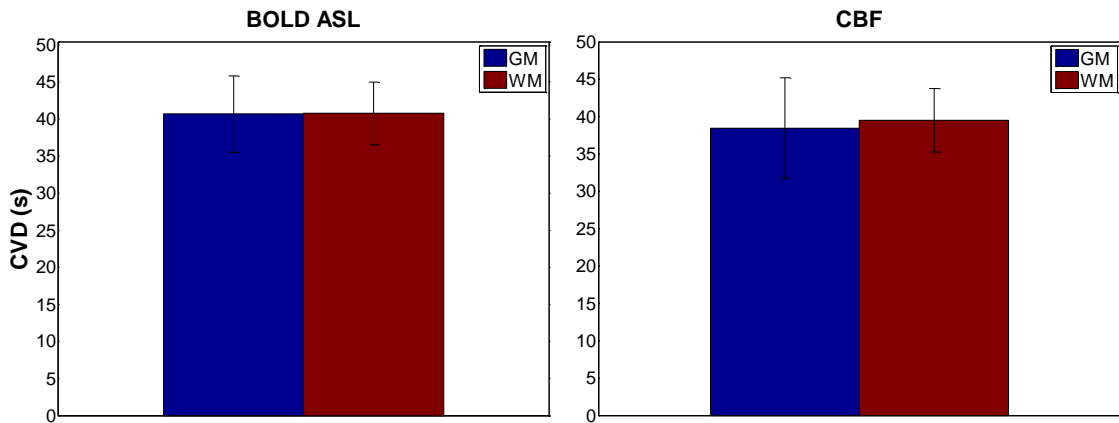


Figure 3.48: Mean of CVD values across specific brain regions, using the BH protocol with preparatory inspiration. Error bars represent standard deviations of the mean. GM and WM correspond to grey matter and white matter, respectively.

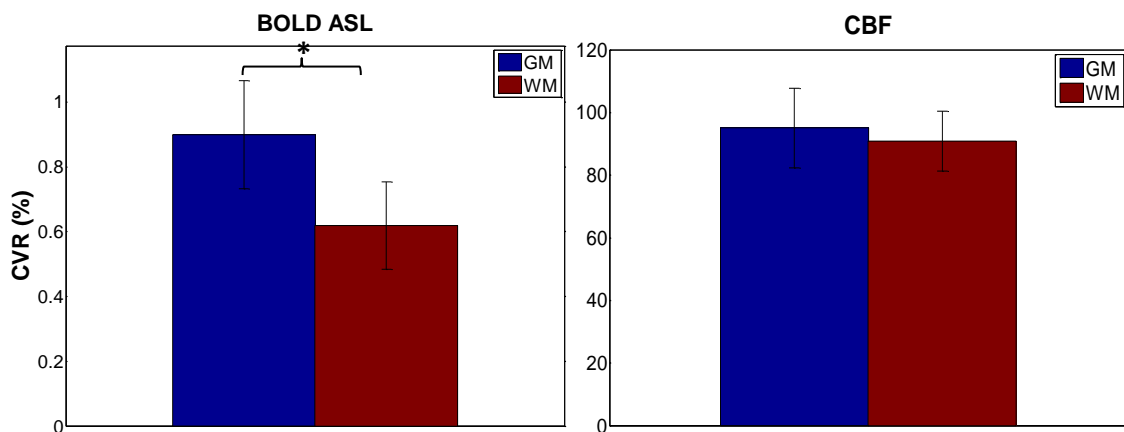


Figure 3.49: Mean of CVR values across specific brain regions using the BH protocol with preparatory inspiration. Error bars represent standard deviations of the mean. GM and WM correspond to grey matter and white matter, respectively. * represents significant differences ($p < 0.005$).

In fact, $BOLD_{ASL}$ CVR white matter values are much lower than CVR grey matter values. No significant differences are observed in the CVD values of these areas for the two contrasts (CBF and $BOLD_{ASL}$) or in the CVR values of CBF data.

Without Preparatory Inspiration

The next eight figures are relative to the BH protocol without preparatory inspiration.

Figure 3.50 shows the sum of all subject masks, registered to the MNI standard space, showing degree of overlap of acquired ASL data coverage across all subjects.

Figure 3.51 and Figure 3.52 display the CVD and CVR group maps of the $BOLD_{ASL}$ BH responses, respectively.

Figure 3.53 corresponds to the map of number of subjects exhibiting a significant $BOLD_{ASL}$ response and Figure 3.54 corresponds to the standard deviation of the delays of $BOLD_{ASL}$ response.

Figure 3.55 and Figure 3.56 display the CVD and CVR group maps of the CBF BH responses respectively.

Figure 3.57 corresponds to the map of number of subjects exhibiting a significant CBF response and Figure 3.58 corresponds to the standard deviation of the delays of CBF data.

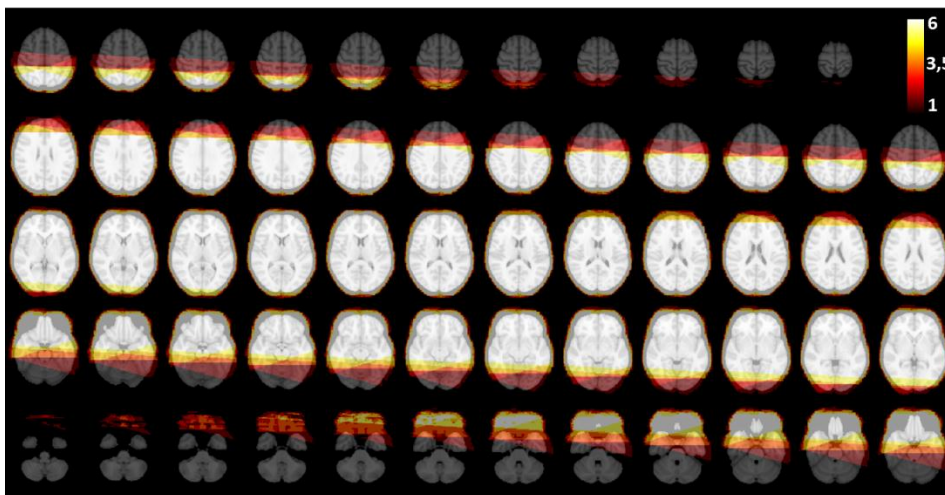


Figure 3.50: Sum of all subject masks, overlaid on the T1-weighted structural image of the MNI standard brain, using the BH protocol without preparatory inspiration.

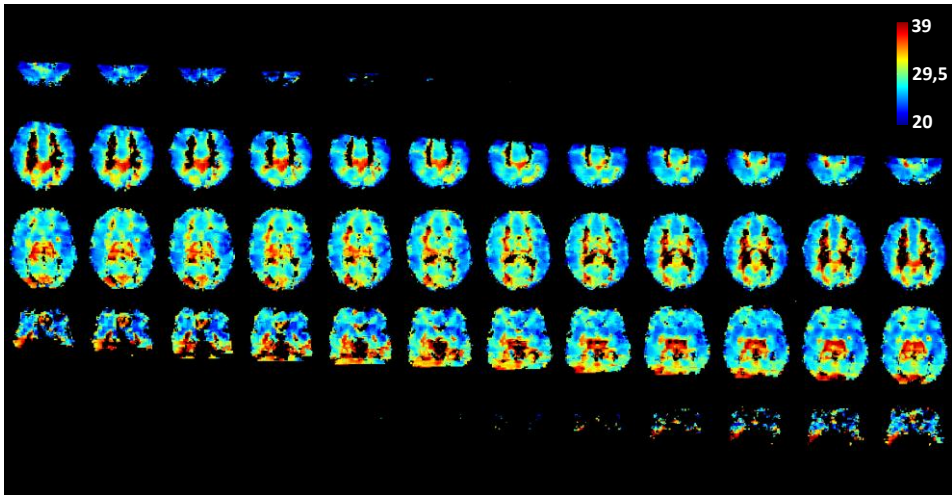


Figure 3.51: Mean CVD map of BOLD_{ASL} responses across subjects, in the MNI standard space, using the BH protocol without preparatory inspiration. Delays are in seconds.

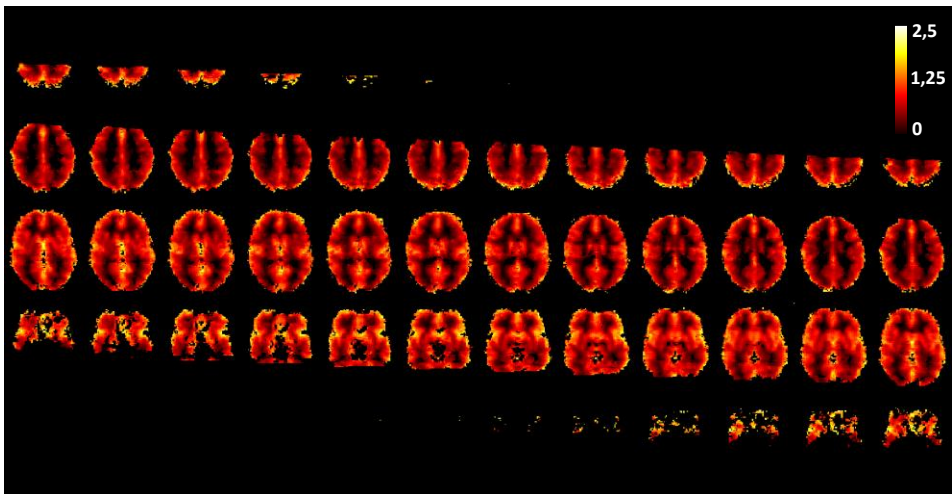


Figure 3.52: Mean CVR map of BOLD_{ASL} responses across subjects, in the MNI standard space, using the BH protocol without preparatory inspiration. Reactivity is in percentage.

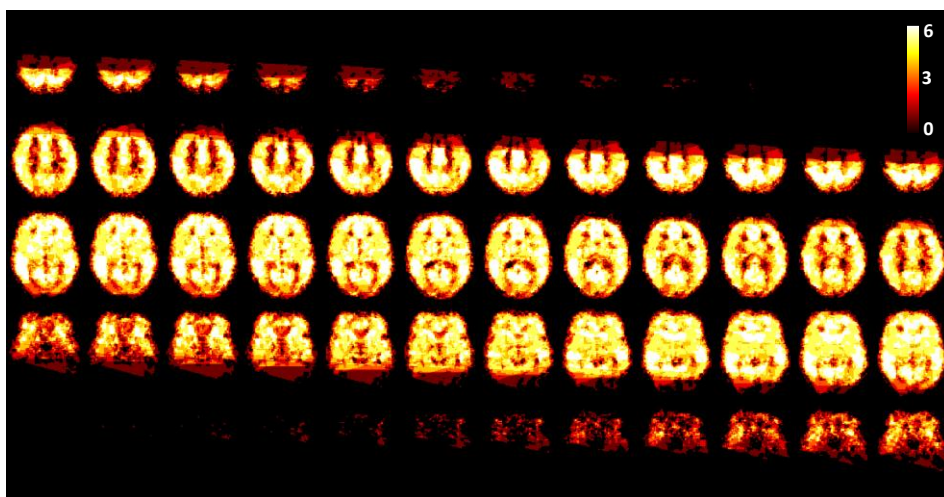


Figure 3.53: Map of number of subjects exhibiting a significant BOLD_{ASL} response, in the MNI standard space, using the BH protocol without preparatory inspiration.

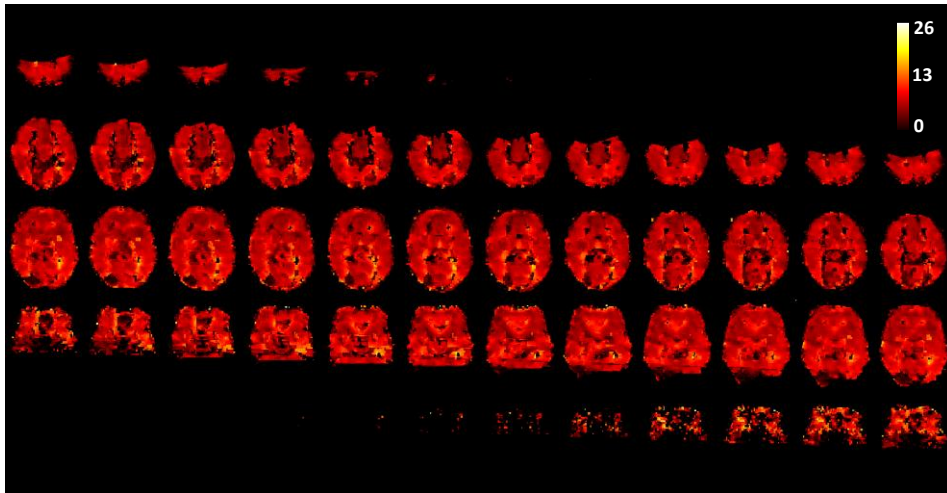


Figure 3.54: Standard deviation of the values of CVD of $BOLD_{ASL}$ responses across subjects, in the MNI standard space, using the BH protocol without preparatory inspiration.

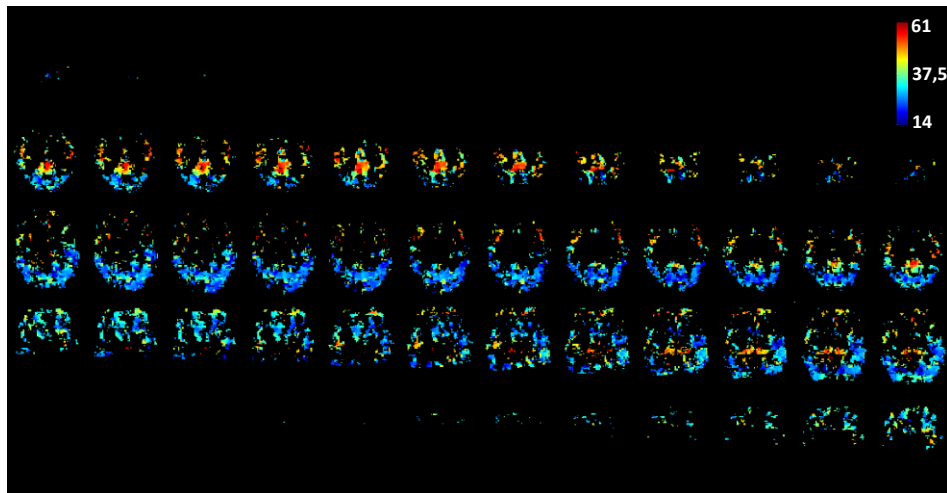


Figure 3.55 Mean CVD map of CBF responses across subjects, in the MNI standard space, using the BH protocol without preparatory inspiration. Delays are in seconds.

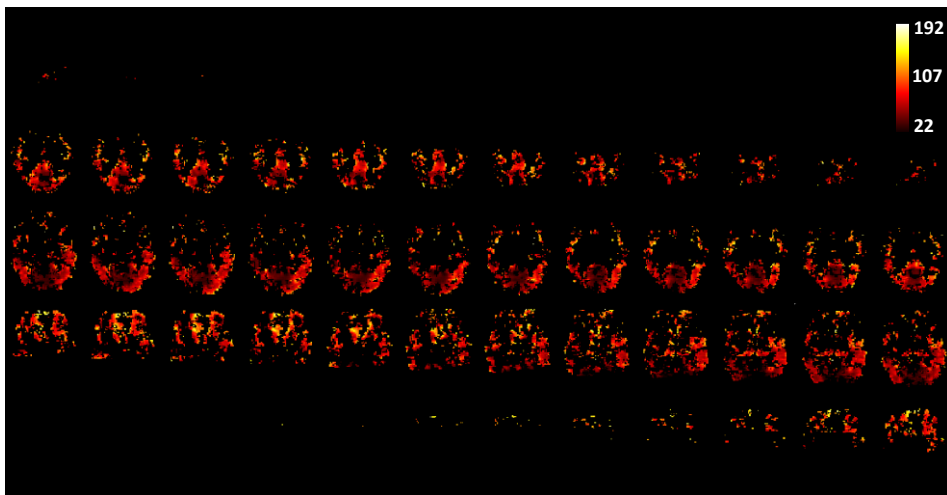


Figure 3.56: Mean CVR map of CBF responses across subjects, in the MNI standard space, using the BH protocol without preparatory inspiration. Reactivity is in percentage

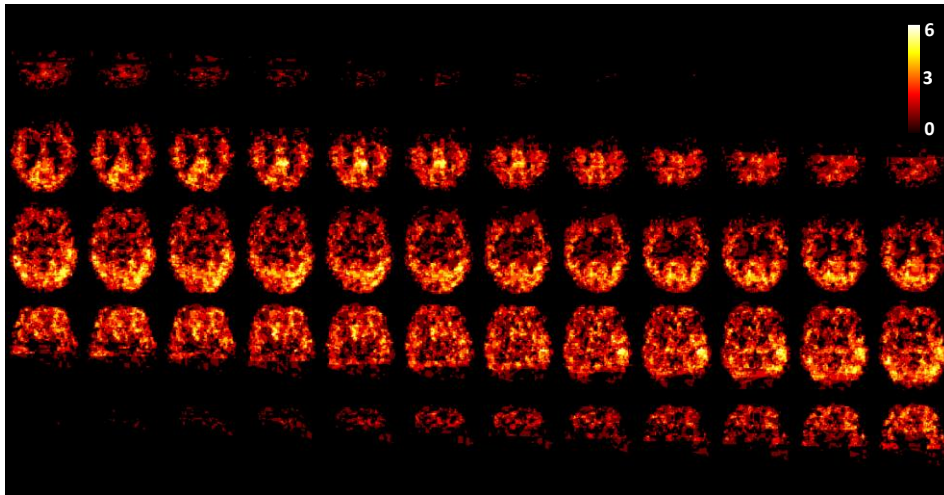


Figure 3.57: Map of number of subjects exhibiting a significant CBF response, in the MNI standard space, using the BH protocol without preparatory inspiration.

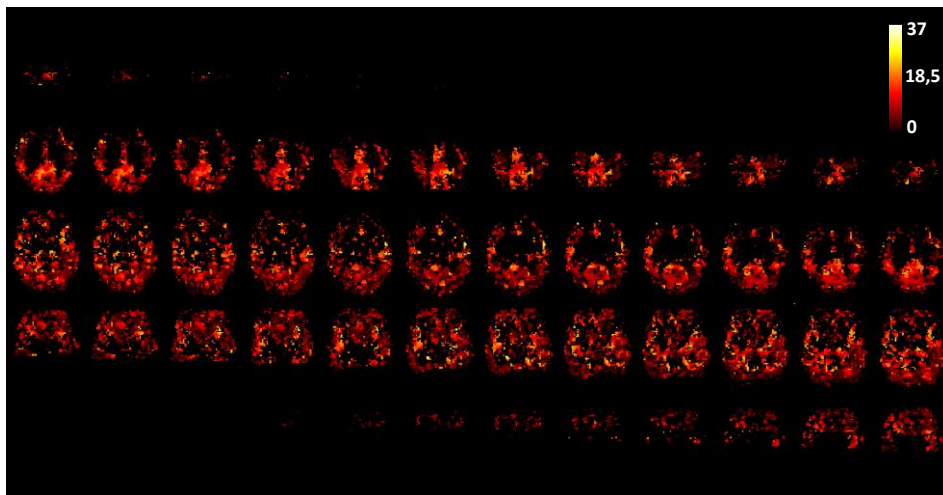


Figure 3.58: Standard deviation of the values of CVD of CBF responses across subjects, in the MNI standard space, using the BH protocol without preparatory inspiration.

We computed mean CVD values in the occipital and non-occipital areas (Figure 3.59).

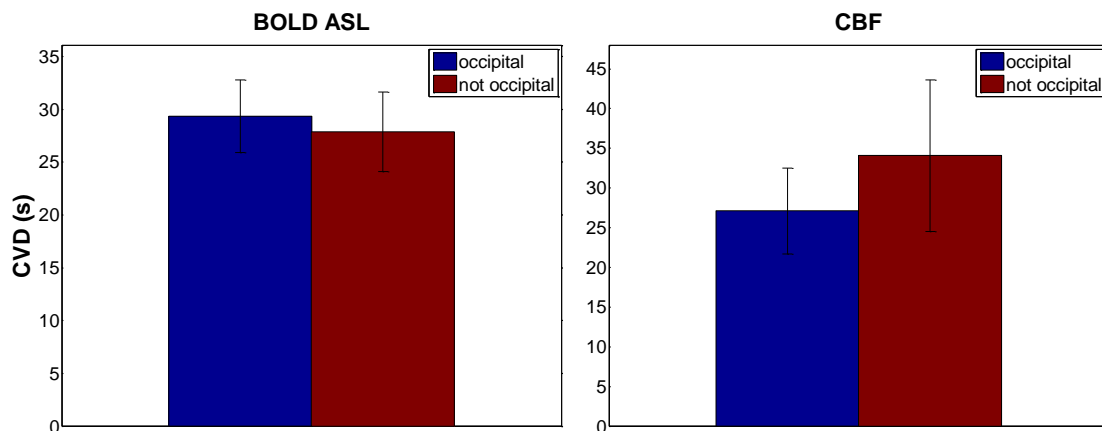


Figure 3.59: Mean and standard deviation of CVD values in seconds of specific regions of the brain (occipital, non-occipital), using the BH protocol without preparatory inspiration.

For the BOLD_{ASL} data, occipital areas have longer delays, however the differences seem to be minimal. On the contrary, CBF areas that are not occipital have longer delays, contrarily to what happens using a BH protocol with preparatory inspiration.

Again, BOLD_{ASL} CVR maps show that white matter regions have smaller values of CVR relative to the grey matter regions. For that reason, we computed mean grey and white matter values for each subject (Figure 3.60 and Figure 3.61) and the mean values for all subjects (Figure 3.62 and Figure 3.63).

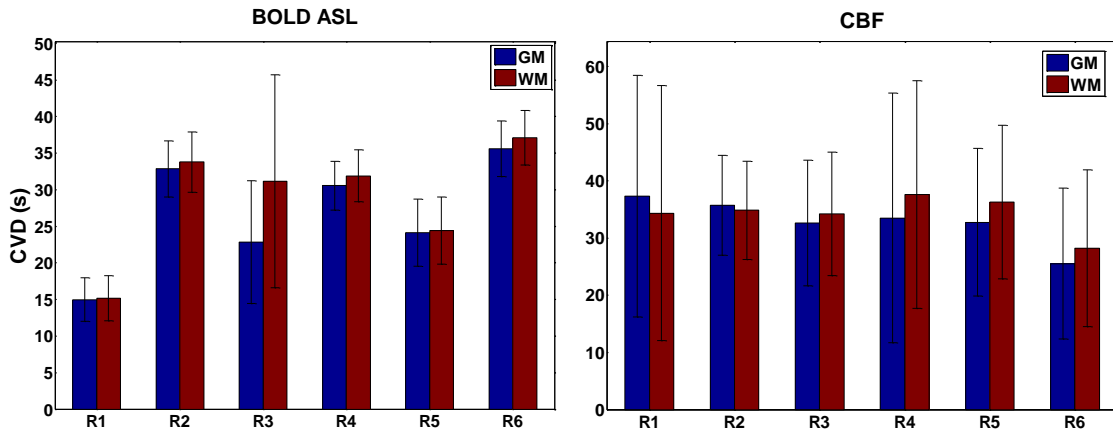


Figure 3.60: Mean of CVD values across specific brain regions for each subject, using the BH protocol without preparatory inspiration. Error bars represent standard deviations of the mean. GM and WM correspond to grey matter and white matter, respectively.

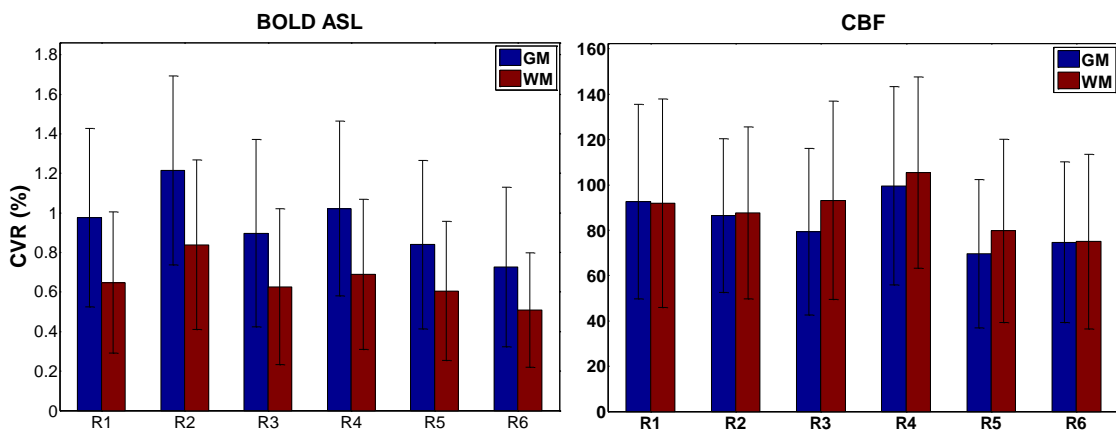


Figure 3.61: Mean of CVR values across specific brain regions for each subject, using the BH protocol without preparatory inspiration. Error bars represent standard deviations of the mean. GM and WM correspond to grey matter and white matter, respectively.

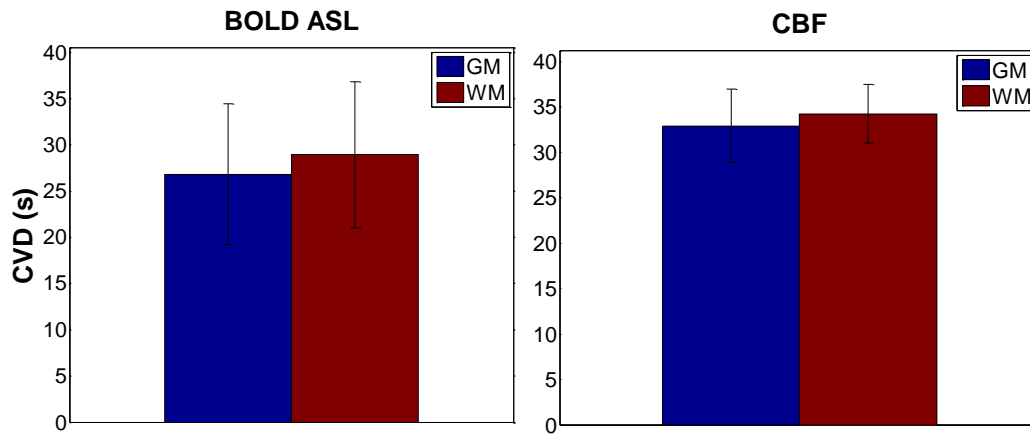


Figure 3.62: Mean of CVD values across specific brain regions, using the BH protocol without preparatory inspiration. Error bars represent standard deviations of the mean. GM and WM correspond to grey matter and white matter, respectively.

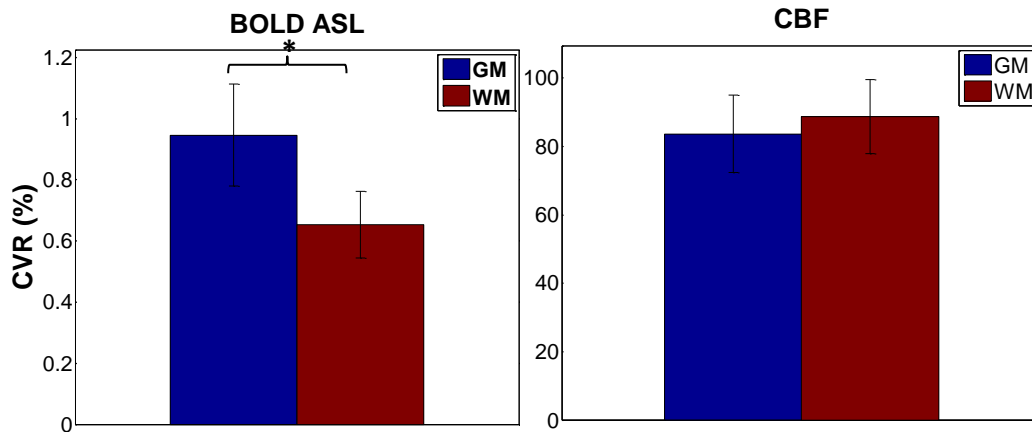


Figure 3.63: Mean of CVD values across specific brain regions, using the BH protocol without preparatory inspiration. Error bars represent standard deviations of the mean. GM and WM correspond to grey matter and white matter, respectively.

Again, $BOLD_{ASL}$ CVR white matter values are much lower than CVR grey matter values. No significant differences are observed in the CVD values of these areas for the two contrasts (CBF and $BOLD_{ASL}$) and in the CVR values of CBF data.

3.4.3. Time Courses

The average time courses of the BH responses in each subject and for each contrast and protocol, are presented in this section. Figure 3.64, Figure 3.65 and Figure 3.66 correspond to the time courses of BOLD, $BOLD_{ASL}$ and CBF responses to the breath-hold challenge with preparatory inspiration, respectively. Figure 3.67, Figure 3.68 and Figure 3.69 correspond to the time courses of BOLD, $BOLD_{ASL}$ and CBF responses to the breath-hold challenge without preparatory inspiration, respectively.

With Preparatory Inspiration

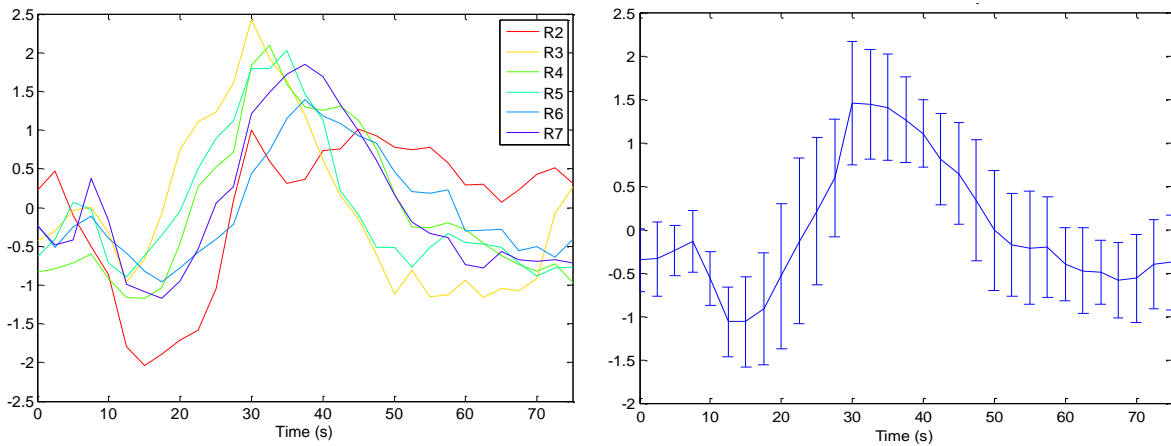


Figure 3.64: Time course of all subjects (left) and mean time course of all subjects (right) averaged over the BH with preparatory inspiration challenge blocks for BOLD signal. Subject R1 data was not used in this analysis due to high levels of motion.

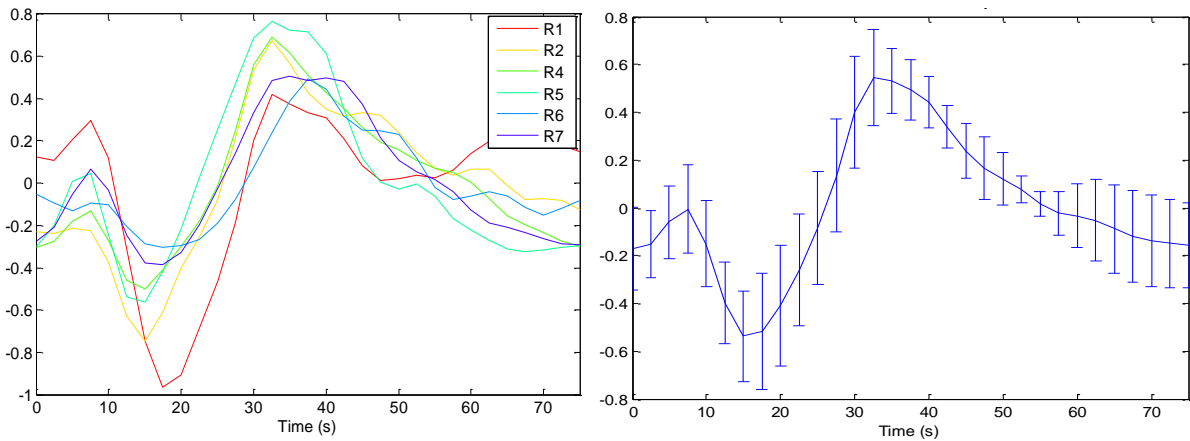


Figure 3.65: Time course of all subjects (left) and mean time course of all subjects (right) averaged over the BH with preparatory inspiration challenge blocks for BOLD_{ASL} signal. Subject R3 data was not used in this analysis due to high levels of motion.

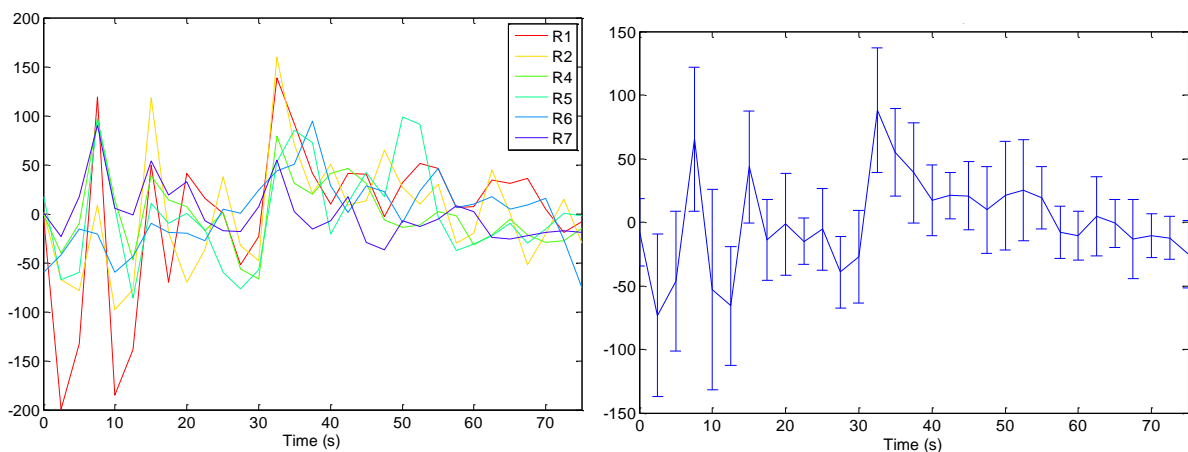


Figure 3.66: Time course of all subjects (left) and mean time course of all subjects (right) averaged over the BH with preparatory inspiration challenge blocks for CBF signal. Subject R3 data was not used in this analysis due to high levels of motion.

The time courses of the responses using respiratory task with a preparatory inspiration before the breath-hold show a complex shape. As it was expected and mentioned in Section 1.1.2., from the time courses we can see that there is an increase in BOLD signal as consequence of an increase in CBF (increase vasodilation because of the increase in $P_{ET}CO_2$) that corresponds to the main and later peak. However, there is a slight delay of this peak probably due to the fact that there seems to be two additional peaks in the beginning of the cycles. The first one, which is positive and appears sooner, can be seen clearly in the CBF time course (at approximately 8s). In the BOLD and $BOLD_{ASL}$ time courses this peak is also observed but not as clearly. A negative peak following the initial positive one is depicted in the BOLD and $BOLD_{ASL}$ time courses. As previously stated in Section 1.1.2 these variations are mainly due to a combination of several factors that are related to the respiratory act of inspiration. However these factors are still not well understood

Without Preparatory Inspiration

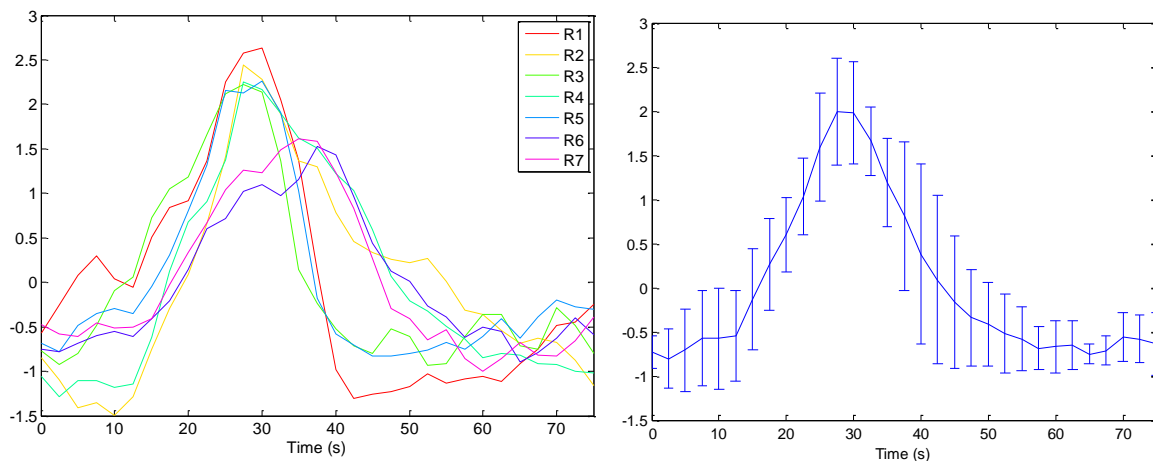


Figure 3.67: Time course of all subjects (left) and mean time course of all subjects (right) averaged over the BH without preparatory inspiration challenge blocks for BOLD signal.

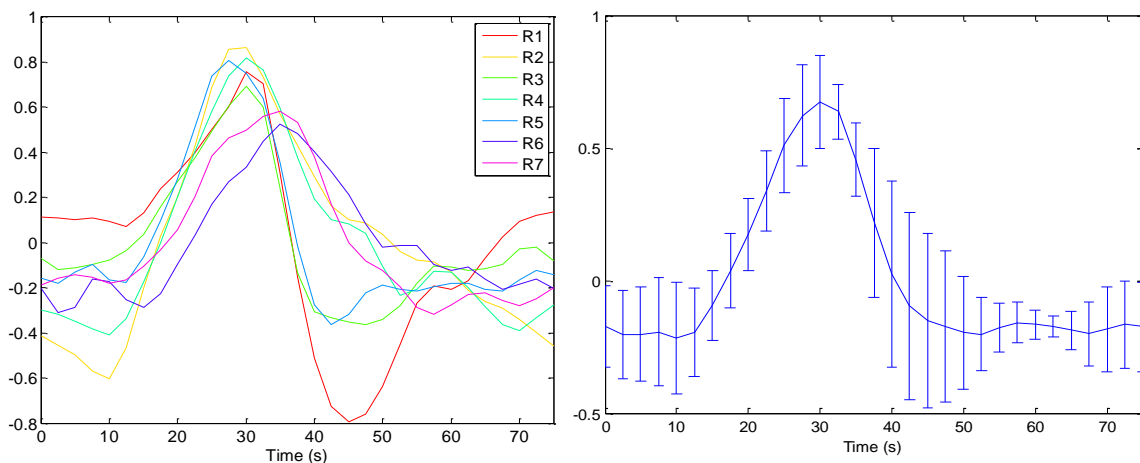


Figure 3.68: Time course of all subjects (left) and mean time course of all subjects (right) averaged over the BH without preparatory inspiration challenge blocks for $BOLD_{ASL}$ signal.

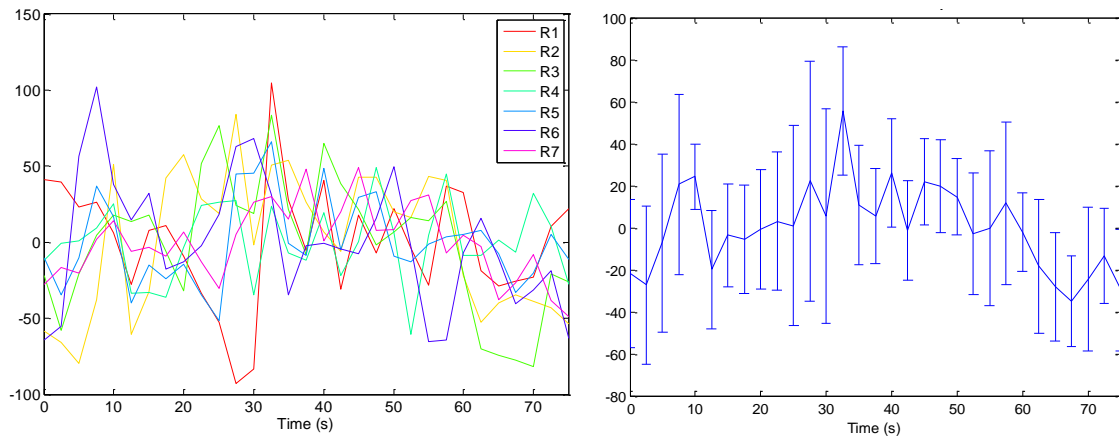


Figure 3.69: Time course of all subjects (left) and mean time course of all subjects (right) averaged over the BH without preparatory inspiration challenge blocks for CBF signal.

The time courses show a less complex shape compared to the time courses of the BH. Again, from the time courses we can see that there is an increase in BOLD signal as a consequence of an increase in CBF (increase vasodilation because of the increase in $P_{ET}CO_2$). In the BOLD and BOLD_{ASL} time courses, a well-defined main peak is observed in all subjects. This peak occurs earlier compared to the BH protocol with inspiration. However, from the CBF time courses we can only see a slight increase, probably due to the low SNR of this type of signal

4

Discussion and Conclusions

A sine/cosine model was proposed to estimate on a voxel-by-voxel basis the amplitude and delay of both CBF and BOLD responses to a BH paradigm. This was compared with a sine model with global delay optimization. The proposed sine/cosine model was successful in improving the sensitivity of both BOLD and BOLD_{ASL} responses to the BH paradigm. No significant improvements were found for CBF data. However CBF CVD maps were obtained for the first time and showed large variations across the brain. These results are partly due to the much lower SNR of CBF data. Furthermore, BH with preparatory inspiration time courses show a more complex shape and BOLD_{ASL} CVR maps in both BH protocols show that grey matter tends to have higher reactivity relative to the white matter.

Model Comparison

The use of the sine-cosine linear combination model, providing both CVR and CVD estimates on a voxel-by-voxel basis, presents clear advantages relative to the use of sine model with varying delays. Firstly, in this approach (SCC) only one GLM is fit to the data whereas in the SDO approach several GLM's are fit to the data, each with a different delay. The latter approach can be time consuming.

The SCC approach improved the sensitivity of both BOLD and BOLD_{ASL} responses to the BH paradigm. By obtaining a CVD map it is possible to observe patterns between different data and brain area (CBF CVDs vary much more across the brain). Significant differences were found for the CVD values of BOLD and BOLD_{ASL} responses between the two approaches, with the SCC approach having, on average, lower values of delay. No significant differences were found for the CBF data. CVR values obtained using the SCC approach were found to be, on average, higher for BOLD and BOLD_{ASL} data, relative to the SDO approach. No significant differences were found for the CBF data.

Protocol Comparison

Comparing the two BH protocols, the corresponding time-courses show different patterns. BH with preparatory inspiration time courses show a much more complex shape relative to the BH without preparatory inspiration time courses. It has been reported that the MR signal induced by BH with an initial preparatory inspiration has an initial biphasic shape that depends on the combination of several factors that are related to the respiratory act of inspiration such as reduction of pulmonary vascular tension, variation of heart rate and automatic modulation of cerebral myogenic autoregulatory responses [24][25]. Furthermore, studies using a breath hold challenge performed after expiration do not show this initial variation supporting the hypothesis that this initial changes are in fact due to the respiratory act itself.

Because of the time courses shape differences, it would be expected that the data from the BH protocol without preparatory inspiration would be best modelled by a sinusoid since it only has a main peak, contrarily to the BH protocol with preparatory inspiration that has a more complex shape. However, no significant differences were found between the two BH protocols in terms of the number of responsive voxels and CVR values, indicating that the sinusoidal modelling of the BH response is appropriate for protocols with or without preparatory inspiration. The CVD values were higher in the BOLD and BOLD_{ASL} data from the BH protocol with preparatory inspiration. No significant differences were found for CBF data. Again, this is probably due to the lower SNR of CBF data.

Future Work

Even though the noninvasive nature of BH fMRI measurements makes them appealing for the use in the clinical set, further work is still required. Particularly, in order to optimize the data and methodology for the analysis of CBF BH data, to elucidate the impact of different BH protocols on the results and to clarify the different delay distributions observed for BOLD and CBF.

Firstly, it is crucial to extend the study to a larger group of subjects. Also, the acquisition of $P_{ET}CO_2$ values for CVR computation can improve the results. Furthermore, a more careful regulation of the depth and rate of the subjects breathing could reduce group and intra-subject variability. This could also help understand the differences between the results obtained from the different BH protocols.

Since the BH protocols instructions are given as visual cues, there can be some unwanted activation in visual areas (occipital). One way to assess this is by performing a control experiment with auditory cues.

The criterion used to compute the CVD values in the SDO approach (the delay that yielded the maximum number of responsive voxels) may not be the best one. Perhaps the z-max information may be relevant and should be included as a criterion.

Our GLM analysis approaches can be optimized from a statistical point of view. In the SDO approach 75 GLM analyses were fitted in order to determine an optimal value of delay and the corresponding CVR map. Generally, when calculating probabilities from a statistical test which is repeated multiple times, the probability with which a researcher wrongly concludes that there is at least one statistically significant effect across a set of tests, even when in fact there is nothing going on, increases with each additional test. A related multiple comparisons concern is that, in a setting where nonzero true effects do exist, a researcher applying multiple tests may identify additional statistically significant effects that are not in fact real [70]. One of the most basic and most popular fixes to this problem is the Bonferroni correction, which adjusts the p -value at which a test is evaluated for significance based on the total number of tests being performed. Implicitly, it assumes that these test statistics are independent [70]. In our case, in order to try to correct this issue, principal component analysis (PCA) could be performed to determine how many of the 75 analysis are actually independent. Then, the p -value used in the post-statistical analysis should be divided by the number of independent models found.

In conclusion, the work presented in this Thesis has investigated different methodologies for the noninvasive assessment of cerebrovascular reactivity using MRI, both in terms of the respiratory challenge used as well as in terms of the modelling technique employed to analyse the data. Most importantly, the direct measurement of CBF using as ASL sequence was explored, critically contributing to the scarce literature on the subject. Further work is required in order to optimize the SCC methodology and to clarify the different CVD and CVR distributions observed for BOLD and CBF. Furthermore, the physiologic mechanisms behind the differences between BH protocols can be of great interest in future works and should be further investigated.

Bibliography

- [1] R. B. Buxton, *Introduction to Functional Magnetic Resonance Imaging: principles and techniques*, 2nd ed. Cambridge, 2002.
- [2] P. Tofts, *Quantitative MRI of the Brain: Measuring changes caused by disease*. John Wiley & Sons, 2003.
- [3] H. Ito, I. Kanno, C. Kato, T. Sasaki, K. Ishii, Y. Ouchi, A. Iida, H. Okazawa, K. Hayashida, N. Tsuyuguchi, Y. Kuwabara, and M. Senda, "Database of normal human cerebral blood flow, cerebral blood volume, cerebral oxygen extraction fraction and cerebral metabolic rate of oxygen measured by positron emission tomography with ¹⁵O-labelled carbon dioxide or water, carbon monoxide a," *European Journal of Nuclear Medicine and Molecular Imaging*, vol. 31, no. 5, pp. 635–643, 2004.
- [4] E. Rostrup, G. Knudsen, I. Law, S. Holm, H. Larsson, and O. Paulson, "The relationship between cerebral blood flow and volume in humans," *NeuroImage*, vol. 24, no. 1, pp. 1–11, 2005.
- [5] P. Vilela, "Imaging cerebrovascular reserve: how and why," in *ESMRMB 2012 - Teaching Syllabus*, 2012.
- [6] O. Paulson, S. Strandgaard, and L. Edvinsson, "Cerebral Autoregulation," *Cerebrovascular Brain Metabolism Review*, vol. 2, pp. 161–192, 1990.
- [7] D. Mandell, J. Han, J. Poulanc, A. P. Crawley, J. A. Stainsby, J. A. Fisher, and D. J. Mikulis, "Mapping cerebrovascular reactivity using blood oxygen level-dependent MRI in Patients with arterial steno-occlusive disease: comparison with arterial spin labeling MRI.," *Stroke*, vol. 39, no. 7, pp. 2021–8, Jul. 2008.
- [8] C. Heyn, J. Poulanc, A. Crawley, D. Mandell, J. S. Han, M. Tymianski, K. TerBrugge, J. A. Fisher, and D. J. Mikulis, "Quantification of cerebrovascular reactivity by blood oxygen level-dependent MR imaging and correlation with conventional angiography in patients with Moyamoya disease.," *American Journal of Neuroradiology*, vol. 31, no. 5, pp. 862–7, May 2010.
- [9] A. Kastrup, J. Dichgans, M. Niemeier, and M. Schabet, "Changes of Cerebrovascular CO₂ Reactivity During Normal Aging," *Stroke*, vol. 29, no. 7, pp. 1311–1314, Jul. 1998.
- [10] M. E. Thomason, B. E. Burrows, J. D. E. Gabrieli, and G. H. Glover, "Breath holding reveals differences in fMRI BOLD signal in children and adults.," *NeuroImage*, vol. 25, no. 3, pp. 824–37, Apr. 2005.
- [11] H. Okazawa, H. Yamauchi, K. Sugimoto, and M. Takahashi, "Differences in vasodilatory capacity and changes in cerebral blood flow induced by acetazolamide in patients with cerebrovascular disease.," *Journal of nuclear medicine : official publication, Society of Nuclear Medicine*, vol. 44, no. 9, pp. 1371–8, Sep. 2003.
- [12] A. Kastrup, G. Krüger, T. Neumann-Haefelin, and M. E. Moseley, "Assessment of cerebrovascular reactivity with functional magnetic resonance imaging: comparison of CO₂ and breath holding.," *Journal of magnetic Resonance Imaging*, vol. 19, no. 1, pp. 13–20, Jan. 2001.
- [13] A. Kastrup, T. Q. Li, G. H. Glover, and M. E. Moseley, "Cerebral blood flow-related signal changes during breath-holding.," *AJNR. American journal of neuroradiology*, vol. 20, no. 7, pp. 1233–8, Aug. 1999.

- [14] T. Q. Li, M. E. Moseley, and G. H. Glover, "A FAIR study of motor cortex activation under normo- and hypercapnia induced by breath challenge.," *NeuroImage*, vol. 10, no. 5, pp. 562–9, Nov. 1999.
- [15] R. F. Leoni, K. C. Mazzetto-Betti, A. C. Silva, A. C. Dos Santos, D. B. de Araujo, J. P. Leite, and O. M. Pontes-Neto, "Assessing Cerebrovascular Reactivity in Carotid Steno-Occlusive Disease Using MRI BOLD and ASL Techniques.," *Radiology Research and Practice*, vol. 2012, p. 268483, Jan. 2012.
- [16] L. Henriksen, "Brain luxury perfusion during cardiopulmonary bypass in humans. A study of the cerebral blood flow response to changes in CO₂, O₂, and blood pressure.," *Journal of cerebral blood flow and metabolism*, vol. 6, no. 3, pp. 366–78, Jun. 1986.
- [17] E. Bor-Seng-Shu, W. S. Kita, E. G. Figueiredo, W. S. Paiva, E. T. Fonoff, M. J. Teixeira, and R. B. Panerai, "Cerebral hemodynamics: concepts of clinical importance.," *Arquivos de neuro-psiquiatria*, vol. 70, no. 5, pp. 352–6, May 2012.
- [18] A. Vesely, H. Sasano, G. Volgyesi, R. Somogyi, J. Tesler, L. Fedorko, J. Grynspan, A. Crawley, J. Fisher, and D. Mikulis, "MRI mapping of cerebrovascular reactivity using square wave changes in end-tidal PCO₂.," *Magnetic resonance in medicine : official journal of the Society of Magnetic Resonance in Medicine / Society of Magnetic Resonance in Medicine*, vol. 45, no. 6, pp. 1011–3, Jun. 2001.
- [19] F. van der Zande, P. Hofman, and W. Backes, "Mapping hypercapnia-induced cerebrovascular reactivity using BOLD MRI.," *Neuroradiology*, vol. 47, no. 2, pp. 114–20, Feb. 2005.
- [20] U. Yezhuvath, K. Lewis-Amezcu, R. Varghese, G. Xiao, and H. Lu, "On the assessment of cerebrovascular reactivity using hypercapnia BOLD MRI.," *NMR in biomedicine*, vol. 22, no. 7, pp. 779–86, Aug. 2009.
- [21] E. Rostrup, I. Law, M. Blinkenberg, H. B. Larsson, A. P. Born, S. Holm, and O. Paulson, "Regional differences in the CBF and BOLD responses to hypercapnia: a combined PET and fMRI study.," *NeuroImage*, vol. 11, no. 2, pp. 87–97, Mar. 2000.
- [22] C. Ratnatunga and M. Adiseshiah, "Increase in middle cerebral artery velocity on breath holding: A simplified test of cerebral perfusion reserve," *European Journal of Vascular Surgery*, vol. 4, no. 5, pp. 519–523, 1990.
- [23] D. R. Corfield, K. Murphy, O. Josephs, L. Adams, and R. Turner, "Does hypercapnia-induced cerebral vasodilation modulate the hemodynamic response to neural activation?," *NeuroImage*, vol. 13, no. 6 Pt 1, pp. 1207–11, Jun. 2001.
- [24] S. Magon, G. Basso, P. Farace, G. K. Ricciardi, A. Beltramello, and A. Sbarbati, "Reproducibility of BOLD signal change induced by breath holding.," *NeuroImage*, vol. 45, no. 3, pp. 702–12, Apr. 2009.
- [25] R. M. Birn, J. B. Diamond, M. A. Smith, and P. A. Bandettini, "Separating respiratory-variation-related fluctuations from neuronal-activity-related fluctuations in fMRI.," *NeuroImage*, vol. 31, no. 4, pp. 1536–48, Jul. 2006.
- [26] M. E. Thomason and G. H. Glover, "Controlled inspiration depth reduces variance in breath-holding-induced BOLD signal.," *NeuroImage*, vol. 39, no. 1, pp. 206–14, Jan. 2008.
- [27] D. Handwerker, A. Gazzaley, B. A. Inglis, and M. D'Esposito, "Reducing vascular variability of fMRI data across aging populations using a breath holding task.," *Human brain mapping*, vol. 28, no. 9, pp. 846–59, Sep. 2007.

- [28] Y. Shen and I. Pu, "Quantification of venous vessel size in human brain in response to hypercapnia and hyperoxia using magnetic resonance imaging.," *Magnetic resonance in medicine : official journal of the Society of Magnetic Resonance in Medicine / Society of Magnetic Resonance in Medicine*, vol. 000, Apr. 2012.
- [29] M. G. Bright, D. P. Bulte, P. Jezzard, and J. H. Duyn, "Characterization of regional heterogeneity in cerebrovascular reactivity dynamics using novel hypocapnia task and BOLD fMRI.," *NeuroImage*, vol. 48, no. 1, pp. 166–75, Oct. 2009.
- [30] D. Lythgoe, S. Williams, M. Cullinane, and H. Markus, "Mapping of Cerebrovascular Reactivity using BOLD Magnetic Resonance Imaging," *Journal of magnetic Resonance Imaging*, vol. 17, no. 4, pp. 495–502, 1999.
- [31] M. Topcuoglu, "Transcranial Doppler ultrasound in neurovascular diseases: diagnostic and therapeutic aspects.," *Journal of Neurochemistry*, vol. 123 Suppl, pp. 39–51, Nov. 2012.
- [32] R. Pindzola, J. Balzer, E. Nemoto, and S. Goldstein, "Cerebrovascular Reserve in Patients With Carotid Occlusive Disease Assessed by Stable Xenon-Enhanced CT Cerebral," 2001.
- [33] N. Sadato, V. Ibañez, G. Campbell, M. Deiber, D. Le Bihan, and M. Hallett, "Frequency-dependent changes of regional cerebral blood flow during finger movements: functional MRI compared to PET.," *Journal of cerebral blood flow and metabolism : official journal of the International Society of Cerebral Blood Flow and Metabolism*, vol. 17, no. 6, pp. 670–9, Jun. 1997.
- [34] A. Shiino, Y. Morita, A. Tsuji, K. Maeda, R. Ito, A. Furukawa, M. Matsuda, and T. Inubushi, "Estimation of Cerebral Perfusion Reserve by Blood Oxygenation Level-Dependent Imaging[colon] Comparison With Single-Photon Emission Computed Tomography," *J Cereb Blood Flow Metab*, vol. 23, no. 1, pp. 121–135, Jan. 2003.
- [35] X. Golay, E. T. Petersen, I. Zimine, and T. C. C. Lim, "Arterial Spin Labeling: a one-stop-shop for measurement of brain perfusion in the clinical settings.," *Conference proceedings: Annual International Conference of the IEEE Engineering in Medicine and Biology Society. IEEE Engineering in Medicine and Biology Society. Conference*, vol. 2007, pp. 4320–3, Jan. 2007.
- [36] W. M. Luh, E. C. Wong, P. A. Bandettini, and J. S. Hyde, "QUIPSS II with thin-slice T1 periodic saturation: a method for improving accuracy of quantitative perfusion imaging using pulsed arterial spin labeling.," *Magnetic resonance in medicine : official journal of the Society of Magnetic Resonance in Medicine / Society of Magnetic Resonance in Medicine*, vol. 41, no. 6, pp. 1246–54, Jun. 1999.
- [37] T. Q. Li, A. Kastrup, A. M. Takahashi, and M. E. Moseley, "Functional MRI of human brain during breath holding by BOLD and FAIR techniques.," *NeuroImage*, vol. 9, no. 2, pp. 243–9, Feb. 1999.
- [38] S. A. Huettel, A. W. Song, and G. McCarthy, *Functional Magnetic Resonance Imaging*. Sinauer Associates, 2004.
- [39] C. Mulert and L. Lemieux, *EEG-fMRI: Physiological Basis, Technique and Applications.*, 1st ed. New York: Springer, 2010.
- [40] L. Pauling and C. Coryell, "The magnetic properties and structure of hemoglobin, oxyhemoglobin and carbonmonoxyhemoglobin," pp. 210–216, 1936.
- [41] S. Ogawa, T. M. Lee, A. R. Kay, and D. W. Tank, "Brain magnetic resonance imaging with contrast dependent on blood oxygenation.," *Proceedings of the National Academy of Sciences of the United States of America*, vol. 87, no. 24, pp. 9868–72, Dec. 1990.

- [42] B. Poser, M. Versluis, J. Hoogduin, and D. Norris, "BOLD contrast sensitivity enhancement and artifact reduction with multiecho EPI: parallel-acquired inhomogeneity-desensitized fMRI.," *Magnetic resonance in medicine : official journal of the Society of Magnetic Resonance in Medicine / Society of Magnetic Resonance in Medicine*, vol. 55, no. 6, pp. 1227–35, Jun. 2006.
- [43] M. Pimentel, P. Vilela, I. Sousa, and P. Figueiredo, "Localization of the hand motor area by arterial spin labeling and blood oxygen level-dependent functional magnetic resonance imaging.," *Human brain mapping*, vol. 00, Nov. 2011.
- [44] H. Lu, M. Donahue, and P. C. M. van Zijl, "Detrimental effects of BOLD signal in arterial spin labeling fMRI at high field strength.," *Magnetic resonance in medicine : official journal of the Society of Magnetic Resonance in Medicine / Society of Magnetic Resonance in Medicine*, vol. 56, no. 3, pp. 546–52, Sep. 2006.
- [45] T. T. Liu and G. G. Brown, "Measurement of cerebral perfusion with arterial spin labeling: Part 1. Methods.," *Journal of the International Neuropsychological Society*, vol. 13, no. 3, pp. 517–25, May 2007.
- [46] P. Figueiredo, S. Clare, and P. Jezzard, "Quantitative perfusion measurements using pulsed arterial spin labeling: effects of large region-of-interest analysis.," *Journal of magnetic resonance imaging*, vol. 21, no. 6, pp. 676–82, Jun. 2005.
- [47] G. K. Aguirre, J. A. Detre, E. Zarahn, and D. C. Alsop, "Experimental design and the relative sensitivity of BOLD and perfusion fMRI.," *NeuroImage*, vol. 15, no. 3, pp. 488–500, Mar. 2002.
- [48] E. C. Wong, R. B. Buxton, and L. R. Frank, "Quantitative imaging of perfusion using a single subtraction (QUIPSS and QUIPSS II).," *Magnetic resonance in medicine : official journal of the Society of Magnetic Resonance in Medicine / Society of Magnetic Resonance in Medicine*, vol. 39, no. 5, pp. 702–8, May 1998.
- [49] S. M. Smith, "Overview of fMRI analysis," *British Journal of Radiology*, vol. 77, no. suppl_2, pp. S167–S175, Dec. 2004.
- [50] R. A. Poldrack, J. Mumford, and T. Nichols, *Handbook of functional MRI data analysis*. Cambridge: Cambridge University Press, 2011.
- [51] FMRI Analysis Group, "FMRI Software Library." [Online]. Available: <http://www.fmrib.ox.ac.uk/fsl/>.
- [52] J. Wang, G. K. Aguirre, D. Y. Kimberg, A. C. Roc, L. Li, and J. A. Detre, "Arterial spin labeling perfusion fMRI with very low task frequency.," *Magnetic resonance in medicine : official journal of the Society of Magnetic Resonance in Medicine / Society of Magnetic Resonance in Medicine*, vol. 49, no. 5, pp. 796–802, May 2003.
- [53] O. Leontiev and R. B. Buxton, "Reproducibility of BOLD, perfusion, and CMRO2 measurements with calibrated-BOLD fMRI.," *NeuroImage*, vol. 35, no. 1, pp. 175–184, 2007.
- [54] T. Tjandra, J. C. W. Brooks, P. Figueiredo, R. G. Wise, P. M. Matthews, and I. Tracey, "Quantitative assessment of the reproducibility of functional activation measured with BOLD and MR perfusion imaging: implications for clinical trial design.," *NeuroImage*, vol. 27, no. 2, pp. 393–401, Aug. 2005.
- [55] W. M. Luh, E. C. Wong, P. A. Bandettini, B. D. Ward, and J. S. Hyde, "Comparison of Simultaneously Measured Perfusion and BOLD Signal Increases During Brain Activation With T1-Based Tissue Identification," vol. 143, pp. 137–143, 2000.

- [56] W. van der Zwaag, S. Francis, K. Head, A. Peters, P. Gowland, P. Morris, and R. Bowtell, "fMRI at 1.5, 3 and 7 T: Characterising BOLD signal changes," *NeuroImage*, vol. 47, no. 4, pp. 1425–1434, 2009.
- [57] A. Kastrup, G. Krüger, G. H. Glover, T. Neumann-Haefelin, and M. E. Moseley, "Regional variability of cerebral blood oxygenation response to hypercapnia.," *NeuroImage*, vol. 10, no. 6, pp. 675–81, Dec. 1999.
- [58] C. Chang, M. E. Thomason, and G. H. Glover, "Mapping and correction of vascular hemodynamic latency in the BOLD signal.," *NeuroImage*, vol. 43, no. 1, pp. 90–102, Oct. 2008.
- [59] R. F. Leoni, K. C. Mazzetto-Betti, K. C. Andrade, and D. B. de Araujo, "Quantitative evaluation of hemodynamic response after hypercapnia among different brain territories by fMRI.," *NeuroImage*, vol. 41, no. 4, pp. 1192–8, Jul. 2008.
- [60] W. Chu, Y. Hsu, K. Lim, and H. Liu, "Quantitative Evaluation of the Dynamic BOLD and CBF Responses to Breath Hold in Different Brain Territories," *Proc. Intl. Soc. Mag. Reason. Med.*, vol. 19, p. 1644, 2011.
- [61] N. P. Blockley, I. D. Driver, S. T. Francis, J. A. Fisher, and P. A. Gowland, "An improved method for acquiring cerebrovascular reactivity maps.," *Magnetic resonance in medicine : official journal of the Society of Magnetic Resonance in Medicine / Society of Magnetic Resonance in Medicine*, vol. 65, no. 5, pp. 1278–86, May 2011.
- [62] M. E. Thomason, L. C. Foland, and G. H. Glover, "Calibration of BOLD fMRI using breath holding reduces group variance during a cognitive task.," *Human brain mapping*, vol. 28, no. 1, pp. 59–68, Jan. 2007.
- [63] J. Jorge, P. Vilela, W. van der Zwaag, and P. Figueiredo, "Improving the characterization of the BOLD response to breath-hold challenges," *Proceedings of the 18th Annual Meeting of the Organization of Human Brain Mapping*, 2012.
- [64] S. M. Smith, "Fast robust automated brain extraction," *Human Brain Mapping*, vol. 17, pp. 143–155, 2002.
- [65] M. Jenkinson, P. Bannister, M. Brady, and S. Smith, "Improved Optimization for the Robust and Accurate Linear Registration and Motion Correction of Brain Images," *NeuroImage*, vol. 17, no. 2, pp. 825–841, Oct. 2002.
- [66] J. Lancaster, D. Tordesillas-Gutiérrez, M. Martínez, F. Salinas, A. Evans, K. Zilles, J. Mazziotta, and P. Fox, "Bias between MNI and Talairach coordinates analyzed using the ICBM-152 brain template.," *Human brain mapping*, vol. 28, no. 11, pp. 1194–205, Nov. 2007.
- [67] Y. Zhang, M. Brady, and S. Smith, "Segmentation of brain MR images through a hidden Markov random field model and the expectation-maximization algorithm.," *IEEE transactions on medical imaging*, vol. 20, no. 1, pp. 45–57, Jan. 2001.
- [68] J. Mumford, L. Hernandez-Garcia, G. R. Lee, and T. E. Nichols, "Estimation efficiency and statistical power in arterial spin labeling fMRI.," *NeuroImage*, vol. 33, no. 1, pp. 103–14, Oct. 2006.
- [69] O. Friman, J. Cedefamn, P. Lundberg, M. Borga, and H. Knutsson, "Detection of neural activity in functional MRI using canonical correlation analysis.," *Magnetic resonance in medicine : official journal of the Society of Magnetic Resonance in Medicine / Society of Magnetic Resonance in Medicine*, vol. 45, no. 2, pp. 323–30, Feb. 2001.

- [70] A. Gelman, J. Hill, and M. Yajima, "Why we (usually) don't have to worry about multiple comparisons," pp. 1–25, 2008.